Summer 2022

PROCESSING AND CHARACTERIZATION OF TINI-BASED ALLOYS FABRICATED BY LASER AIDED MANUFACTURING

Yitao Chen
Missouri University of Science and Technology

Department: Mechanical and Aerospace Engineering

Recommended Citation
Chen, Yitao, "PROCESSING AND CHARACTERIZATION OF TINI-BASED ALLOYS FABRICATED BY LASER AIDED MANUFACTURING" (2022). *Doctoral Dissertations*. 3218.
https://scholarsmine.mst.edu/doctoral_dissertations/3218

PROCESSING AND CHARACTERIZATION OF TINI-BASED ALLOYS FABRICATED BY LASER AIDED MANUFACTURING

by

YITAO CHEN

A DISSERTATION

Presented to the Graduate Faculty of the

MISSOURI UNIVERSITY OF SCIENCE AND TECHNOLOGY

In Partial Fulfillment of the Requirements for the Degree

DOCTOR OF PHILOSOPHY

in

MECHANICAL ENGINEERING

2022

Approved by:

Frank Liou, Advisor
K. Chandrashekhara
Lokeswarappa Dharani
Ashok Midha
F. Scott Miller

PUBLICATION DISSERTATION OPTION

This dissertation consists of the following four articles, formatted in the style used by the Missouri University of Science and Technology:

Paper I, found on pages 8–46, has been published in *Materials*.

Paper II, found on pages 47–76, has been published in *Applied Sciences*.

Paper III, found on pages 77–103, has been published in *Materials*.

Paper IV, found on pages 104–128, is intended for submission to *The International Journal of Advanced Manufacturing Technology*.

ABSTRACT

Laser powder-based directed energy deposition (DED) is a major laser aided additive manufacturing (AM) process for metals. It applies laser energy to deposit metal powders to form 3D metal parts. Apart from manufacturing traditional alloys, DED can also be used to develop advanced alloys with the novel idea of elemental powder mixture feedstock. TiNi-based alloy is a type of shape memory alloy (SMA), a smart material with unique shape memory effects. Using laser powder DED to synthesize TiNi-based SMAs from elemental powder mixture can create more possibilities in new compositions and properties. It can also overcome the limitations of conventional manufacturing.

In this work, a comprehensive review on applying elemental powder mixture in the DED process to fabricate all kinds of alloys was first performed to summarize the current status of this novel method. Then, the elemental powder DED process was used to deposit Ti–Ni–Cu ternary SMA with Cu as the third element to extend the application of DED in fabricating ternary SMAs. The major phase obtained was TiNi phase with successful shape memory effects. Next, Ti-rich Ti–Ni–Cu ternary SMA was fabricated on the substrate of near equiatomic TiNi binary SMA by the elemental powder DED process to build bi-metallic SMA structures with two different SMA sections and multiple shape memory effects. The joining region obtained a good quality, and the multiple shape memory temperatures were demonstrated. Heat treatment effects on material properties of the as-deposited bi-metallic Ti–Ni–Cu/TiNi SMA were also studied, and the various combinations of properties show that the DED process via elemental powder has great potential in developing multifunctional smart alloys with a wide range of applications.

ACKNOWLEDGMENTS

First and foremost, I express my sincere gratitude to my advisor Dr. Frank Liou for offering me this great opportunity to work in this excellent lab, and for all his guidance, support, and encouragement. It has been a great honor to have worked with him. I extend my appreciation to my committee members Dr. Ashok Midha, Dr. K. Chandrashekhara, Dr. F. Scott Miller, and Dr. Lokeswarappa Dharani for their valuable feedback and suggestions on my work. My sincere thanks also go to Dr. Joseph Newkirk for sharing his professional advice to improve the research quality.

Thank you to all the experts who provided instruction and training on lab equipment, especially Dr. Eric Bohannan, Dr. Clarissa Wisner, Dr. Jincheng Bai, Dr. Wei-Ting Chen, Dr. Jeremy Watts, Dr. Nathan Leigh, Dave Satterfield, and Fred Eickelmann. Other than research, it was also a nice experience to work with Dr. Jillian Schmidt and Dr. Michael Puopolo as a teaching assistant. Also, many thanks to office staff members especially Karen Walberg, Shelly Morgan, and Jade Sinnott for their guidance and help in the academic program.

Thanks to my labmates and other graduate students for their discussion, collaboration, and help: Xinchang, Lei, Wei, Jingwei, Yunlu, Sreekar, Xueyang, Masud, Todd, Praneeth, Aaron, Rachel, Wenyuan, Lan, Tan, Connor, Max, Bharadwaja, Braden, Jonathan, Usman, Freddy, Will, Cesar, Daches, Anilas, Hans, Austin, etc. Also, I appreciate all other friends who shared unforgettable moments with me during my Ph.D. journey.

Last but not the least, I wish to extend my special and sincere thanks to my parents. None of these would happen without their love, encouragement, and unwavering support.

TABLE OF CONTENTS

Page

SECTION

LIST OF ILLUSTRATIONS

Page

PAPER I

PAPER II

PAPER III

PAPER IV

LIST OF TABLES

1. INTRODUCTION

1.1. BACKGROUND

TiNi-based alloy with a near equal atomic composition of Ti and Ni elements is attracting interest in various industries, including but not limited to civil engineering, aerospace engineering, actuators, and biomedical field, owing to its unique shape memory effect, superelastic behavior, and excellent biocompatibility [1–3]. As for the shape memory effect, TiNi-based alloy belongs to shape memory alloy (SMA), a class of smart material that can memorize shapes with temperature changes [3]. The knowledge and experience in the manufacturing and processing of TiNi-based alloys are of great importance. It was reported that traditional machining processing methods are difficult for TiNi-based alloys [4,5]. Therefore, more approaches are in need for processing TiNi-based alloys in a faster and more cost-effective way.

In addition to traditional manufacturing processes, additive manufacturing (AM) has large potential in the manufacturing of complex products with a layer-by-layer fashion, and laser is an effective energy source in the field of AM [6]. Laser directed energy deposition (DED) is a laser aided AM technique for metals, which uses laser energy to deposit raw metallic materials, either powders or wires, to build 3D parts [7]. As the DED process uses the additive approach, the geometric flexibility is much higher in fabricating complex bulk metal parts and performing part repairing that conventional manufacturing can hardly handle [8,9]. Also, the AM process causes less waste [10]. Nowadays, various types of industrial alloys have been made into pre-alloyed powders and used in DED, including steels [9], Al-alloy [11], Ti-6Al-4V [12], and Inconel625 [13], etc. Due to the limitations in conventional material subtraction approaches, using the AM process such as DED with the additive feature can be a different feasible way to fabricate and develop novel TiNi-based alloys [14]. AM process is commonly known as 3D printing [9]. While when the AM process is used in the manufacturing of TiNi-based alloys with shape memory effects that the shape changes with time, it is also regarded as 4D printing [14].

The DED processing technique also has high material flexibility [15]. For powder state feedstocks, multiple different powders can be pre-mixed in a wide range of compositions and fed simultaneously during the DED process. Then, apart from using pre-alloyed powders, researchers also have started to try fabricating alloys by DED using elemental powder mixture as an alternative type of powder feedstock [16,17]. In the early days, elemental powder mixture was applied in powder metallurgy as a cost-effective approach [18]. Then it was also adopted in the powder-based AM processes, including DED [17]. The novel method of using elemental powder in DED has several main advantages. For pre-alloyed powders, each powder particle is designed with a fixed composition. In comparison, the elemental powder mixture has the potential to lead to more possibilities in novel alloy manufacturing [17], resulting in wider varieties of properties and performances, which can potentially contribute to the novel alloy development. With elemental powder mixtures, generating more possibilities in novel alloy manufacturing could be more cost-effective [17]. Also, in the DED manufacturing system, the alloy composition can be changed during the manufacturing process by controlling the feeding rate or mixing composition at different layers. Then, various compositions within a single part can be realized, which shows more functions than homogeneous alloys [19].

Multifunctional metal parts can be useful in many industrial environments that need material components to possess different properties at different spatial locations [19].

In the manufacturing of TiNi-based alloy, using Ti and Ni elemental powder is more cost-effective than TiNi alloy powders [20]. Thus, using elemental powder mixture as the feedstock in DED to fabricate smart alloys like TiNi-based SMA also has a large potential [20]. Also, it was found that a third metal element can be added to the TiNi alloy system to form ternary SMAs that can adjust material properties such as phase transformation temperatures [21,22]. The effect of adding a type of third element in the TiNi system can be more conveniently studied using the flexible elemental powder mixture technique in DED. However, the work in using DED to fabricate TiNi-based ternary SMA by elemental powders is still limited, and more understanding and knowledge are needed in TiNi-based ternary SMAs by AM using elemental powders, and the correlations among element composition, structure, and functional properties.

Moreover, by taking advantage of the layer-wise additive feature and the wide range of material selection in both the substrate materials and powder feedstock materials, DED can also be used to deposit structures with multiple sections of different alloys or join different metal sections to realize bi-metallic structures and graded structures, which fully utilizes the high degree of customization in both spatial locations and material compositions. Examples of bi-metallic structures by DED include Cu/steel [23,24], Cu/Inconel [25], Ti-6Al-4V/Al12Si [26], etc., which can combine excellent properties from both metals. DED can be applied to directly deposit one type of alloy on the other type of alloy used as substrate material [27] or insert graded layers or intermediate layers to improve the joining [28]. Also, more possible joining structures can be designed and invented with the aid of elemental powder mixtures. Other than joining bi-metallic structures from traditional alloys, for smart alloys such as SMAs, TiNi-based alloys with different compositions, structures, and functional properties can also be combined into bi-metallic SMA that can demonstrate multiple memory effects. An example of functionally graded TiNi-based alloy was reported, which was fabricated using the powder-bed AM process selective laser melting with adjustable processing parameters at different TiNi sections [29]. While very limited work has been done in taking advantage of the promising elemental powder DED AM process to develop bi-metallic smart metals such as TiNi-based multi-sectional SMAs and study the shape memory behavior of different sections. The feasibility of manufacturing bi-metallic SMAs using the elemental powder DED process, the study and evaluation of performance, including but not limited to joining quality, bonding strength, the exhibition of multiple shape memory behaviors, and the post-processing effect on the entire bi-metallic multifunctional structure will all be of great interest in the manufacturing of new smart materials.

1.2. RESEARCH OBJECTIVES

The objective of this research is to improve the understanding and advance the knowledge of the fabrication and development of advanced alloys by laser aided DED manufacturing process with elemental powders as feedstocks. Also, it aims to provide more perspectives on incorporating AM process, especially DED, in developing more novel smart alloys such as TiNi-based ternary SMAs and bi-metallic SMAs with multiple functional behaviors to benefit a wide range of industries.

Although several groups have attempted to use DED to 3D print various alloys with elemental powder [17,30,31], a systematic review in the research progress of using elemental powder blends in the DED process to fabricate various alloys has not been done. Therefore, a comprehensive review of the use of the elemental powder DED process in manufacturing all types of metal alloys will be first performed. The review will cover the latest progress and outlook to contribute to both the metal AM area and the development of new alloys for AM.

The second topic will be conducted to study the fabrication of Ti–Ni–Cu ternary SMAs by elemental powder DED to make good use of DED in fabricating novel SMAs. Various types of third elements can be added to the Ti–Ni binary system, which is expected to adjust material properties and shape memory behaviors on the TiNi-based SMA, while the addition of the Cu element is expected to narrow down the thermal hysteresis of the phase transformation [21,32]. The feasibility of using the elemental powder mixture in the DED AM process to fabricate Ti–Ni–Cu ternary SMA will be conducted by depositing elemental Ti, Ni, and Cu powder mixtures on pure Ti substrate. The as-mixed Ti, Ni, and Cu composition of Ti–45at.%Ni–5at.%Cu will be used, where a few amounts of Cu will be added. Microstructure analysis, phase information, mechanical properties, and shape memory effects study will all be carried out to evaluate the fabrication outcome. Also, the correlations among composition, structure, and properties of the as-fabricated alloys will be presented.

In the third topic, the fabrication of Ti–Ni–Cu ternary SMA will be expanded to the design and development of SMAs with multifunctions such as multiple shape memory effects. Studies of using the DED AM process to build TiNi-based bi-metallic alloy structures will be carried out. To achieve the goal of the TiNi-based bi-metallic SMAs with multiple shape memory effects, two different types of compositions were selected for the substrate material and the powder material for the DED process. A Ti-rich Ti/Ni/Cu elemental powder mixture with a Ti composition of 53 at.% will be used for feedstock, while a near equiatomic TiNi binary alloy will be picked for the substrate. The transformation temperatures at both sections and the bonding strength at the interface will be evaluated. Also, the multiple mechanical behaviors will be revealed by the digital image correlation technique, which can be a useful tool to accurately record the mechanical behaviors of the multi-sectional bi-metallic SMA.

Based on the third topic, the investigation of heat treatment on properties of TiNi-based bimetallic structure built by DED will be conducted. Since both laser heat effect and post heat treatment can affect the microstructure and material properties [33,34], this work will provide more investigations on the effect on the multi-sectional structure features and shape memory effects from both laser effects during the DED process and the post heat treatment effects at different locations of the bi-metallic structure, which will finally greatly contribute to a wider range of property combinations in bi-metallic multifunctional new SMAs.

1.3. ORGANIZATION OF DISSERTATION

In this dissertation, four major works are presented by four papers. In Paper I, a systematic review of fabricating metallic alloys using the laser aided DED AM process with the novel idea of elemental powder mixture feedstock is carried out. The review summarizes the advantages of using elemental powder as raw materials in the DED process and covers the latest progress in the design, development, and modifications of all kinds of metallic alloys, including conventional alloys and novel alloys. Also, points that are not widely explored and some potential challenges are discussed. Paper II presents the fabrication and comprehensive characterization of Ti–Ni–Cu ternary SMA on pure titanium substrate material by the DED process with elemental powders. It shows both good shape memory behaviors and effects from the addition of the third element, which provides useful results in the manufacturing of TiNi-based SMA with more element types using the cost-effective elemental powders in the AM area. Paper III presents the development of bi-metallic SMA structures by depositing Ti-rich Ti–Ni–Cu ternary SMA using elemental powder DED on near equiatomic TiNi binary SMA substrate in order to create a combining effect of two different SMAs to achieve multiple shape memory responses. It successfully demonstrates a good metallurgical bonding between two SMA sections and the multiple shape memory effect. This paper also provides perspectives on incorporating the flexible elemental powder DED AM process with the development of novel SMAs with both a wider range of elements and a structure with more functions. Post heat treatment studies on the DED bi-metallic SMA can be seen in Paper IV. It investigates the heat effect on the structure and properties at multiple locations of the bi-metallic SMA structure from both laser and post heat treatment. This paper proposes potential methods to further adjust the combined functional properties and expand the application possibilities of DED TiNi-based bi-metallic SMAs.

PAPER

I. A REVIEW ON METALLIC ALLOYS FABRICATION USING ELEMENTAL POWDER BLENDS BY LASER POWDER DIRECTED ENERGY DEPOSITION PROCESS

ABSTRACT

The laser powder directed energy deposition process is a metal additive manufacturing technique, which can fabricate metal parts with high geometric and material flexibility. The unique feature of in-situ powder feeding makes it possible to customize the elemental composition using elemental powder mixture during the fabrication process. Thus, it can be potentially applied to synthesize industrial alloys with low cost, modify alloys with different powder mixtures, and design novel alloys with location-dependent properties using elemental powder blends as feedstocks. This paper provides an overview of using a laser powder directed energy deposition method to fabricate various types of alloys by feeding elemental powder blends. At first, the advantage of laser powder directed energy deposition in manufacturing metal alloys is described in detail. Then, the state-of-the-art research and development in alloys fabricated by laser powder directed energy deposition through a mix of elemental powders in multiple categories is reviewed. Finally, critical technical challenges, mainly in composition control are discussed for future development.

1. INTRODUCTION

Additive manufacturing (AM) is a novel manufacturing technique that can fabricate a wide range of materials and complex structures. The definition given in the American Society for Testing and Materials (ASTM) states that: AM is “The process of joining materials to make objects from 3D model data, usually layer upon layer, as opposed to subtractive manufacturing methodologies [1]”. Due to its layer-based additive nature that is different from subtractive manufacturing, AM created a paradigm shift in the manufacturing industry [2]. AM has lots of advantages compared to traditional subtractive manufacturing. For example, AM can directly produce complex 3D parts without much tooling and assembly. It is also much more material-saving than conventional manufacturing since conventional manufacturing mainly uses the subtractive method to remove materials to reach the desired geometry [3]. Thus, AM has become more essential in the manufacturing industry. As metals and their alloys are of great importance in human life, efforts have been paid on the research and development of AM of metals and alloys [4]. Based on the mechanism and material, the AM process has been classified into seven categories [5]. There are four major categories associated with metal additive manufacturing, which are powder bed fusion (PBF), directed energy deposition (DED), binder jetting (BJ), and laminated object manufacturing (LOM). Among them, PBF and DED are more commercialized [5]. According to ASTM F3187-16 standard guide for DED technique [6], the DED process applies an energy source to fuse feedstock metallic materials by melting during deposition. Metallic materials in powder or wire form are fed into the melt pool and solidify into a 2D solid layer. The tool path is guided by path planning to fill every layer, and the successive layers will be built until a 3D part is achieved [6]. The laser powder DED process applies laser as the energy source and metal powder as the raw material feedstock. In this paper, we focus on the laser powder DED, and for convenience, here we use DED to represent the laser powder DED process. Using computer-aided design (CAD) tools, a 3D model of a part can be created, and the slicing algorithm can be used to slice the 3D model into many 2D layers. Figure 1 shows the schematic diagram of the DED process using powder as feedstock. During the DED process, a laser beam is applied to create a melt pool, and metal powders are carried and blown into the melt pool by the inert gas. After the laser moves away, melted powders will join and cool down to form a solid layer. The laser travels according to the toolpath for each layer. By repeating this procedure for each layer, a 3D part can be constructed [7].

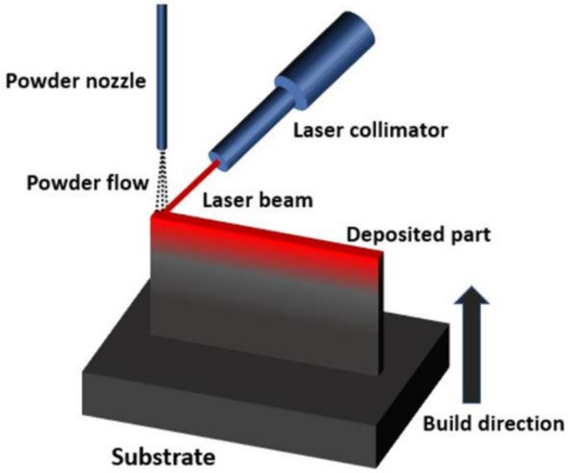

Figure 1. Schematic illustration of DED to build a 3D part.

During the past decade, typical metal alloys fabricated by DED has been studied. These alloys include austenitic stainless steels (304/304L [8,9] and 316/316L [10,11]), precipitation hardening stainless steels (17-4 PH [12]), nickel-based superalloys (Inconel 718 [13,14] and Inconel 625 [15,16]), titanium alloys (Ti-6Al-4V [17,18,19,20]), etc. DED and PBF have their own advantages according to their special features. For DED, it is able to build parts on a non-flat surface while PBF usually needs a horizontal area for powder spreading. Thus, modification of the curved surface and repairing of damaged parts are also possible using the DED process [21,22,23]. The part remanufacturing can be collaborated with reverse engineering to repair damaged parts by constructing a damaged profile and determine the laser scanning strategy, which will be of great significance in saving cost on tooling [24,25]. As an in-situ powder feeding process, it has the potential to fabricate parts without an enclosed chamber [26]. Therefore, the volume of building parts can be much larger than the PBF process. One more important feature is because of the in-situ powder feeding process, DED can flexibly create different material compositions from layer to layer by mixing different powders; however, this is difficult to be realized in PBF. Therefore, much more metallic alloys with various compositions can be potentially directly created by taking this advantage of DED. This novel aspect of DED will be the main topic to review in this article.

Metal powders are the commonly used raw materials and feedstocks in the DED process. Most of the powders used in DED mentioned in the former paragraphs are pre-alloyed powders, which indicate that each powder particle is designed with the prescribed composition. Since the composition is identical in each particle, the composition of the as-fabricated 3D part made by DED is usually close to constant. However, the cost of producing pre-alloyed powders are high. Therefore, similar to using cost-effective elemental powders in powder metallurgy [27,28,29], the idea of mixing elemental powders into the desired composition to synthesize alloys is also arisen in the area of AM, especially for DED. The cost of alloy powder manufacturing can be reduced by using elemental powders. Also, as each pre-alloyed powder particle has a constant elemental composition, the possibility of fabricating various types of alloys using DED is limited. If the pre-alloyed powders are replaced by elemental powder blends, it is possible to fabricate more alloys with a pre-designed elemental weight percentage or atomic percentage. This replacement can potentially make a great contribution to the development of novel alloys through the thorough investigation of different alloy systems. In addition, with the evolvement of highly automated DED manufacturing systems, the weight composition of multiple elemental powders can be changed during the manufacturing process by in-situ control of the feeding rate. Then, a variety of elemental compositions can coexist within a single part, which can be more functional than homogeneous alloys.

Although a few works have been done using DED to fabricate various alloys, as a relatively new method in DED, a comprehensive overview of the research progress of DED using elemental powder blends has not been done. Thus, an overview of the elemental powder-based DED process can provide new knowledge systems for the metal AM area and potentially develop new alloys, which can significantly widen the application of metal AM in the next generation of manufacturing fields. This review paper will summarize the current research progress in different types of applications via DED and discuss the major technical challenges and issues that remained in this area in order to provide guidelines for future studies.

2. CURRENT STATUS OF DED USING ELEMENTAL POWDER

The typically reported research works in DED using elemental powders can be generally classified into two categories, which are listed and elaborated in Section 2.1 and Section 2.2, respectively. Many types of industrial alloys can be potentially fabricated by mixing the specified composition of elemental powders. Also, conventional alloys can be flexibly modified by mixing elemental powders with other compositions to get an in-depth understanding of how a certain element affects the final properties. The study of the effect of specific elements on the as-fabricated parts will be more direct. With the flexible change in compositions, various types of alloys with a gradual shift in alloy compositions can be joined and form functionally graded materials (FGMs). Using DED and elemental powder blend method can investigate FGMs that are difficult to realize using conventional manufacturing. Novel alloys, especially high entropy alloys (HEAs), which need more types of elements, can be fabricated and designed flexibly by the DED process using elemental powders. Section 3 mainly covers the controlling of the deposition in multiple aspects. The outlook is discussed in Section 4, while the conclusion is summarized in Section 5.

2.1. INDUSTRIAL ALLOYS AND INTERMETALLICS

There is a wide variety of alloys that are prevalent in the industry due to their excellent mechanical properties. However, due to the high manufacturing cost, they are mostly seen in specific areas. For instance, Ti-6Al-4V is an excellent industrial alloy with high specific strength and corrosion resistance [30]. However, the cost is high for certain industrial areas such as automobile and transportation [31]. Thus, reducing the manufacturing cost of Ti-6Al-4V is essential to expand the applications. Near net shape processing, such as powder metallurgy, was reported as a cost-effective approach to develop and expand the use of titanium alloys [32]. In the area of powder metallurgy, the elemental powder blend is applied to form titanium alloys and avoid the high cost of pre-alloyed powders [32]. Based on the elemental powder method applied in powder metallurgy, blending elemental powder to fabricate alloys has also become a potential method in powder-based metal AM, such as DED, to reduce the manufacturing cost and open new perspective research and industrial fields. Until now, several attempts were made in synthesizing Ti-6Al-4V by a mixture of Ti, Al, and V pure powders via DED. Differences were found between Ti-6Al-4V fabricated by DED using elemental powder blends and conventional Ti-6Al-4V. Manufacturing issues were also identified. More investigation of properties and performances of DED-processed Ti-6Al-4V using elemental powder blends are needed.

Hua et al., Yan et al., and Chen et al. [33,34,35,36] mixed Ti, Al, and V elemental powders to fabricate Ti-6Al-4V, which proved the feasibility of making industrial alloys like Ti-6Al-4V using elemental powders in a cost-effective approach. Apart from Ti-6Al-4V, Clayton [37] applied pure Fe, Cr, and Ni powders to make Fe-based alloys similar to stainless steels such as SS316 and SS430. It was found that the Fe-based alloy Fe-17Cr-12Ni made by elemental powder mixture got similar microstructure and mechanical properties with SS316. On the other hand, properties of the alloy Fe-17Ni fabricated by elemental powder mixture was not comparable with the conventional pre-alloyed SS430. More experimental investigations are needed to reveal the attributes of the difference in properties. Similarly, a number of other Fe-, Ti-, and Ni-based alloys in Fe-Cr-Ni and Ti-Al-V alloy systems can be potentially fabricated by mixing elemental powders with certain compositions. It is significantly beneficial to the alloy manufacturing industry that using only a small stock of Fe, Cr, Ni, Ti, Al, and V powders can generate a large number of alloy combinations.

Some types of intermetallic compounds possess excellent mechanical properties that could be widely used in various industries. Thanks to the manufacturing flexibility of the DED process, many hard-to-machine intermetallic compounds can now be fabricated by new methods. As a wide variety of intermetallic compounds only consist of two metal elements, mixing elemental powder can be a convenient way to synthesize those compounds. A couple of intermetallics are attractive for their high wear and corrosion resistance. For instance, Fe-Al intermetallics possess excellent wear, corrosion, and oxidation resistance. It can also function in a high-temperature environment. Conventionally, Fe-Al intermetallics are manufactured by sintering blended elemental powders. However, this process causes high energy consumption and cost [38]. Therefore, the DED process was also introduced for the fabrication of Fe-Al intermetallic [38]. Pęska et al. [39] applied elemental Fe and Al powder to synthesize Fe-Al intermetallics by DED. The hardness of the as-fabricated samples was very similar to the classically built Fe-Al intermetallics.

NiTi is a special intermetallic compound with unique shape memory effects and superelasticity. It is also biocompatible and corrosion resistive [40]. Thus, it is widely used in structures with shape-changing effect and biomedical implants. Machining is difficult to process NiTi. To reduce the machining procedure, attentions are paid on near-net shaping processes, especially AM. Attempts were made by using the DED process to fabricate NiTi and pre-alloyed powders were applied in [41,42,43]. As pre-alloyed NiTi powder is expensive, blending Ni and Ti elemental powder is an alternative way to in-situ synthesize Ni-Ti alloys and with a variety of composition design. Halani et al. [44] applied the DED process to fabricate NiTi using elemental powder. Different compositions such as Ni55Ti45 and Ni50Ti50 in atomic percentage were attempted for the deposition process. Similarly, Shiva et al. [45] studied the difference among premixed compositions of Ni45Ti55, Ni50Ti50, and Ni55Ti45. Bimber et al. [46,47,48] conducted works in fabricating NiTi by DED with elemental powder blends. They built large volume structures to find out the difference in the secondary phase, compressive properties, and martensitic transformation temperature regarding the spatial locations. Other works include comparative studies among DED, SLM, and EBM by Wang et al. [49]. Figure 2 shows the microstructure of NiTi alloy fabricated by DED in [49]. Different issues were identified in three metal AM processing methods, which will be discussed in the later sections.

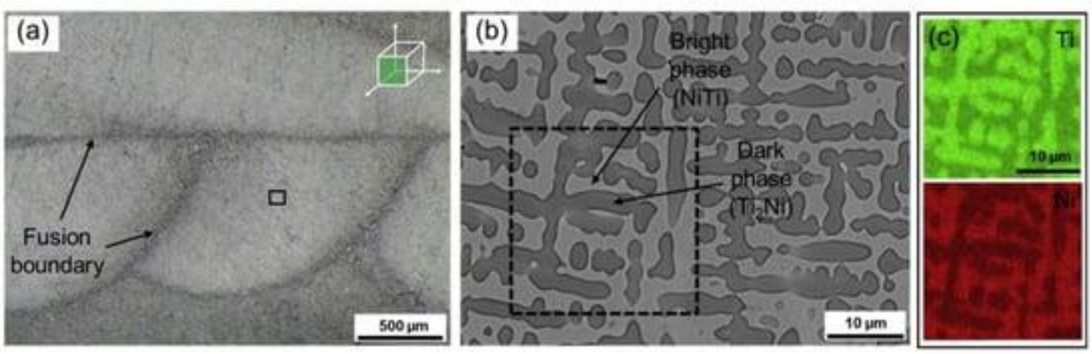

Figure 2. (a) Microstructure and fusion boundary of NiTi alloy fabricated by DED using elemental powder blends. (b) SEM image of the NiTi alloy with NiTi phase and Ti_2Ni phase. (c) EDS mapping of Ti and Ni [49]. (Reproduced with permission from Elsevier).

Other types of intermetallics for surface strengthening using elemental powder mixture for DED were also studied. Most of the works focus on the surface strengthening of steel and titanium alloy to improve wear and corrosion resistance by synthesizing intermetallics on the surface. Yu et al. [50] applied elemental Al and Ni powder to synthesize pure Ni_3Al intermetallic compound coating on 1Cr18Ni9Ti stainless steel. Effects of laser energy density on tribological behavior and crystallographic orientation were studied. Wang et al. [51,52,53,54] have fabricated various types of intermetallics for surface coating applications using laser cladding. Those works include coating $TiCo/Ti_2Co$ on titanium alloy [51], coating $Ti_5Si_3/NiTi_2$ on titanium alloy [52], and coating Cr_3Si on austenitic stainless steel 1Cr18Ni9Ti by using Cr-Si-Ni elemental powder as the precursor material [53]. Si was also blended with metal powders to provide intermetallics and $Ni_2Si/NiSi$ on 0.2% C carbon steel [54]. Zhong et al. [55] applied the DED process to clad WC/Ni hardfacing alloy on 40Cr steel by using W, C, and Ni elemental powder. The in-situ reaction produced WC hard phase in the Ni matrix for surface wear resistance improvement. Different dissolution behaviors were observed in W and C/Ni powder within the melt pool at different locations in the melt pool. The dissolution situation of W, C, and N depends highly on the local temperature distribution and reheating, which is related to laser deposition parameters and deposition strategies.

2.2. DEVELOP ADVANCED ALLOYS

Due to the advantage of customization and small-batch manufacturing, the DED process with blended elemental powders is also a powerful tool for developing novel alloys and inventing innovative materials [33]. Changes in structure and property of adding different types and quantities of elements in an alloy system can be quickly observed by a small volume deposition, rather than making a large structure using conventional methods. By adding more alloying elements, the fabrication of advanced alloys such as FGMs, HEAs, and metallic glass can also be realized. Therefore, using elemental powder will then create many more probabilities in the field of alloy design in a cost-effective way.

2.2.1. Alloy Modification. Modifying alloys can be flexible by using elemental powders in DED, as the composition can be customized by varying parts of the elements or all elements. This method may either solve the difficulty in processing certain alloys or study the element effects in alloy systems using DED. This advantage can benefit the development of numerous binary and ternary alloy systems, including, but not limited to Cu-Ni, Ti-Nb, Fe-W, Ti-Al-Mo, etc. [56,57,58,59] and the development of new alloys. Cu and Ni are completely soluble, which attracts industrial interests in making Cu-Ni alloys with both high thermal conductivity from Cu and high mechanical properties from Ni. Karnati et al. [56] mixed elemental Cu and near-pure Ni powders in different composition levels, and they all produced solid solutions of Cu-Ni alloys. Li et al. [57] deposited 80W-20Fe using elemental W and Fe powders, which indicates DED is an effective and novel method to process W based alloys. Fallah et al. [58] deposited 55 wt.% Ti/45 wt.% Nb in elemental powder blend on the Ti-6Al-4V substrate to create a compositionally modified surface layer. Then the biocompatibility of Ti-Nb alloy at the surface can be utilized, and the cost can be reduced by avoiding manufacturing the entire part using Ti-Nb alloy. Zhang et al. [59] deposited a series of Ti-2Al-yMo (y = 2, 5, 7, 9, 12) to study the Ti-Al-X system and develop innovative alloys via DED.

2.2.2. FGMs The elemental powder mixture can be used to modify alloys using different compositions of elemental powders. The DED process is also a flexible layer-based AM technique, which can produce different compositions at different locations. Then, within a certain binary or ternary alloy system, different compositions can be joined together by taking a proper usage of the DED process in a layer-wise fashion. More advanced metallic alloys can be designed for multifunctionality, and FGM is a good example. The concept of FGM originated from applying a graded composition between two materials with different properties to avoid delamination under extreme loading conditions at the interface [60]. Compared with selective laser melting (SLM), which is a laser-based metal additive manufacturing in the category of PBF, one important advantage for DED is the flexibility of in-situ control of the location-dependent chemical composition. The flexibility in composition control makes DED an excellent processing technique for fabricating FGMs [60]. DED can be fully utilized to deposit different compositions of elemental powder mixtures layer by layer without using complicated assembly processes in traditional manufacturing. One purpose of fabricating FGMs is to join two dissimilar pure alloys without a sharp interface [61,62,63,64]. This could be solved by adding compositionally graded interlayers between pure alloy A and pure alloy B. Figure 3 illustrates the concept of joining based FGM, and a real deposited sample from the literature [61] is shown in Figure 4, which joins Inconel 625 and 304L stainless steel via a compositional gradient.

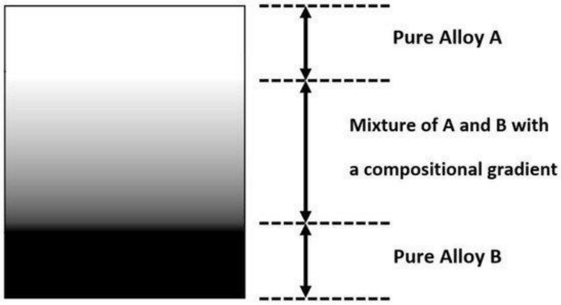

Figure 3. FGM joined by pure alloy A and pure alloy B with a compositional gradient.

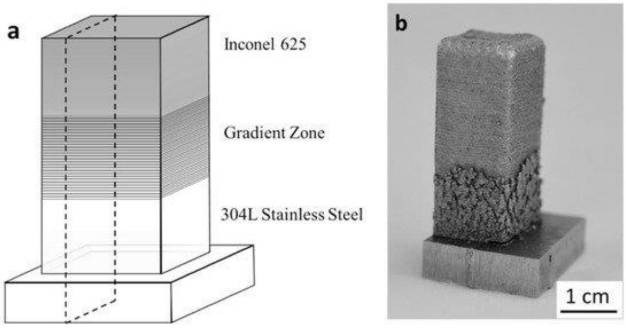

Figure 4. (a) Schematic of Inconel 625/304L stainless steel FGM. (b) Image of an Inconel 625/304L stainless steel FGM sample fabricated by DED [61]. (Reproduced with permission from Elsevier).

In addition, FGMs can be intentionally designed by combining different chemical compositions at different locations to fabricate multifunctional parts. This type of FGM has been done in using the DED method to fabricate binary or ternary alloy systems with a compositional gradient via elemental powder mixture. Banerjee et al. have made a decent amount of Ti-based binary alloys into FGMs using elemental powders, including Ti-V [65,66], Ti-Mo [66], and Ti-Ta [67]. Titanium can form α/β alloy systems with many other metal elements. As seen in Figure 5, a Ti/V FGM was fabricated by mixing graded Ti/V composition and the resultant composition gradient varies from 100% Ti on the left to 75 at.% Ti/25 at.% V on the right side. It is of great interest to apply elemental powder to study graded titanium alloys and identify their process-structure-property relations since many Ti-based binary alloys have not been widely considered in the AM category. Elemental powder mixture will be convenient to check the effect of alloying elements on microstructure, grain size, and mechanical properties. Those works focused on the relationship among composition, microstructure, and mechanical properties of Ti-based binary alloys with a composition change along the graded direction. Here the research in DED-processed FGMs also helps to establish the process-structure-property relationship of these promising alloy systems. Ti-Cr [68], Ti-Al [69], Ti-W [70], and Ti-Mo [71] systems were also investigated. Details are tabulated in Table 1. W element is good for grain refinement, while Mo does not have a significant refining effect. They also studied the Ti-Al-V system by varying the composition of V using the elemental powder mixture of Ti-8Al-xV [72]. Thus, graded ternary alloys can also be fabricated using DED to systematically study the effect of variation of alloying elements.

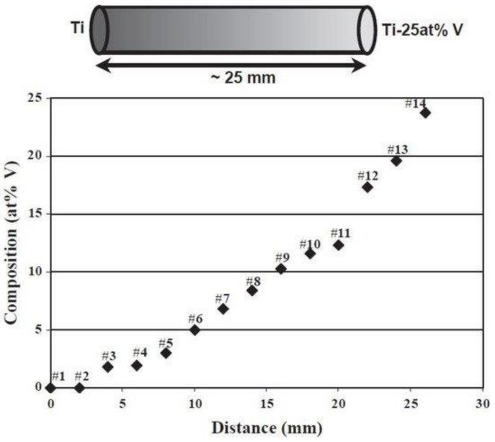

Figure 5. Schematic diagram of Ti-25 at.%V FGM alloy fabricated via elemental powder mixture and the compositional variation vs. distance [65]. (Reproduced with permission from Elsevier).

Table 1. Summary of Ti-based FGM alloys fabricated by elemental powder-based DED.

Alloy System	**Ref.**	**Composition**	**Findings**
Ti-Mo	[66]	Ti-25 at.% Mo	Hardness first increased and then decreased, a combination of grain size and alloy content.
Ti-Ta	[67]	Ti-50 wt.% Ta	The microhardness initially decreases, then increases, and finally decreases again.
Ti-Cr	[68]	Ti-60 at.% Cr	Hardness and modulus increase with Cr composition.
Ti-W	[70]	Ti-23 wt.% W	W has a significant effect of grain refinement across the gradient.

Karnati et al. [73] mixed elemental Cu and Ni powders to create Cu-Ni FGMs based on the complete solubility in Cu-Ni binary system. After the previous investigation of mixing Cu and Ni in different compositions, the different compositions were then combined and fabricated into Cu/Ni FGM. Li et al. [74,75] fabricated a new graded Fe-Cr-Ni alloy using Fe, Cr, and Ni elemental powders with a gradient in Cr and Ni composition, as shown in Figure 6. Thus, on the Cr-rich side, the graded system can exhibit excellent behaviors in corrosion resistance. On the Ni-rich side, the system possesses high plasticity owing to the large composition of austenite.

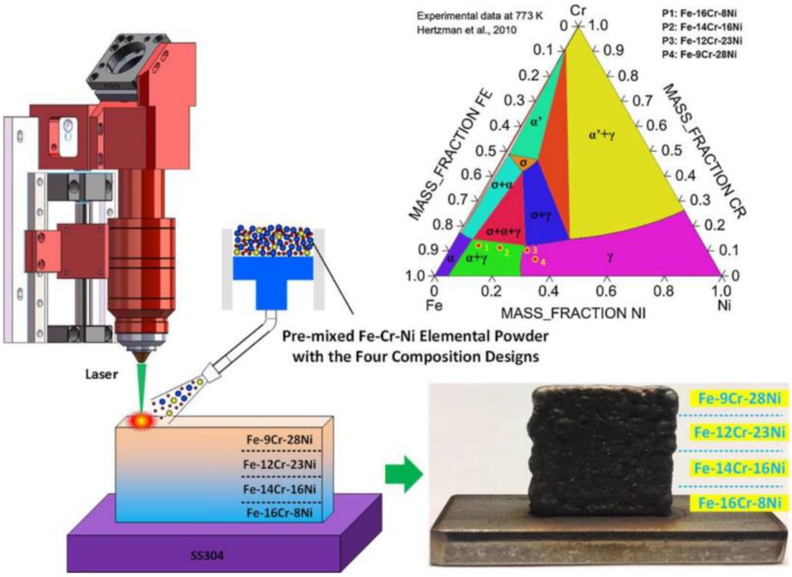

Figure 6. Fabricating Fe-Cr-Ni FGM by DED process using elemental Fe, Cr, and Ni powders [74]. (Reproduced with permission from Elsevier).

2.2.3. Magnetic Materials and Metallic Glass Apart from common structural alloys, new types of alloy systems with special functions were also studied using elemental powder blend. Conteri et al. [76] studied a novel magnetic alloy Fe73.5Si13.5B9Nb3Cu1. Based on this study, Borkar et al. [77] synthesized a more complex magnetic alloy with a gradually changing Si/B ratio. Thus, this new design is also known as a functionally graded Fe-Si-B-Cu-Nb alloy with magnetic properties. Amorphous (or glassy) metals can be fabricated using this technique. Manna et al. [78] deposited 94Fe4B2C, 75Fe15B10Si, and 78Fe10BC9Si2Al1C by mixing glass-forming elemental powders on a substrate made by carbon steel. While in Hou et al.'s work [79], the Fe-based Fe-Cr-Mo-Co-C-B amorphous alloy was produced according to the weight percentage of Fe45.8Mo24.2Cr14.7Co7.8C3.2B4.3. The amorphous phase occupied 52.8% of the entire volume. The resulted hardness of the deposition has a maximum of 1200 HV0.5, which shows a significant improvement compared to the substrate that is 200 HV0.5.

2.2.4. HEAs HEA was also proved to be feasible to be fabricated by DED using elemental powders. HEAs are known to possess high hardness, excellent high-temperature strength, corrosion resistance, and wear resistance due to the unique multiprincipal element composition [80]. It is promising for fabricating coating materials on engineering parts for wear and oxidation resistance. As the flexible mixture of powders from at least five principal elements, different atomic ratios can be varied to study the element effect on the as-fabricated HEAs, such as $Al_xCrCuFeNi$ [81], where x varies while the atomic percentage of all five elements are between 5 at.% and 35 at.%.

Coating HEAs on conventional structural alloys are highly attractive due to the potential high hardness of HEAs. Cui et al. [82] applied DED to coat AlCoCrFeNi on AISI SS316 using the elemental powders. An intermediate $CoFe_2Ni$ layer was applied between the AlCoCrFeNi HEA coating and the SS316 substrate to avoid cracking. The intermediate $CoFe_2Ni$ was also synthesized by elemental powder, which has the purpose of providing an average coefficient of thermal expansion (CTE) that does not differ greatly from the SS316 substrate and the HEA coating. Chao et al. [83] applied DED to coat $Al_xCoCrFeNi$ on a 253MA steel substrate, where the value of the Al mole fraction x was taken as 0.3, 0.6, and 0.85. Elemental powders were utilized, and the composition change of Al can be adjusted. The effect of the Al mole fraction on the crystal structure was revealed by material characterization. Chen et al. [84] varied two types of elements (Al and Cu) to study the influence on the structure and properties of $Al_xCoFeNiCu_{1-x}$, where x = 0.25, 0.5, and 0.75. It was found that crystal structure and hardness varied significantly from 0.25 Al/0.75 Cu to 0.75 Al/0.25 Cu. In another work, the hardness of Al alloy was improved by depositing $Al_{0.5}FeCu_{0.7}NiCoCr$ HEA coating [85]. The average value of hardness reached about eight times higher than the Al alloy substrate.

In addition, HEAs that possess high erosion and oxidation resistance can be synthesized by elemental powder mixture. Siddiqui et al. [86] coated $Al_xCu_{0.5}FeNiTi$ HEA on Al alloy AA1050 by elemental powder blend for erosion resistance. It was stated that the erosion rate was decreased mainly due to the improved microhardness of tough grains formed in HEA. The HEA coating using elemental powder is also studied for the potentially high-temperature oxidation resistance. Huang et al. [87] studied that depositing TiVCrAlSi on Ti-6Al-4V can improve the oxidation resistance of Ti-6Al-4V at 800 °C.

As high temperature fields can be created by the high-power laser beam, some works that focus on combining a series of metal elements with high melting points to produce refractory HEAs were also carried out. Dobbelstein et al. [88] produced TiZrNbHfTa from elemental powder blends for the first time. The mixing was homogeneous, and a high hardness was achieved. The effect of the mole fraction of one specific element was also studied. The $W_xNbMoTa$ HEA with the composition change in W was fabricated by Li et al. [89]. The mole fraction x was taken as 0, 0.16, 0.33, and 0.53. It was found the microhardness increases with the increase in W. Based on the flexibility in modifying the mole fraction, different HEAs with different mole fractions can also be fabricated together to make FGMs, which then becomes compositionally graded HEAs. By taking advantage of FGM, Dobbelstein et al. [90] also fabricated compositionally graded TiZrNbTa refractory HEAs using elemental powder blends. Gwalani et al. [91] deposited $AlCrFeMoV_x$ compositionally graded HEA, where the mole fraction of V varies from 0 to

1. The lattice parameter decreased, and an improvement was found on hardness with the increase in V content. DED with elemental powders was regarded as a high-throughput method to study the composition-microstructure-hardness relationship of novel HEAs.

3. DEPOSITION CONTROL

In Section 2, major types of alloys which have been fabricated by elemental powder based DED technique are introduced and discussed. The classification and examples with the reference are tabulated in Table 2. Using elemental powders to fabricate various types of alloys using DED is now very promising. However, as a novel technique, there are still a lot of unsolved issues beyond feasibility studies to popularize this concept. Whether the composition of the deposited part matches up with the originally designed composition is a big issue for this technique. Also, the final deposition is expected to be homogeneous. As the entire feedstock delivery and manufacturing system are highly complex, multiple key factors should be taken into consideration. The stability and repeatability are of great importance to promote this process into a new stage in various industries.

3.1. ENTHALPY OF MIXING

Mixing is important to maintain a good homogeneity during the deposition. To ensure a uniform mixing, the enthalpy of mixing of the system should be negative. Schwendner et al. [92] used Ti-Cr and Ti-Nb binary elemental powder blend to study the effect of mixing enthalpy on the homogeneity of mixing. The results showed that Ti-10%Cr alloy has a negative enthalpy of mixing and has a homogeneous intermixing result within the melt pool. While the Ti-10%Nb system has an inhomogeneous mixing and a slow cooling rate. The mixing of enthalpy can be a useful criterion to guide the design of chemical elements in the alloy. For some of the alloy systems, the constituent elements are in the positive enthalpy of mixing, such as Cu-Ni [56] and Cu-Fe, the adjustment of laser power to generate additional energy for mixture homogenization is needed. For example, Karnati et al. [56] applied pulse width modulated laser power to induce vibrations in the melt pool to avoid segregation during the deposition of the Cu-Ni system.

3.2. POWDER DELIVERY

Although using the elemental powder blend is straightforward to understand, the accuracy of the chemical composition of the as-deposited part is a big challenge. The pre-designed chemical compositions or elemental composition should match well with the deposited part. Element deviations are often observed from most of the previously reported works. Among those works, few of them made an in-depth investigation in this aspect. In [56], blending Ni and Cu resulted in the part with a 4% error with respect to the pre-designed composition. In [82], the atomic percentage of Al in AlCoCrFeNi HEA was between 10 at.% and 15 at.%, while the pre-designed atomic percentage was 20 at.%. In some cases, fabricating the material system with high compositional accuracy is of great importance. A small composition error can cause a significant change in microstructure, phase, and mechanical properties. For example, a slight increase in the Mo composition of Ti-Mo alloy will result in a bimodal distribution of α lath in the β matrix [66]. The control of chemical composition needs to be solved in order to improve the manufacturing quality of the elemental DED process and push this method entirely in the industrial applications.

Table 2. Classification of alloys synthesized by elemental powder-based DED.

Alloy Types	**Examples**	**Ref.**
Industrial Alloys	Ti-6Al-4V	[33,34,35,36]
	Stainless Steel	[37]
Intermetallics	FeAl	[39]
	NiTi	[44,45,46,47,48,49]
	Ni_3Al	[50]
	Hard Coadings: TiCo, Cr_3Si, NiSi, etc.	[51,52,53,54,55]
FGMs	Ti-based: Ti-Mo, Ti-V, Ti-Ta, etc.	[68,69,70,71,72]
	Cu-Ni	[73]
	Fe-Cr-Ni	[74,75]
Magnetic Alloys	Fe73.5Si13.5B9Nb3Cu1 etc.	[76,77]
Metallic Glass	78Fe10BC9Si2Al1C etc.	[78,79]
HEAs	Al_xCrCuFeNi etc.	[81,82,83,84,85,86,87,88,89,90,91]

Powders are the commonly used feedstock material for the DED process. Most of the previous works applied the method of blown powder blend of pre-mixed elemental powders to deliver powders into the melt pool with the carrier gas. Since elemental powders made by different metals are mixed and delivered by carrier gas, the powder properties, and flow behavior are important to control. Collins et al. [93] mentioned that powder size and density could affect the actual composition of the as-deposited part in their work of fabricating Ti-Al-Mo and Ti-Al alloys. Li et al. systematically studied powder separation using both numerical and experimental methods [94,95,96]. As the powder mixture is delivered by the carrier gas, the velocity of each particle mainly depends on its shape, density, and size. Li performed studies in exploring the powder segregation in the blown powder DED process with pre-mixed spherical elemental powder as feedstocks, as seen in Figure 7. The larger the difference in density, the greater the segregation phenomenon will be. Cu and Al powders were applied for the experimental investigation of the flow behavior. In the investigation, it was found that significant segregation was observed in un-sieved powder mixtures without size adjustment. The segregation issue was resolved after the sieving process under the guidance of the density and size relation. The limitation of this model is it only works for spherical powder particles. For non-spherical powders, the flowability will be changed, and more studies are needed.

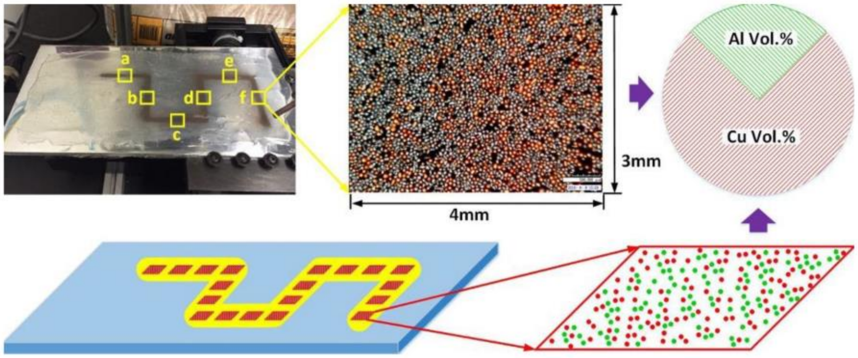

Figure 7. Investigation of powder segregation between Al powder and Cu powder by spraying powder mixture on a glue plate and calculating the volume ratio of Al powder and Cu powder at different locations [96]. (Reproduced with permission from Elsevier).

3.3. CAPTURING AND MELTING

When a real deposition is performed, a stream of powder is blown into the melt pool, and only part of the powder can be captured by the melt pool. The capture rate is also a factor to affect the chemical composition, as for different types of powders, the probability of falling into the melt pool also varies. Chen et al. [36] performed an experiment to investigate the powder capture rate of Ti, Al, and V at different size levels. For each metal powder, a constant capture rate can be determined, and the corresponding size level can be picked for the same capture rate. Another perspective for keeping a constant capture rate for different metal powders is to maintain a constant divergence angle to maintain a consistent composition before and after deposition. A mathematical model was worked out by Zhang et al. [97]. The constant divergence is a reflection of constant speed out of the nozzle. The optimized powder particle size of Ti, Al, and V used to maintain a constant divergence angle match nicely with Li's work [94].

The study of the flow behavior by Li et al. [96] revealed the relationship between powder properties and the avoidance of powder separation. However, it was limited in powder spray. The actual laser deposition was not performed to check the exact elemental composition of the as-deposited part. As when an actual deposition is performed, different metals may have different composition loss due to evaporation. The melt pool capture rate of powders can also be different. In the research [74,75] of the Fe-Cr-Ni FGM, Li et al. applied this method and found that the deposition works better when the powder size was sieved and controlled according to the physical properties of Fe, Cr, and Ni, as shown in Figure 8. Fe, Cr, and Ni have relatively similar density and melting point, the effect of evaporation and capture rate will be less obvious. For other combinations with larger differences in properties, such as Cu and Al differ greatly in density and melting temperature, further works should be done for this model extension.

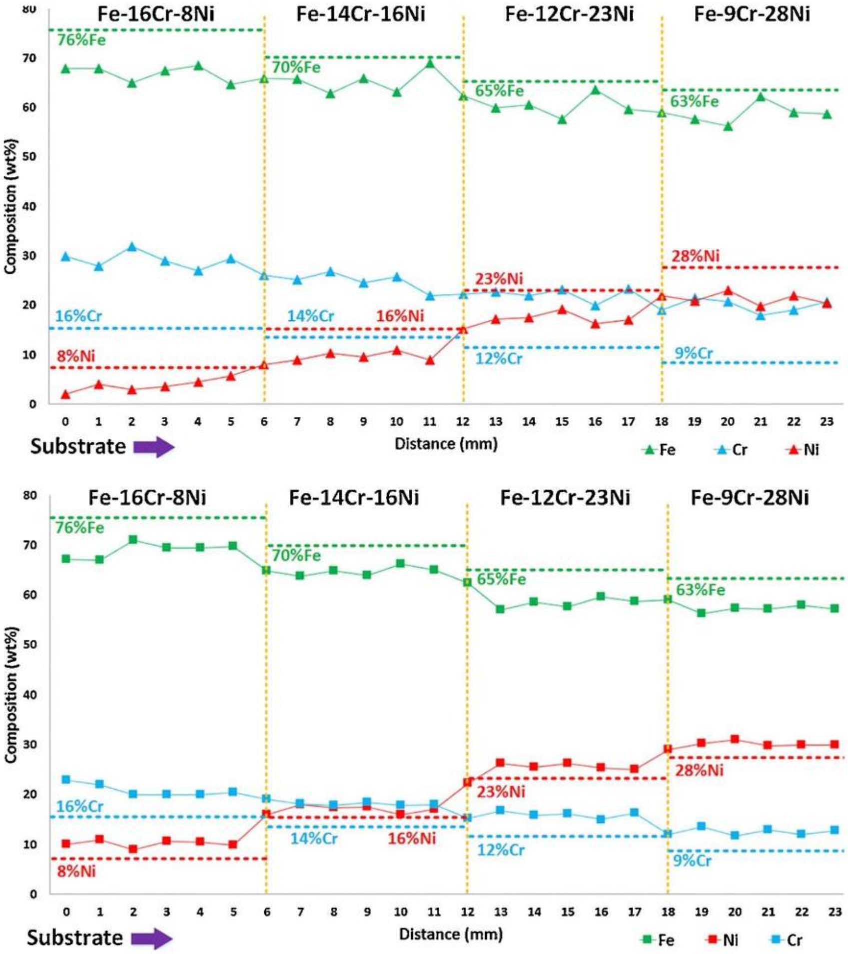

Figure 8. Element composition control of Fe-Cr-Ni FGM with un-sieved (the upper figure) and sieved (the lower figure) elemental powder mixture. The FGM fabricated by sieved powder mixture gives more accurate composition [74]. The percentage indicates wt.% in this figure. (Reproduced with permission from Elsevier).

Therefore, apart from the flow properties of powder particles, the thermal interactions are also complex, which may affect the composition, microstructure, and performance. Metal elements cover a wide range of physical properties such as density, melting point, and laser absorption rate. For instance, among engineering structural alloys, the melting point can span from 600 °C in Al to 3400 °C in W [91]. The energy absorption rate is also worth considering when a highly reflected element, such as Cu, is part of the alloy [98]. In SLM work, a refractory HEA comprises of NbMoTaW was deposited [99]. A 3.5% composition deviation was found. Although the element composition of 5%–35% can all be regarded as HEA, how this deviation can affect the phase evolution and the final properties are still unknown at this moment. In [90], a new processing of DED was applied to deposit a functionally graded refractory HEA, which includes a wide range of melting points. The newly designed process route consists of a low power step to yield low powder evaporation and a high power step to remelt the previous layer and homogenize the elements. In Figure 9, Figure 9a,b are single track deposition and deposition track after the second remelting step, respectively. Figure 9d,e are EDS mapping of elements (Zr, Nb, Ti, Ta, and the substrate Mo) of Figure 9a,b respectively. From the EDS mapping, it can be seen that the remelting step strongly homogenizes the refractory elements within the entire deposition.

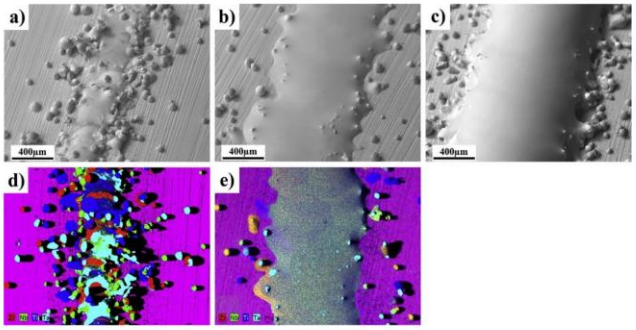

Figure 9. Deposition of TiZrNiTa refractory HEA on Mo substrate: (a) Single-track deposition; (b) Deposition after the second remelting step; (c) Deposition after four deposition and remelting steps; (d) The EDS mapping of deposition in (a) and (e) The EDS mapping of deposition in (b) [90]. (Reproduced with permission from Elsevier).

4. OUTLOOK

Based on the major factors discussed in Section 3, it can be concluded that keeping an accurate composition in elemental powder deposition is still challenging. Those factors were partially studies in a couple of previous works. Each factor needs more experimental and theoretical studies. For blown powder-based DED, it was reported that linearly varying flow parameters can still result in nonlinear compositional grading and material behaviors [66]. The model of powder delivery using carrier gas needs to be further improved. Multiple factors, including the elemental powder properties and the processing parameters, are quite relevant, and the interactions among them are not negligible. It was reported that nano-sized powders were applied in high velocity oxygen fuel (HVOF) coating technique [100], which applies powder spray to fabricate thin layers. The delivery of powders with a more tiny size can be further studied that the DED process can be extended to more precise manufacturing applications. For thin layer deposition, preplacing powders on the processing surface before laser melting is another way to obtain a strong metallurgical bonding [50,51,52,53,54]. The dilution analysis can be further investigated to control the resultant phases after the deposition process.

There are very few works that cover the tolerance of chemical compositions of alloys fabricated by DED using elemental powders. Then, the compositional sensitivity study can be an important topic to study for the industry to adopt this processing method. It is worth mentioning that one advantage for elemental powder DED is that the mass loss due to evaporation can be compensated [36]. For pre-alloyed powders, since all the particles are in the same composition, if elements such as Mg, Zn, and Al are included, the favorable evaporation during the laser processing will change the overall composition. So, there is a need to compensate for this loss in pre-alloyed powders. However, for elemental powder mixture, more volatile elements can be prepared in the pre-designed powder mixture by adding more volatile element powders. Mukherjee et al. [101] listed some examples of the most volatile elements in some common alloys. Depositing pre-alloyed Ti-6Al-4V has a large loss in Al. It was reported the percentage of Al loss in pre-alloyed Ti-6Al-4V is higher than Cr loss in Inconel 625. If using elemental powders, various compositions can be pre-mixed to compensate for easy-to-evaporate alloy elements. An early compensation study was performed by Yan et al. [34]. During the first experiment, the pre-designed composition was equal to Ti-6Al-4V, the ideal value. However, the result gives Ti-5Al-2V. Later, a Ti-8Al-8V composition was pre-designed, and the result matched well with Ti-6Al-4V. More details for the compensation study in different alloy systems should be performed in future works, which is a challenging issue. A more mature relationship between the pre-mixed composition and the deposited composition should be studied. Another example is NiTi, which is very sensitive when there is a slight deviation in compositions. There is a need to figure out how to adjust the pre-designed composition in order to get an acceptable chemical composition.

Apart from obtaining an accurate composition, since the process is layer by layer, the heating and cooling history varies at different locations. Also, to build a bulk part, overlaps between tracks cannot be avoided. These are the main features in DED, and the grain structure and the anisotropic mechanical behavior resulted from the layer by layer heating and cooling history have been a hot topic. These features in DED lead to highly dynamic phenomena including dynamic melt pool, particle vaporization, rapid solidification and phase transition. In traditional manufacturing processes, highly dynamic phenomena was found to result in large scattering in mechanical properties [102], and when it comes to DED, the scattering can be more serious. When the feedstock materials become elemental powder mixture, the process will subject to more complex changes and may cause more discrepancies that have not been understood very well. The spatial difference sensitivity is worth learning, and a comprehensive thermophysical model is needed to control the temperature heating and cooling to guide the processing.

As a promising technology which uses elemental powders as feedstock materials, the effect of powder chemistry should be considered in the future study. Powder quality affects the final deposition, and for the DED process, little has known in this area. Powder chemistry, such as the composition of oxygen affects the final part of oxidation sensitive materials such as titanium alloys. Also, the oxidation of powder can induce porosity in the as-built parts. Karnati et al. [56] found the porosity issue in Cu-Ni FGM when using elemental Ni powder. A Ni alloy powder with 96 wt.% Ni and a small amount of Si was used as a substitution of pure Ni powder since Si can consume oxygen and relieve the porosity issue. Powder recycling is attracting research interest in recent years, which is also relevant to this area.

Last but not least, other related AM processing methods based on elemental powders, and the difference between elemental powder-based DED alloys and conventionally manufactured alloys are also worth further study. Nowadays, many important industrial alloys, such as Ti-6Al-4V and NiTi can be manufactured by both conventional methods and AM. The room-temperature mechanical properties of the as-fabricated Ti-6Al-4V using powder mixture were better than wrought counterparts [33]. In

AM, selective laser melting (SLM) and electron beam melting (EBM) can also apply elemental powder mixtures. Wang et al. [49] found out the result of using SLM to fabricate NiTi alloy through elemental powders was not similar to DED. It was reported that there was a significant loss in Ti, which resulted in Ni-rich intermetallics as the predominant phase. The fabrication using EBM was not successful, which shows a low printability. Mechanisms and parametric study of SLM and EBM can be very different from DED based elemental powder manufacturing [49]. Studying in this aspect will give more understanding of the differences between additively manufactured alloys and conventionally manufactured alloys. It will also figure out more advantages of using multiple AM techniques to fabricate alloys by elemental powders in the corresponding industrial area.

5. CONCLUSIONS

In this paper, the current research status of using the DED process to fabricate metal alloys through elemental powder mixture was summarized based on different types of alloys, including industrial alloy and intermetallics synthesis, alloy modification, FGMs, metallic glass, and HEAs. The main issues and challenges are also summarized.

Various types of alloys, including industrial alloys, FGMs, metallic glass, and HEAs, have been synthesized by DED through elemental powders. Many of those works show good feasibility, and the mechanical properties of the deposited parts are comparable to conventionally manufactured alloys. As a new technique, numerous topics are still unsolved. Main scientific issues like overcoming the entropy of mixing, studying the physical and chemical properties of powders, the flow behavior for different metal powders, and how the laser-material interaction affect the final composition of the as-built part need systematic and in-depth research. Also, a relationship between the initial designed atomic or weight composition and the final composition is needed, and it will be integrated with the knowledge of materials science, dynamics, thermomechanical interaction, and the manufacturing system. Numerical simulation and more experimental results can be done in the future, which will significantly extend this new area to the metal manufacturing industry not only in DED, but also in other AM areas such as SLM and EBM.

FUNDING

This project was supported by National Science Foundation Grants CMMI 1625736, Department of Energy Grant #DE-SC0018879, Intelligent Systems Center, and Material Research Center at Missouri S&T. Their financial support is greatly appreciated.

REFERENCES

1. Frazier, W.E. Metal Additive Manufacturing: A Review. J. Mater. Eng. Perform. 2014, 23, 1917–1928.

2. Huang, Y.; Leu, M.; Mazumder, J.; Donmez, M.A. Additive Manufacturing: Current State, Future Potential, Gaps and Needs, and Recommendations. J. Manuf. Sci. Eng. 2015, 137, 014001.

3. Paris, H.; Mokhtarian, H.; Coatanéa, E.; Museau, M.; Ituarte, I.F. Comparative environmental impacts of additive and subtractive manufacturing technologies. CIRP Ann. 2016, 65, 29–32.

4. Debroy, T.; Wei, H.; Zuback, J.; Mukherjee, T.; Elmer, J.; Milewski, J.; Beese, A.M.; Wilson-Heid, A.; De, A.; Zhang, W. Additive manufacturing of metallic components—Process, structure and properties. Prog. Mater. Sci. 2018, 92, 112–224.

5. Zhang, Y.; Jarosinski, W.; Jung, Y.-G.; Zhang, J. Additive manufacturing processes and equipment. In Additive Manufacturing; Elsevier BV: Oxford, UK, 2018; pp. 39–51.

6. F42 Committee. Standard Guide for Directed Energy Deposition of Metals; ASTM International: West Conshohocken, PA, USA, 2016.

7. Gibson, I.; Rosen, D.; Stucker, B. Directed Energy Deposition Processes. In Additive Manufacturing Technologies; Springer Science and Business Media LLC: New York, NY, USA, 2015; pp. 245–268.

8. Wang, Z.; Palmer, T.A.; Beese, A.M. Effect of processing parameters on microstructure and tensile properties of austenitic stainless steel 304L made by directed energy deposition additive manufacturing. Acta Mater. 2016, 110, 226–235.

9. Melia, M.A.; Nguyen, H.-D.A.; Rodelas, J.M.; Schindelholz, E.J. Corrosion properties of 304L stainless steel made by directed energy deposition additive manufacturing. Corros. Sci. 2019, 152, 20–30.

10. Sciammarella, F.M.; Najafabadi, B.S. Processing Parameter DOE for 316L Using Directed Energy Deposition. J. Manuf. Mater. Process. 2018, 2, 61.

11. Weng, F.; Gao, S.; Jiang, J.; Wang, J.; Guo, P. A novel strategy to fabricate thin 316L stainless steel rods by continuous directed energy deposition in Z direction. Addit. Manuf. 2019, 27, 474–481.

12. Ning, F.; Cong, W. Microstructures and mechanical properties of Fe-Cr stainless steel parts fabricated by ultrasonic vibration-assisted laser engineered net shaping process. Mater. Lett. 2016, 179, 61–64.

13. Kistler, N.A.; Nassar, A.R.; Reutzel, E.W.; Corbin, D.J.; Beese, A.M. Effect of directed energy deposition processing parameters on laser deposited Inconel®718: Microstructure, fusion zone morphology, and hardness. J. Laser Appl. 2017, 29, 022005.

14. Jinoop, A.; Paul, C.; Mishra, S.; Bindra, K. Laser Additive Manufacturing using directed energy deposition of Inconel-718 wall structures with tailored characteristics. Vacuum 2019, 166, 270–278.

15. Kakinuma, Y.; Mori, M.; Oda, Y.; Mori, T.; Kashihara, M.; Hansel, A.; Fujishima, M. Influence of metal powder characteristics on product quality with directed energy deposition of Inconel 625. CIRP Ann. 2016, 65, 209–212.

16. Fujishima, M.; Oda, Y.; Ashida, R.; Takezawa, K.; Kondo, M. Study on factors for pores and cladding shape in the deposition processes of Inconel 625 by the directed energy deposition (DED) method. CIRP J. Manuf. Sci. Technol. 2017, 19, 200–204.

17. Carroll, B.E.; Palmer, T.A.; Beese, A.M. Anisotropic tensile behavior of Ti–6Al–4V components fabricated with directed energy deposition additive manufacturing. Acta Mater. 2015, 87, 309–320.

18. Prabhu, A.W.; Vincent, T.; Chaudhary, A.; Zhang, W.; Babu, S.S. Effect of microstructure and defects on fatigue behaviour of directed energy deposited Ti–6Al–4V. Sci. Technol. Weld. Join. 2015, 20, 659–669.

19. Beese, A.M.; Carroll, B.E. Review of Mechanical Properties of Ti-6Al-4V Made by Laser-Based Additive Manufacturing Using Powder Feedstock. JOM 2015, 68, 724–734.

20. Saboori, A.; Gallo, D.; Biamino, S.; Fino, P.; Lombardi, M. An Overview of Additive Manufacturing of Titanium Components by Directed Energy Deposition: Microstructure and Mechanical Properties. Appl. Sci. 2017, 7, 883.

21. Onuike, B.; Bandyopadhyay, A. Additive manufacturing in repair: Influence of processing parameters on properties of Inconel 718. Mater. Lett. 2019, 252, 256–259.

22. Wilson, J.M.; Piya, C.; Shin, Y.C.; Zhao, F.; Ramani, K. Remanufacturing of turbine blades by laser direct deposition with its energy and environmental impact analysis. J. Clean. Prod. 2014, 80, 170–178.

23. Zhang, X.; Cui, W.; Li, W.; Liou, F. Effects of tool path in remanufacturing cylindrical components by laser metal deposition. Int. J. Adv. Manuf. Technol. 2018, 100, 1607–1617.

24. Zhang, X.; Pan, T.; Li, W.; Liou, F. Experimental Characterization of a Direct Metal Deposited Cobalt-Based Alloy on Tool Steel for Component Repair. JOM 2018, 71, 946–955.

25. Zhang, X.; Li, W.; Chen, X.; Cui, W.; Liou, F. Evaluation of component repair using direct metal deposition from scanned data. Int. J. Adv. Manuf. Technol. 2017, 95, 3335–3348.

26. Yu, J.; Rombouts, M.; Maes, G.; Motmans, F. Material Properties of Ti6Al4V Parts Produced by Laser Metal Deposition. Phys. Procedia 2012, 39, 416–424.

27. Jia, M.; Blanchard, C.; Bolzoni, L. Microstructure and Mechanical Properties of Ti-5Al-2.5Fe Alloy Produced by Powder Forging. Key Eng. Mater. 2018, 770, 39–44.

28. Liu, Y.; Chen, L.; Tang, H.; Liu, C.-T.; Liu, B.; Huang, B. Design of powder metallurgy titanium alloys and composites. Mater. Sci. Eng. A 2006, 418, 25–35.

29. Azarniya, A.; Garmendia, X.; Mirzaali, M.J.; Sovizi, S.; Bartolomeu, F.; Mare, K.S.W.; Wits, W.W.; Yap, C.Y.; Ahn, J.; Miranda, G.; et al. Additive manufacturing of Ti–6Al–4V parts through laser metal deposition (LMD): Process, microstructure, and mechanical properties. J. Alloys Compd. 2019, 804, 163–191.

30. Saresh, N.; Pillai, M.G.; Mathew, J. Investigations into the effects of electron beam welding on thick Ti–6Al–4V titanium alloy. J. Mater. Process. Technol. 2007, 192, 83–88.

31. Ivasishin, O.; Anokhin, V.; Demidik, A.; Savvakin, D. Cost-Effective Blended Elemental Powder Metallurgy of Titanium Alloys for Transportation Application. Key Eng. Mater. 2000, 188, 55–62.

32. Wang, H.; Fang, Z.Z.; Sun, P. A critical review of mechanical properties of powder metallurgy titanium. Int. J. Powder Metall. 2010, 46, 45–57.

33. Hua, T.; Jing, C.; Fengying, Z.; Xin, L.; Huang, W. Microstructure and Mechanical Properties of Laser Solid Formed Ti-6Al-4V from Blended Elemental Powders. Rare Met. Mater. Eng. 2009, 38, 574–578.

34. Yan, L.; Chen, X.; Li, W.; Newkirk, J.; Liou, F. Direct laser deposition of Ti-6Al-4V from elemental powder blends. Rapid Prototyp. J. 2016, 22, 810–816.

35. Chen, X.; Yan, L.; Li, W.; Wang, Z.; Liou, F.; Newkirk, J. Effect of Powder Particle Size on the Fabrication of Ti-6Al-4V Using Direct Laser Metal Deposition from Elemental Powder Mixture. J. Mech. Eng. Autom. 2016, 6, 348.

36. Chen, X. Fabrication and Characterization of Advanced Materials Using Laser Metal Deposition from Elemental Powder Mixture. Ph.D. Thesis, Missouri University Of Science And Technology, Rolla, MO, USA, 2018.

37. Clayton, R.M. The Use of Elemental Powder Mixes in Laser-Based Additive Manufacturing. Master’s Thesis, Missouri University Of Science And Technology, Rolla, MO, USA, 2013.

38. Karczewski, K.; Pęska, M.; Ziętala, M.; Polański, M.; Dąbrowska, M. Fe-Al thin walls manufactured by Laser Engineered Net Shaping. J. Alloys Compd. 2017, 696, 1105–1112.

39. Pęska, M.; Karczewski, K.; Rzeszotarska, M.; Polański, M. Direct Synthesis of Fe-Al Alloys from Elemental Powders Using Laser Engineered Net Shaping. Materials 2020, 13, 531.

40. Mwangi, J.W.; Nguyen, L.T.; Bui, V.D.; Berger, T.; Zeidler, H.; Schubert, A. Nitinol manufacturing and micromachining: A review of processes and their suitability in processing medical-grade nitinol. J. Manuf. Process. 2019, 38, 355–369.

41. Krishna, B.V.; Bose, S.; Bandyopadhyay, A. Laser Processing of Net-Shape NiTi Shape Memory Alloy. Met. Mater. Trans. A 2007, 38, 1096–1103.

42. Marattukalam, J.J.; Singh, A.K.; Datta, S.; Das, M.; Balla, V.K.; Bontha, S.; Kalpathy, S.K. Microstructure and corrosion behavior of laser processed NiTi alloy. Mater. Sci. Eng. C 2015, 57, 309–313.

43. Baran, A.; Polański, M. Microstructure and properties of LENS (laser engineered net shaping) manufactured Ni-Ti shape memory alloy. J. Alloys Compd. 2018, 750, 863–870.

44. Halani, P.R.; Shin, Y.C. In Situ Synthesis and Characterization of Shape Memory Alloy Nitinol by Laser Direct Deposition. Met. Mater. Trans. A 2011, 43, 650–657.

45. Shiva, S.; Palani, I.; Mishra, S.; Paul, C.; Kukreja, L.M. Investigations on the influence of composition in the development of Ni–Ti shape memory alloy using laser based additive manufacturing. Opt. Laser Technol. 2015, 69, 44–51.

46. Bimber, B.A.; Hamilton, R.F.; Palmer, T.A. Ni-Concentration Dependence of Directed Energy Deposited NiTi Alloy Microstructures. Shape Mem. Superelasticity 2019, 5, 182–187.

47. Bimber, B.A.; Hamilton, R.F.; Keist, J.; Palmer, T.A. Anisotropic microstructure and superelasticity of additive manufactured NiTi alloy bulk builds using laser directed energy deposition. Mater. Sci. Eng. A 2016, 674, 125–134.

48. Hamilton, R.F.; Bimber, B.A.; Palmer, T.A. Correlating microstructure and superelasticity of directed energy deposition additive manufactured Ni-rich NiTi alloys. J. Alloys Compd. 2018, 739, 712–722.

49. Wang, C.; Tan, X.; Du, Z.; Chandra, S.; Sun, Z.; Lim, C.; Tor, S.; Lim, C.; Wong, C.H. Additive manufacturing of NiTi shape memory alloys using pre-mixed powders. J. Mater. Process. Technol. 2019, 271, 152–161.

50. Yu, Y.; Zhou, J.; Chen, J.; Zhou, H.; Guo, C.; Guo, B. Preparation, microstructure and tribological properties of Ni3Al intermetallic compound coating by laser cladding. Intermetallics 2010, 18, 871–876.

51. Xue, Y.; Wang, H. Microstructure and wear properties of laser clad TiCo/Ti2Co intermetallic coatings on titanium alloy. Appl. Surf. Sci. 2005, 243, 278–286.

52. Wang, H.M.; Liu, Y.F. Microstructure and wear resistance of laser clad Ti5Si3/NiTi2 intermetallic composite coating on titanium alloy. Mat. Sci. Eng. A-Struc. 2002, 338, 126–132.

53. Wang, H.; Duan, G. Wear and corrosion behavior of laser clad Cr3Si reinforced intermetallic composite coatings. Intermetallics 2003, 11, 755–762.

54. Wang, H.; Wang, C.; Cai, L. Wear and corrosion resistance of laser clad Ni2Si/NiSi composite coatings. Surf. Coat. Technol. 2003, 168, 202–208.

55. Zhong, M.; Liu, W.; Zhang, Y.; Zhu, X. Formation of WC/Ni hard alloy coating by laser cladding of W/C/Ni pure element powder blend. Int. J. Refract. Met. Hard Mater. 2006, 24, 453–460.

56. Karnati, S.; Liou, F.F.; Newkirk, J.W. Characterization of copper–nickel alloys fabricated using laser metal deposition and blended powder feedstocks. Int. J. Adv. Manuf. Technol. 2019, 103, 239–250.

57. Li, C.; Ma, S.; Liu, X.; Li, J.; Le, G. Microstructures and properties of 80W-20Fe alloys prepared using laser melting deposition process. Int. J. Refract. Met. Hard Mater. 2018, 77, 113–119.

58. Fallah, V.; Corbin, S.F.; Khajepour, A. Process optimization of Ti–Nb alloy coatings on a Ti–6Al–4V plate using a fiber laser and blended elemental powders. J. Mater. Process. Technol. 2010, 210, 2081–2087.

59. Zhang, F.; Yang, M.; Clare, A.; Lin, X.; Tan, H.; Chen, Y. Microstructure and mechanical properties of Ti-2Al alloyed with Mo formed in laser additive manufacture. J. Alloys Compd. 2017, 727, 821–831.

60. Chen, Y.; Liou, F. Additive Manufacturing of Metal Functionally Graded Materials: A Review. In Proceedings of the 29th Annual International Solid Freeform Fabrication Symposium, Austin, TX, USA, 13–15 August 2018.

61. Carroll, B.E.; Otis, R.; Borgonia, J.P.; Suh, J.-O.; Dillon, R.P.; Shapiro, A.A.; Hofmann, U.C.; Liu, Z.-K.; Beese, A.M. Functionally graded material of 304L stainless steel and inconel 625 fabricated by directed energy deposition: Characterization and thermodynamic modeling. Acta Mater. 2016, 108, 46–54.

62. Liu, Y.; Liu, C.; Liu, W.; Ma, Y.; Zhang, C.; Cai, Q.; Liu, B. Microstructure and properties of Ti/Al lightweight graded material by direct laser deposition. Mater. Sci. Technol. 2017, 34, 945–951.

63. Schneider-Maunoury, C.; Weiss, L.; Acquier, P.; Boisselier, D.; Laheurte, P. Functionally graded Ti6Al4V-Mo alloy manufactured with DED-CLAD® process. Addit. Manuf. 2017, 17, 55–66.

64. Bobbio, L.D.; Otis, R.; Borgonia, J.P.; Dillon, R.P.; Shapiro, A.A.; Liu, Z.-K.; Beese, A.M. Additive manufacturing of a functionally graded material from Ti-6Al-4V to Invar: Experimental characterization and thermodynamic calculations. Acta Mater. 2017, 127, 133–142.

65. Banerjee, R.; Collins, P.; Bhattacharyya, D.; Fraser, H. Microstructural evolution in laser deposited compositionally graded α/β titanium-vanadium alloys. Acta Mater. 2003, 51, 3277–3292.

66. Collins, P.; Banerjee, R.; Fraser, H. Laser deposition of compositionally graded titanium–vanadium and titanium–molybdenum alloys. Mater. Sci. Eng. A 2003, 352, 118–128.

67. Nag, S.; Banerjee, R.; Fraser, H.L. A novel combinatorial approach for understanding microstructural evolution and its relationship to mechanical properties in metallic biomaterials. Acta Biomater. 2007, 3, 369–376.

68. Zhang, Y.; Meacock, C.; Vilar, R. Laser powder micro-deposition of compositional gradient Ti–Cr alloy. Mater. Des. 2010, 31, 3891–3895.

69. Shishkovsky, I.; Missemer, F.; Smurov, I. Direct Metal Deposition of Functional Graded Structures in Ti- Al System. Phys. Procedia 2012, 39, 382–391.

70. Mendoza, M.Y.; Samimi, P.; Brice, D.A.; Martin, B.; Rolchigo, M.R.; Lesar, R.; Collins, P. Microstructures and Grain Refinement of Additive-Manufactured Ti-xW Alloys. Met. Mater. Trans. A 2017, 48, 3594–3605.

71. Mendoza, M.Y.; Samimi, P.; Brice, D.A.; Ghamarian, I.; Rolchigo, M.; Lesar, R.; Collins, P. On the role of composition and processing parameters on the microstructure evolution of Ti-xMo alloys. BMC Chem. 2019, 13, 1–8.

72. Banerjee, R.; Bhattacharyya, D.; Collins, P.; Viswanathan, G.; Fraser, H. Precipitation of grain boundary α in a laser deposited compositionally graded Ti–8Al–xV alloy—An orientation microscopy study. Acta Mater. 2004, 52, 377–385.

73. Karnati, S.; Zhang, Y.; Liou, F.; Newkirk, J. On the Feasibility of Tailoring Copper–Nickel Functionally Graded Materials Fabricated through Laser Metal Deposition. Metals 2019, 9, 287.

74. Li, W.; Yan, L.; Chen, X.; Zhang, J.; Zhang, X.; Liou, F. Directed energy depositing a new Fe-Cr-Ni alloy with gradually changing composition with elemental powder mixes and particle size’ effect in fabrication process. J. Mater. Process. Technol. 2018, 255, 96–104.

75. Li, W.; Chen, X.; Yan, L.; Zhang, J.; Zhang, X.; Liou, F. Additive manufacturing of a new Fe-Cr-Ni alloy with gradually changing compositions with elemental powder mixes and thermodynamic calculation. Int. J. Adv. Manuf. Technol. 2017, 95, 1013–1023.

76. Conteri, R.; Borkar, T.; Nag, S.; Jaeger, D.; Chen, X.; Ramanujan, R.; Banerjee, R. Laser additive processing of Fe-Si-B-Cu-Nb magnetic alloys. J. Manuf. Process. 2017, 29, 175–181.

77. Borkar, T.; Conteri, R.; Chen, X.; Ramanujan, R.; Banerjee, R. Laser additive processing of functionally-graded Fe–Si–B–Cu–Nb soft magnetic materials. Mater. Manuf. Process. 2016, 32, 1581–1587.

78. Manna, I.; Majumdar, J.D.; Chandra, B.R.; Nayak, S.; Dahotre, N.B. Laser surface cladding of Fe–B–C, Fe–B–Si and Fe–BC–Si–Al–C on plain carbon steel. Surf. Coat. Technol. 2006, 201, 434–440.

79. Hou, X.; Du, D.; Wang, K.; Hong, Y.; Chang, B. Microstructure and Wear Resistance of Fe-Cr-Mo-Co-C-B Amorphous Composite Coatings Synthesized by Laser Cladding. Metals 2018, 8, 622.

80. Tsai, M.-H.; Yeh, J.-W. High-Entropy Alloys: A Critical Review. Mater. Res. Lett. 2014, 2, 107–123.

81. Cui, W.; Zhang, X.; Li, L.; Chen, Y.; Pan, T.; Liou, F. Fabrication and Characterization of AlxCrCuFeNi2 High-Entropy Alloys Coatings by Laser Metal Deposition. Procedia Manuf. 2019, 39, 509–518.

82. Cui, W.; Karnati, S.; Zhang, X.; Burns, E.; Liou, F. Fabrication of AlCoCrFeNi High-Entropy Alloy Coating on an AISI 304 Substrate via a CoFe2Ni Intermediate Layer. Entropy 2018, 21, 2.

83. Chao, Q.; Guo, T.; Jarvis, T.; Wu, X.; Hodgson, P.; Fabijanic, D. Direct laser deposition cladding of AlxCoCrFeNi high entropy alloys on a high-temperature stainless steel. Surf. Coat. Technol. 2017, 332, 440–451.

84. Chen, X.; Yan, L.; Karnati, S.; Zhang, Y.; Liou, F. Fabrication and Characterization of AlxCoFeNiCu1−x High Entropy Alloys by Laser Metal Deposition. Coatings 2017, 7, 47.

85. Ni, C.; Shi, Y.; Liu, J.; Huang, G. Characterization of Al0.5FeCu0.7NiCoCr high-entropy alloy coating on aluminum alloy by laser cladding. Opt. Laser Technol. 2018, 105, 257–263.

86. Siddiqui, A.; Dubey, A.; Paul, C.P. A study of metallurgy and erosion in laser surface alloying of AlxCu0.5FeNiTi high entropy alloy. Surf. Coatings Technol. 2019, 361, 27–34.

87. Huang, C.; Zhang, Y.; Shen, J.; Vilar, R. Thermal stability and oxidation resistance of laser clad TiVCrAlSi high entropy alloy coatings on Ti–6Al–4V alloy. Surf. Coat. Technol. 2011, 206, 1389–1395.

88. Dobbelstein, H.; Gurevich, E.L.; George, E.P.; Ostendorf, A.; Laplanche, G. Laser metal deposition of a refractory TiZrNbHfTa high-entropy alloy. Addit. Manuf. 2018, 24, 386–390.

89. Li, Q.; Zhang, H.; Li, D.; Chen, Z.; Huang, S.; Lu, Z.; Yan, H. WxNbMoTa Refractory High-Entropy Alloys Fabricated by Laser Cladding Deposition. Materials 2019, 12, 533.

90. Dobbelstein, H.; Gurevich, E.L.; George, E.P.; Ostendorf, A.; Laplanche, G. Laser metal deposition of compositionally graded TiZrNbTa refractory high-entropy alloys using elemental powder blends. Addit. Manuf. 2019, 25, 252–262.

91. Gwalani, B.; Soni, V.; Waseem, O.A.; Mantri, S.A.; Banerjee, R. Laser additive manufacturing of compositionally graded AlCrFeMoVx (x = 0 to 1) high-entropy alloy system. Opt. Laser Technol. 2019, 113, 330–337.

92. Schwendner, I.K.; Banerjee, R.; Collins, P.; Brice, C.A.; Fraser, H.L. Direct laser deposition of alloys from elemental powder blends. Scr. Mater. 2001, 45, 1123–1129.

93. Collins, P.C. A Combinatorial Approach to the Development of Composition-Microstructure-Property Relationships in Titanium Alloys Using Directed Laser Deposition. Ph.D. Thesis, The Ohio State University, Columbus, OH, USA, December 2004.

94. Wei, L. Modeling and Experimental Investigations on Particle Dynamic Behaviors in Laser 3D Printing with Blown Powder. Ph.D. Thesis, Missouri University of Science and Technology, Rolla, MO, USA, 2018.

95. Wei, L.; Zhang, X.; Liou, F. Modeling analysis of argon gas flow rate's effect on pre-mixed powder separation in laser metal deposition process and experimental validation. Int. J. Adv. Manuf. Technol. 2018, 96, 4321–4331.

96. Li, W.; Karnati, S.; Zhang, Y.; Liou, F. Investigating and eliminating powder separation in pre-mixed powder supply for laser metal deposition process. J. Mater. Process. Technol. 2018, 254, 294–301.

97. Zhang, F.; Chen, J.; Tan, H.; Lin, X.; Huang, W. Composition control for laser solid forming from blended elemental powders. Opt. Laser Technol. 2009, 41, 601–607.

98. Asano, K.; Tsukamoto, M.; Sechi, Y.; Sato, Y.; Masuno, S.-I.; Higashino, R.; Hara, T.; Sengoku, M.; Yoshida, M. Laser metal deposition of pure copper on stainless steel with blue and IR diode lasers. Opt. Laser Technol. 2018, 107, 291–296.

99. Zhang, H.; Zhao, Y.; Huang, S.; Zhu, S.; Wang, F.; Li, D. Manufacturing and Analysis of High-Performance Refractory High-Entropy Alloy via Selective Laser Melting (SLM). Materials 2019, 12, 720.

100. Guzanová, A.; Brezinová, J.; Draganovská, D.; Maruschak, P. Properties of coatings created by HVOF technology using micro-and nano-sized powder. Koroze Ochr. Mater. 2019, 63, 86–93.

101. Mukherjee, T.; Zuback, J.S.; De, A.; Debroy, T. Printability of alloys for additive manufacturing. Sci. Rep. 2016, 6, 19717.

102. Maruschak, P.; Konovalenko, I.; Chausov, M.G.; Pylypenko, A.P.; Panin, S.V.; Vlasov, I.V.; Prentkovskis, O. Impact of Dynamic Non-Equilibrium Processes on Fracture Mechanisms of High-Strength Titanium Alloy VT23. Metals 2018, 8, 983.

II. FABRICATING TINICU TERNARY SHAPE MEMORY ALLOY BY DIRECTED ENERGY DEPOSITION VIA ELEMENTAL METAL POWDERS

ABSTRACT

In this paper, a TiNiCu shape memory alloy single-wall structure was fabricated by the directed energy deposition technique with a mixture of elemental Ti, Ni, and Cu powders following the atomic percentage of Ti50Ni45Cu5 to fully utilize the material flexibility of the additive manufacturing process to develop ternary shape memory alloys. The chemical composition, phase, and material properties at multiple locations along the build direction were studied, using scanning electron microscopy, energy-dispersive X-ray spectroscopy, X-ray diffraction, Vickers hardness testing, tensile testing, and differential scanning calorimetry. The location-dependent compositions of martensitic TiNi and austenitic TiNi phases, mechanical properties, and functional properties were investigated in detail. Variations were found in atomic compositions of Ti, Ni, and Cu elements along the build direction due to the complex interaction between elemental powders and laser processing. Good correlations were present among the chemical composition, phase constituent, hardness, and feature of phase transformation temperatures at various locations. The ultimate tensile strength of the as-deposited TiNiCu alloy is comparable with the previously reported additively manufactured TiNi binary alloys. By adding Cu, a much lower thermal hysteresis was achieved, which shows good feasibility of fabricating ternary TiNiCu shape memory alloys, using elemental powders in the directed energy deposition to adjust the thermal hysteresis.

1. INTRODUCTION

Additive manufacturing (AM) has become a novel and essential fabrication method. The layer-based additive feature makes AM more flexible in both geometry and materials [1]. Directed energy deposition (DED) is an AM process that applies an energy source to melt raw materials, such as metal powder or wire, and join them into solid parts [2]. Among various DED-related techniques, laser and powders are commonly used energy sources and raw materials, respectively [2]. Nowadays, as the manufacturing techniques of metal powder is improving, various types of metallic materials and industrial alloys have been made into pre-alloyed powders and thus used in DED, including steels [3,4,5], Inconel [6,7,8], titanium alloys such as Ti-6Al-4V [9,10,11] and aluminum alloys [12,13]. Apart from using a single type of pre-alloyed powder in DED, blending multiple types of powders creates much more possibilities to generate new metallic materials and composites with more advantages and, at the same time, the cost can be reduced [14]. Examples include mixing metallic alloy powders with hard ceramic powders, such as TiC, SiC, and WC [15,16,17,18], to gain high hardness and wear resistance, and blending various types of elemental metal powders to synthesize industrial alloys and novel alloys, such as functionally graded alloys and high entropy alloys [19,20,21,22,23,24]. A schematic diagram for the mechanism of DED using laser and pre-mixed powders is demonstrated in Figure 1.

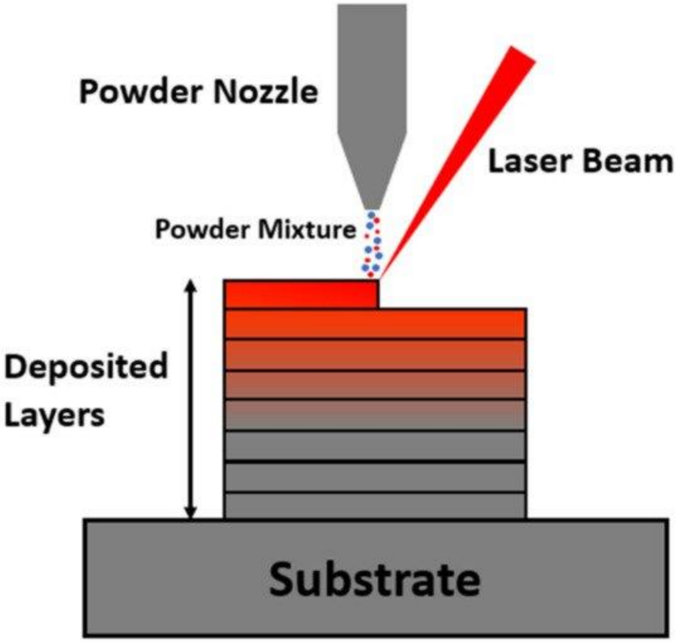

Figure 1. The schematic of laser-based DED with pre-mixed powders as feedstock materials.

TiNi alloy has attracted much more attention in applications in various engineering areas due to its unique shape memory effect and superelastic behavior [25,26]. Researchers have found AM to be a good choice to fabricate TiNi since conventional machining is challenging [27]. Several previous works attempted to fabricate TiNi alloys via pre-alloyed TiNi powders [28,29]. Due to the high cost of producing pre-alloyed TiNi powders, blending Ti and Ni elemental powders has become a novel approach to fabricate TiNi alloys with more flexibility and low cost [27]. It was reported that a small amount of a third metal element could be added to design new ternary shape memory alloys [30]. A good example of metal elements that can act as the third element is Cu. Adding Cu in TiNi alloy to replace a small portion of Ni attracts interest due to its capability to shorten thermal hysteresis, which can be more welcomed in the field of actuator fabrication [30].

According to the high material flexibility of the DED process, adjusting material properties by adding a third element in the Ti–Ni system can be carried out in a more flexible way [31]. However, manufacturing ternary shape memory alloys by DED has not been extensively reported. Shiva et al. [32] attempted to fabricate TiNiCu ternary alloys via the DED process with elemental powders, and they compared material properties among TiNiCu parts with different Cu compositions. However, some special aspects were not reported in detail in [32]. For DED using elemental powders as feedstocks, it is also worth mentioning the inhomogeneity of composition, microstructure, phase formation, and material properties reported in the works of elemental powder-based DED [31]. The DED process can cause anisotropic material behaviors due to its layer-wise fashion [33], and for parts fabricated by DED with an elemental powder mixture, the interaction between the powder mixture and energy is more complex than using pre-alloyed powders [31]. Thus, the composition of the final as-fabricated part can be location dependent with compositional deviations [31]. In [32], the location information and the correlation among chemical compositions, phase, and material behaviors at various locations within an as-fabricated TiNiCu alloy part were not fully described. Therefore, in this work, we use a Ti, Ni, and Cu elemental powder mixture to fabricate a TiNiCu ternary shape memory alloy to find out more about the correlation among the composition, phase, mechanical properties, and functional properties, which could provide a more comprehensive understanding of the structure–property relationship in the TiNiCu ternary shape memory alloy, especially when fabricated by the elemental powder-based DED process.

2. MATERIALS AND METHODS

2.1. MATERIALS

The feedstock for this DED experimental study is a mixture of near-spherical elemental Ti, Ni, and Cu powders. The Ti, Ni, and Cu powders were supplied by AP&C, Atlantic Equipment Engineers, and Royal Metal Powders Inc., respectively. A Hitachi S4700 scanning electron microscope (SEM) was applied to obtain images of powders. SEM images of Ti, Ni, and Cu powders are shown in Figure 2. Those powders were weighted according to the atomic percentage of 50 at.% Ti, 45 at.% Ni, and 5 at.% Cu. The weighted Ti, Ni, and Cu powders were mixed and homogenized using a Turbula T2F powder mixer for 20 min. Grade-2 Ti bar with a dimension of 2 × ½ × ¼ inch was selected as the substrate material. The deposition was performed on the 2 × ½ inch horizontal surface. Before the deposition experiment, the 2 × ½ inch flat surface was ground by sandpapers to remove the surface oxidation layer and wiped with acetone to remove dust particles.

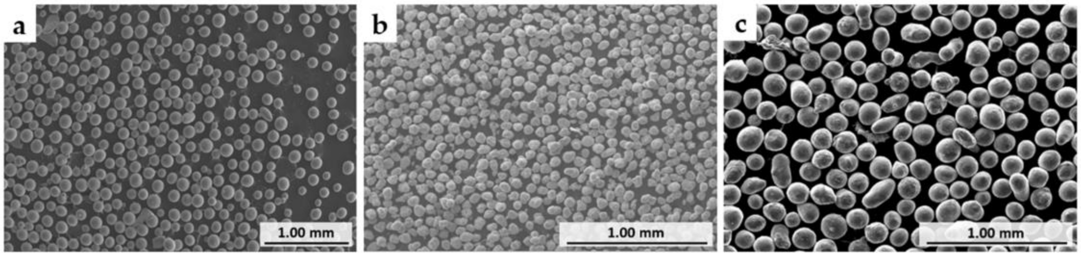

Figure 2. SEM images of elemental powders used in this work: (a) Ti; (b) Ni; (c) Cu.

2.2. DED FABRICATION

The DED fabrication process in this work was carried out by an in-house developed laser powder DED system, which consists of a continuous wave fiber laser manufactured by IPG Photonics with a wavelength of 1064 nm and a maximum power of 1 kW, a deposition platform controlled by computer numerical control (CNC) with x, y, and z movements, and a powder feeder designed by Powder Motion Labs. The diameter of the laser beam was set at 2 mm. During the deposition process, the laser power generated a melt pool on the solid materials. At the same time, the powder mixture was carried by Ar gas and delivered through a vertical powder nozzle. A TiNiCu single wall was deposited by applying the laser beam to travel back and forth with a distance of 30 mm. The laser power was set at 600 W for the first layer and 400 W for the rest of the layers; the laser travel speed was 250 mm/min. In the meantime, the powder blend was fed into the melt pool steadily and continuously. The deposition was performed in an Ar atmosphere. The average height of the entire single wall is approximately 16 mm.

2.3. MICROSTRUCTURE, ELEMENT COMPOSITION, AND PHASE

After the deposition, a thin piece of the cross-section area of the single wall was sectioned by wire electric discharge machining (EDM). The build direction (BD) is from the bottom to the top. In order to analyze the material properties at certain locations, five specific heights were marked as H1, H2, H3, H4, and H5 along the BD. The detailed information of the specific locations of the single wall cross-section is illustrated in Figure 3. H1 is a near-bottom location that is 2 mm above the bottom of the TiNiCu single wall, while H5 is a near-top location with a distance of 16 mm from the bottom. H2, H3, and H4 equally divide the cross-section from H1 to H5 into four sections. At the region of each specific height, the chemical composition and phase were studied to reveal the differences at various locations.

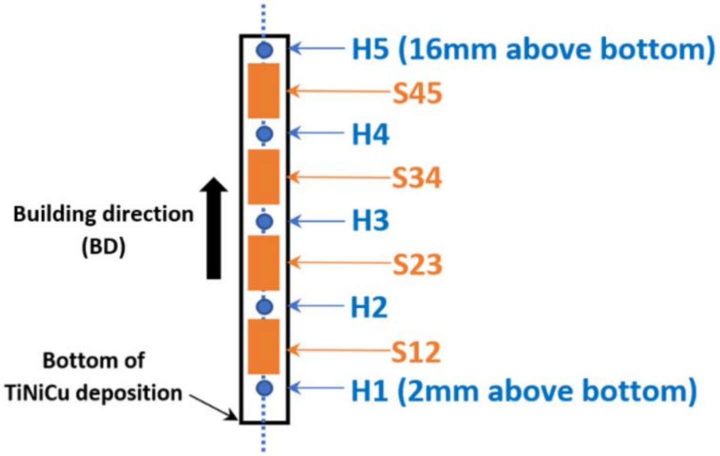

Figure 3. Schematic of the location H1, H2, H3, H4 and H5 along the BD.

The cross-section was mounted, ground, and polished using a Buehler EcoMet 250 grinder/polisher. The well-polished cross-section of the single wall was analyzed using an FEI Helios NanoLab 600 Dual-Beam SEM equipped with Oxford Energy Dispersive Spectrometer. Both large area and small area energy dispersive spectroscopy (EDS) analyses were carried out within the cross-section area of the single wall. The large area EDS analysis was conducted at all five height locations with a rough area of 1 mm2. Specific small areas were selected within various phases for the EDS spectrum analysis to determine the composition of Ti, Ni, and Cu. The X-ray diffraction (XRD) technique was used to characterize the crystal structure. All five locations were analyzed by an X'Pert X-ray diffractometer with a step size of 0.03°.

2.4. HARDNESS TEST

Vickers hardness tests were performed using a Struers Duramin 5 Vickers hardness tester equipped with a pyramidal diamond indenter. A thin slice of the TiNiCu single wall was sectioned and polished for the hardness testing. The hardness measurement was taken from 1 to 16 mm above the bottom, with an interval of 1 mm. For each measurement, the indentation load was 1.96 N, and the dwell time was set at 10 s.

2.5. TENSILE TEST

Tensile tests were applied by an Instron 5969 universal testing machine to evaluate the tensile strength of the as-deposited TiNiCu structure. The type of mini tensile sample was designed, and more details about this design can be found in the previous work [34]. The sketch is shown in Figure 4. The gauge length of this mini tensile sample design is 3 mm. Samples with the horizontal direction and vertical direction were both prepared by EDM and tested. Details of the location of sample extraction can be found in the section of results and discussions. The testing speed (strain rate) was 0.003 mm/mm/s from the start to fracture. The fracture surface was imaged by the Helios SEM, and discussion was provided based on the fractographical feature.

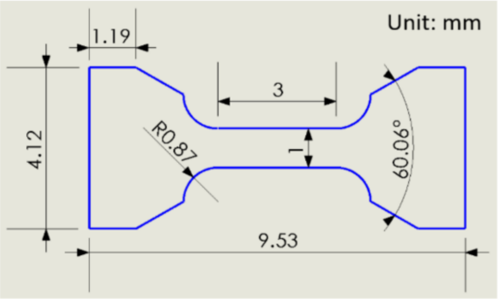

Figure 4. The mini tensile sample design.

2.6. PHASE TRANSFORMATION CHARACTERIZATION

Differential scanning calorimetry (DSC) was used to identify the phase transformation temperature of the as-deposited TiNiCu at various locations. In this work, a slice of the cross-section was divided into four sections according to the five location points. As seen in Figure 3, the four sections marked by the orange color between location points H1–H2, H2–H3, H3–H4, and H4–H5 are named S12, S23, S34, and S45, respectively. A TA Instruments Q2000 differential scanning calorimeter was utilized to run a heating and cooling cycle on each section. The range of the heating and cooling cycle was from 0 °C to 120 °C, with a constant rate of 10 °C/min.

3. RESULTS AND DISCUSSION

3.1. ELEMENT COMPOSITION AND MICROSTRUCTURE

A picture of the as-deposited TiNiCu single wall structure is displayed in Figure 5. The as-prepared cross-section of the TiNiCu deposition was analyzed by Helios SEM in both the element composition and phase distribution. At each location, large area EDS was applied for element composition study. The atomic compositions of Ti, Ni, and Cu regarding the location from H1 up to H5 are plotted in Figure 6. From Figure 6, all three elements have some variations along with BD. Ti and Cu start with a composition higher than the as-mixed composition in the powder state and decrease gradually when the location rises. In contrast, Ni begins with a lower composition and gradually increases. At higher locations, the composition of the three elements becomes much closer to the initial as-mixed composition Ti50Ni45Cu5. The element deviation at the lower height might be due to a combined effect of dilution from the Ti substrate and powder flow rate difference among different types of metal powders [35].

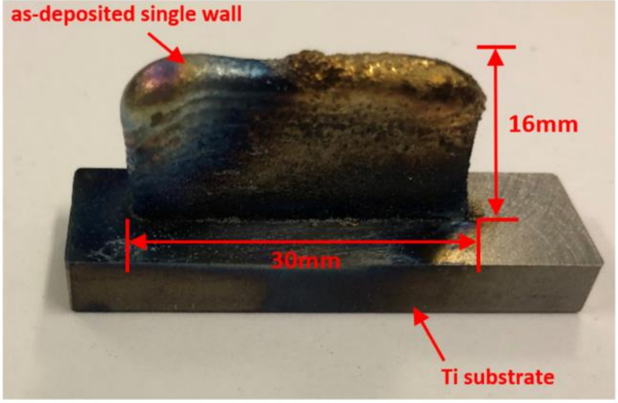

Figure 5. Image of the as-deposited TiNiCu single wall on Ti substrate.

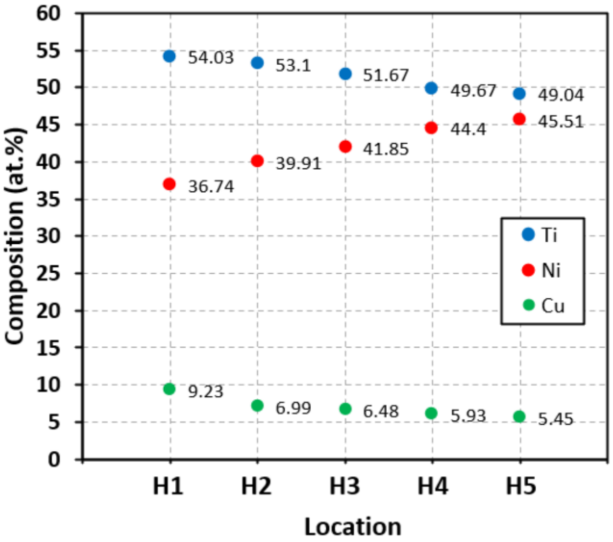

Figure 6. Ti, Ni, and Cu element composition distribution along with the height locations.

SEM images were obtained for detailed analysis in microstructure and phase composition. Figure 7 is a combination of images of all five locations. Among the ten subimages, Figure 7a,c,e,g,i are SEM images of locations H1, H2, H3, H4, and H5, respectively. Figure 7a,c,e,g,i shows the overall phase distribution, and Figure 7b,d,f,h,j shows higher magnified SEM images of a specific region within Figure 7a,c,e,g,i for small area EDS analysis on phases, respectively.

As shown in Figure 7a,c,e,g, locations H1, H2, H3, and H4 are all dominated by the light gray phase as the matrix phase and the dark gray phase as the secondary phase, which disperses within the matrix. In general, it can also be seen that the area covered by the dark gray phase decreases as the height increases. In Figure 7i, another light phase that is brighter than the matrix is also detected. In Figure 7b,d,f,h,j, ten areas within these three types of phases were picked for the EDS analysis. Areas 1, 3, 5, 7, and 9 were selected within the matrix of five height locations, while Areas 2, 4, 6, and 8 were located inside of darker secondary phases at the locations H1, H2, H3, and H4, respectively. At the height of H5, Area 10 was drawn within the brighter secondary phase. All EDS analysis results of the ten areas are listed in Table 1. In those EDS results, the relation between the atomic percentage ratio of Ti and the sum of Ni and Cu is noticed. The ratio of atomic composition Ti/(Ni + Cu) values is close to 1 in all matrices, which reveals that all five matrices are recognized as the TiNi phase with a small amount of Cu substitution. In Areas 1, 3, and 5, the matrix Ti composition exceeds 50 at.%, which is considered the Ti-rich TiNi phase, while matrix phases in Areas 7 and 9 are Ti-poor. Areas 2, 4, 6, and 8 are inside the darker secondary phase, and their Ti/(Ni + Cu) ratios are all close to 2. Then, the suggested phase will be the Ti_2Ni type intermetallic phase, which includes the Cu that replaces a low percentage of the Ni as well.

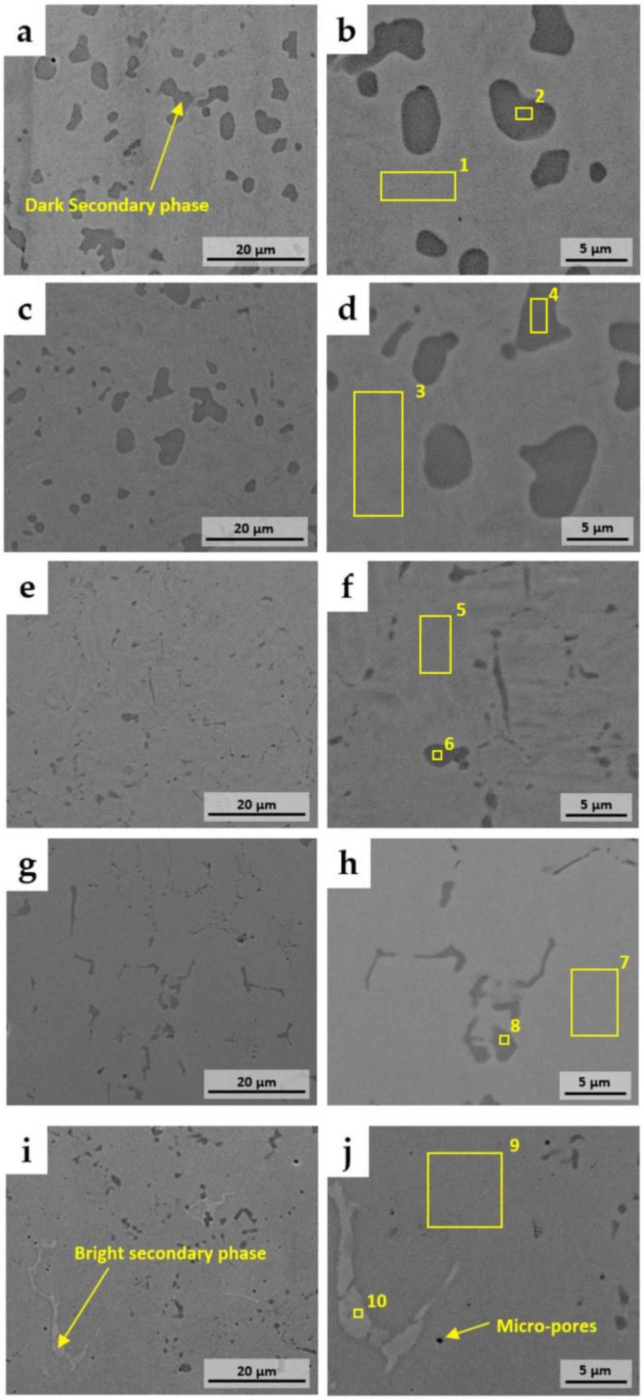

Figure 7. SEM images of the as-deposited TiNiCu single wall at various locations along the BD: (a,c,e,g,i)—Locations H1, H2, H3, H4, and H5, respectively; (b,d,f,h,j)—Locations H1, H2, H3, H4, and H5, respectively with higher magnification for EDS analysis.

Table 1. The EDS results of ten selected areas in Figure 7.

Area No. for EDS	**Ti at.%**	**Ni at.%**	**Cu at.%**
1	51.2	38.4	10.4
2	66.3	29.6	4.1
3	51.4	40.9	7.7
4	67.3	30.2	2.5
5	51.0	42.8	6.2
6	64.6	31.5	3.9
7	49.4	45.8	4.9
8	63.9	33.1	3.0
9	48.2	46.2	5.6
10	35.3	42.7	21.9

Area 10 is selected from the inner part of the brighter phase generated at the near-top location H5 of the single wall. The EDS result in Table 1 gives that Ti at.% = 35.3%, Ni at.% = 42.7%, and Cu at.% = 21.9%. According to the literature [36], the suggested phase might be $(Cu, Ni)_2Ti$, which is a type of Ti-poor secondary phase. Figure 7j also shows micro-pores that are less than 1 mm in size. The micro-pores at the upper layer could be due to the heat accumulation resulting in overheating at the upper layer.

3.2. PHASE

XRD patterns of five locations are shown in Figure 8. From the bottom to the top, four phases can be found, including the austenitic TiNi (labeled as A-phase in Figure 8), martensitic TiNi (labeled as M-phase in Figure 8), intermetallic Ti_2Ni, and Ti. The diffraction peaks of those four phases are labeled using different red markers. At the H1 location, austenitic TiNi, martensitic TiNi, and Ti give a strong signal, which is shown in Figure 8a. The existence of Ti_2Ni can also be found. The presence of the Ti crystal structure is mainly due to the dilution effect near the bottom of the single wall. In Figure 8b, the Ti peaks cannot be observed since the impact of dilution is largely reduced. The major existing phases are austenitic TiNi, martensitic TiNi, and Ti_2Ni. Figure 8c demonstrates that austenite dominates, while the signals of the martensitic TiNi and Ti_2Ni become less obvious. When they go up to locations H4 and H5, as shown in Figure 8d,e, the martensitic TiNi and Ti_2Ni can hardly be observed, and the entirety of the XRD patterns is almost dominated only by the austenite phase. For TiNi phases, the signal of the austenite phase starts from weak to strong from the bottom to the top, while the martensitic phase follows an opposite tendency. At the lower location, the as-deposited structure consists of a combination of martensite and austenite, while at the higher location, austenite becomes much more prevalent.

According to the finding in the EDS results, from the bottom to the top, the atomic composition of Ti within the matrix area varies from Ti-rich (Ti at.% > 50 at.%) to Ti-poor (Ti at.% < 50 at.%). It was mentioned in a previous research study that Ti-rich TiNi-based shape memory alloy tends to exhibit a martensitic structure at room temperature since the temperatures for phase transformation are higher [37]. The transformation temperatures will also be discussed in Section 3.5. The decrease in the martensite signal correlates with the gradual decrease in the Ti atomic composition and the constituent of Ti-rich intermetallic Ti_2Ni along with the BD, which is displayed in Figure 7. Thus, the XRD results show good consistency with the composition study found in the EDS analysis.

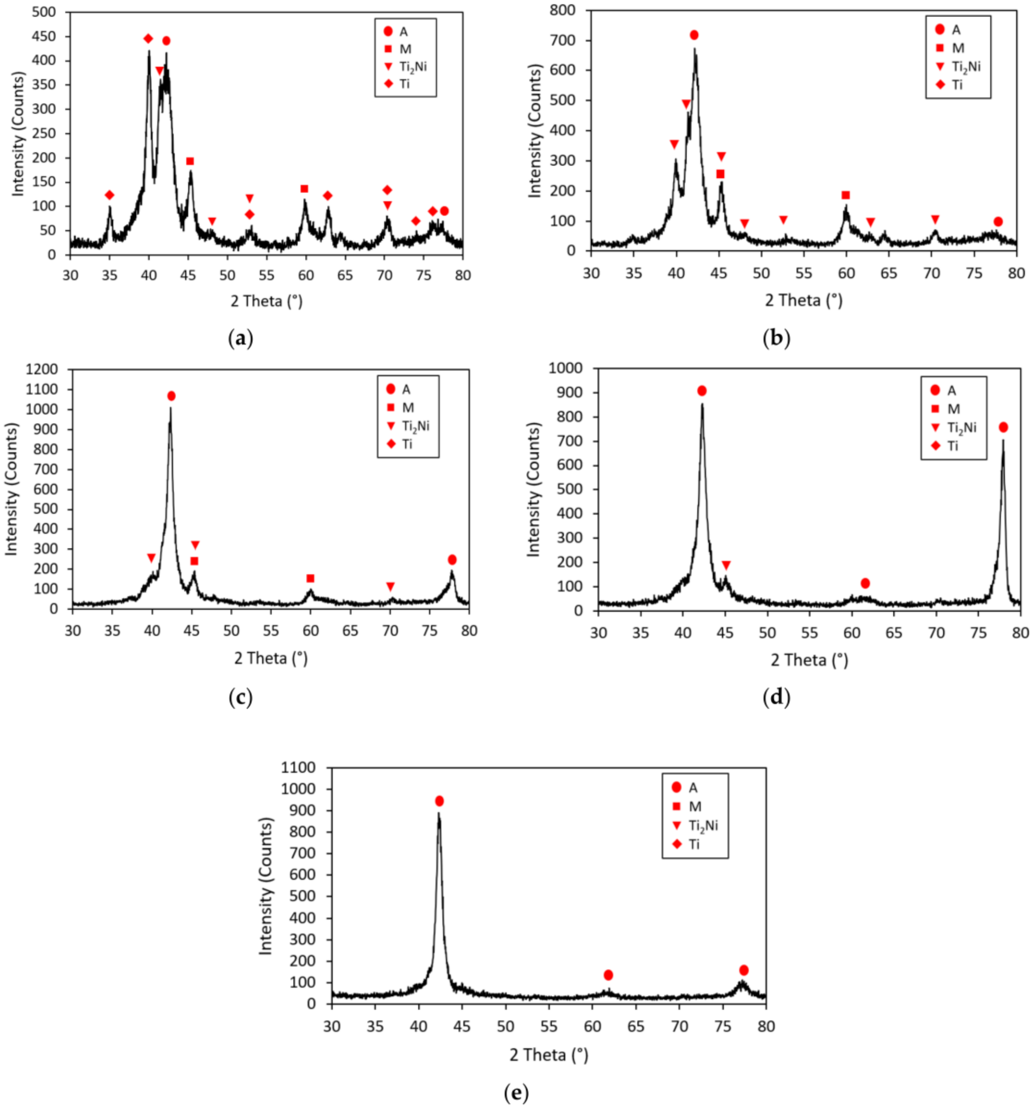

(a) (b) (c) (d) (e)

Figure 8. XRD patterns of five locations: (a) H1; (b) H2; (c) H3; (d) H4; (e) H5.

3.3. HARDNESS

The Vickers hardness values were tested along the BD across the entire deposition. The polished surface of the single wall cross-section was indented from 1 to 16 mm above the TiNiCu/Ti interfacial line (bottom line of the single wall). Hardness measurements are plotted in Figure 9. In Figure 9, the zero height is set at the TiNiCu/Ti interfacial line. It can be seen from Figure 9 that, from 1 to 10 mm, hardness values mostly fall into the range of 200~250 HV0.2, which reflects the hardness of the martensite in the lower region. There is a tendency of decline in the hardness from 1 to 10 mm within the martensite-rich region. The decline is due to the decrease in Ti_2Ni intermetallics from 1 to 10 mm. The measured hardness value becomes higher starting from 11 mm, and it increases to > 300 HV0.2, which corresponds to the hard austenite-dominated regions [29]. The increase in hardness at higher levels reflects the formation of the Ni-rich austenite phase since the matrix becomes Ti-poor at the location H4, which is 12.5 mm above the interface.

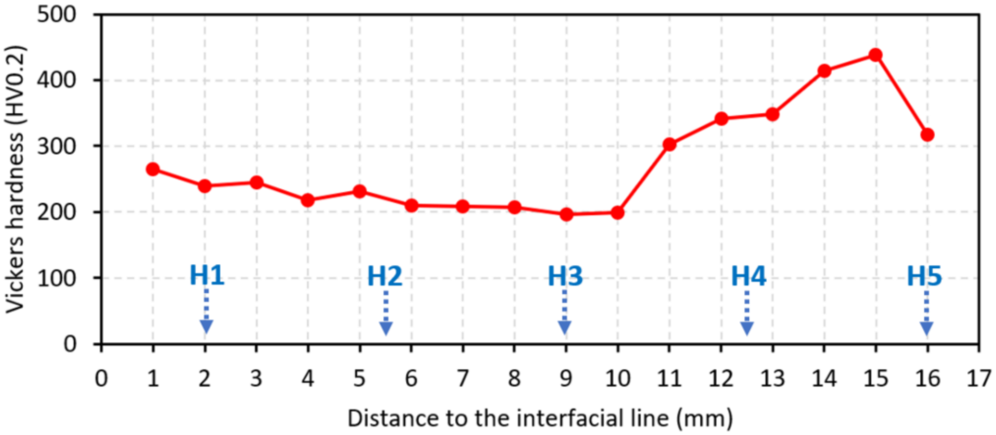

Figure 9. Vickers hardness distribution along the BD.

3.4. TENSILE TEST

Mini tensile samples were extracted along the horizontal (parallel to the substrate surface) and vertical direction (parallel to the BD). For the horizontal one, the entire sample is mainly included in the region of 8~12 mm above the interface. The vertical one spans from 13.5 to 3.5 mm above the bottom. Then, the gauge length of the vertical sample locates in the range of 7~10 mm. To avoid sample misalignment, mini tensile samples need a preload at the beginning of the test, which can also be found in previous works [38]. All tensile tests were carried out at a constant strain rate of 0.003 mm/mm/s until the sample fracture finally occurred. The stress and strain data points were collected and plotted as stress–strain curves, shown in Figure 10.

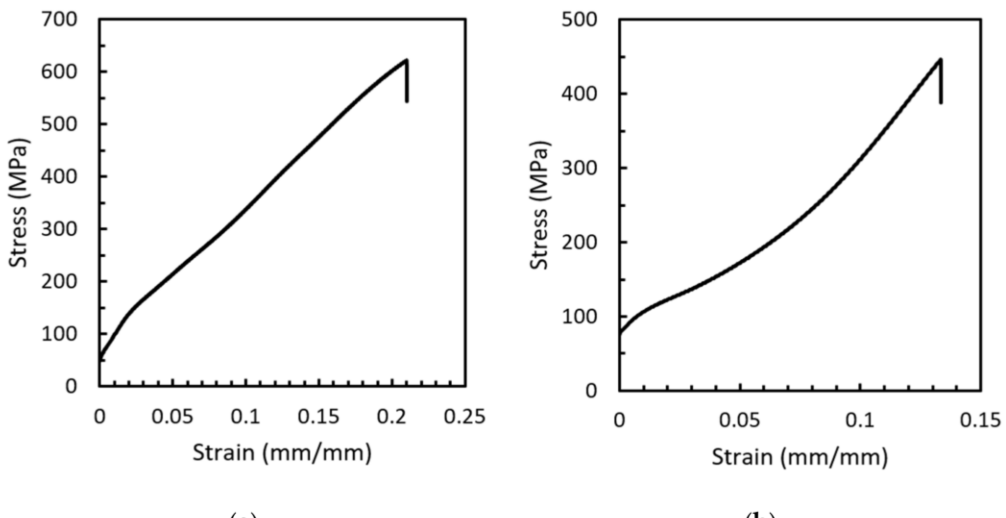

(a) (b)

Figure 10. Stress–strain curves: (a) Horizontal tensile sample; (b) vertical tensile sample.

The stress–strain curves of both horizontal and vertical samples are recorded and plotted in Figure 10, where the horizontal and vertical samples correspond to Figure 10a,b, respectively. The ultimate tensile strength (UTS) values of the horizontal sample and the vertical sample are 622 MPa and 447 MPa, respectively. The two curves are different in feature mainly due to their different compositions of martensite and austenite. The concave part of the vertical sample at the tensile strain range between 0.01 and 0.05 indicates the martensite reorienting stage [39], while the horizontal sample includes less martensite; this plateau region is not found obviously.

The SEM images of the fracture surface of the fractured samples are listed in Figure 11, where Figure 11a,b indicates the horizontal sample and Figure 11c,d represents the vertical sample. The fracture surface in Figure 11a,b,d shows the mix mode of the fracture with both dimple-like features and microcracks within the fracture surface image. The ductile feature is due to the ductile matrix, while the defects and secondary phases can cause microcracks under tensile loading and finally result in brittle fracture. Figure 11c shows brittle features. The martensite-rich vertical sample shows a lower UTS and mostly brittle fracture at the fracture surface. The strain value at the fracture point of the vertical sample is also lower than the horizontal sample. On the fracture surface of the vertical sample, more pure brittle fracture regions can be found, such as that shown in Figure 11c. The vertical sample displays more brittle features and a lower UTS result, as it includes more Ti_2Ni secondary phases along the direction of BD.

Researchers in [40,41] fabricated DEDed TiNi binary alloy parts through elemental powder blend, and the UTS values of 250 MPa and 320 MPa were obtained, respectively. The fracture shows brittle features in [40]. While in [42], TiNi was built by DED with pre-alloyed TiNi powder, and the UTS exceeds 700 MPa. Some other available reported UTS values of TiNi using selective laser melting (SLM) and wire arc additive manufacturing

(WAAM) include 601 MPa (SLM [43]), 690 ± 15 MPa (SLM [44]), and 571.4 ± 18.6 (WAAM [45]). These reported data are tabulated in Table 2 for comparison. Therefore, this work obtains a much higher UTS value among DED works using an elemental powder blend, and it is comparable with the TiNi binary alloys fabricated with AM processes other than DED. In addition, it can still be improved when comparing with DED works with pre-alloyed powders.

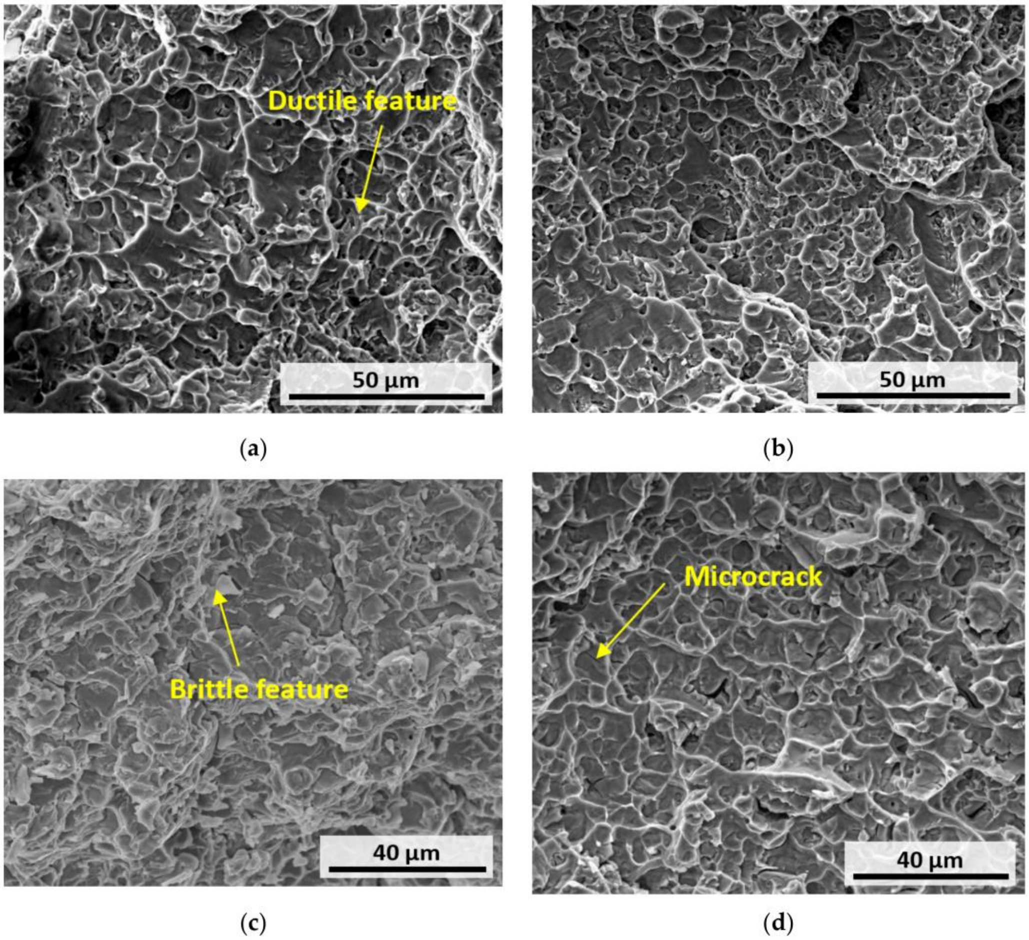

Figure 11. Fracture surface of the fractured tensile sample under SEM: (a,b) Horizontal sample; (c,d) vertical sample.

Table 2. Comparison of UTS of current work and other published AM TiNi alloys.

UTS (MPa)	**AM Processing Methods**	**Ref.**
622 for the horizontal sample 447 for the vertical sample	DED (elemental powder)	This work
250	DED (elemental powder)	[40]
320	DED (elemental powder)	[41]
780	DED (pre-alloyed)	[42]
601	SLM	[43]
690 ± 15	SLM	[44]
571.4 ± 18.6	WAAM	[45]

3.5. DSC PHASE TRANSFORMATION ANALYSIS

The DSC exothermic/endothermic graphs of four different sections are shown in Figure 12a–d. For each section, the procedure was set as a heating and cooling cycle: heating to 120 °C from 0 °C with a constant heating rate of 10 °C/min (the lower part of each graph), and then cooling back to 0 °C with a constant cooling rate of 10 °C/min (the upper part of each graph). Peaks appear during the heating and cooling process, which reflects the heat absorption or release between martensite and austenite phase transformation. From Figure 12a–c, it can be observed that sections S12, S23, and S34 have one martensite-to-austenite (M→A) peak during heating and one austenite-to-martensite (A→M) peak during cooling, while no peak can be observed between the given temperature range in S45.

The characteristic temperatures of S12, S23, and S34, including the austenite starting temperature (A_s), austenite finishing temperature (A_f), austenite peak temperature (A_p), martensite starting temperature (M_s), martensite finishing temperature (M_f), and martensite peak temperature (M_p) are determined from DSC graphs in Figure 12a–c. All of the phase starting and finishing temperature points were determined by the tangent method. These characteristic temperatures are all labeled in each DSC graph.

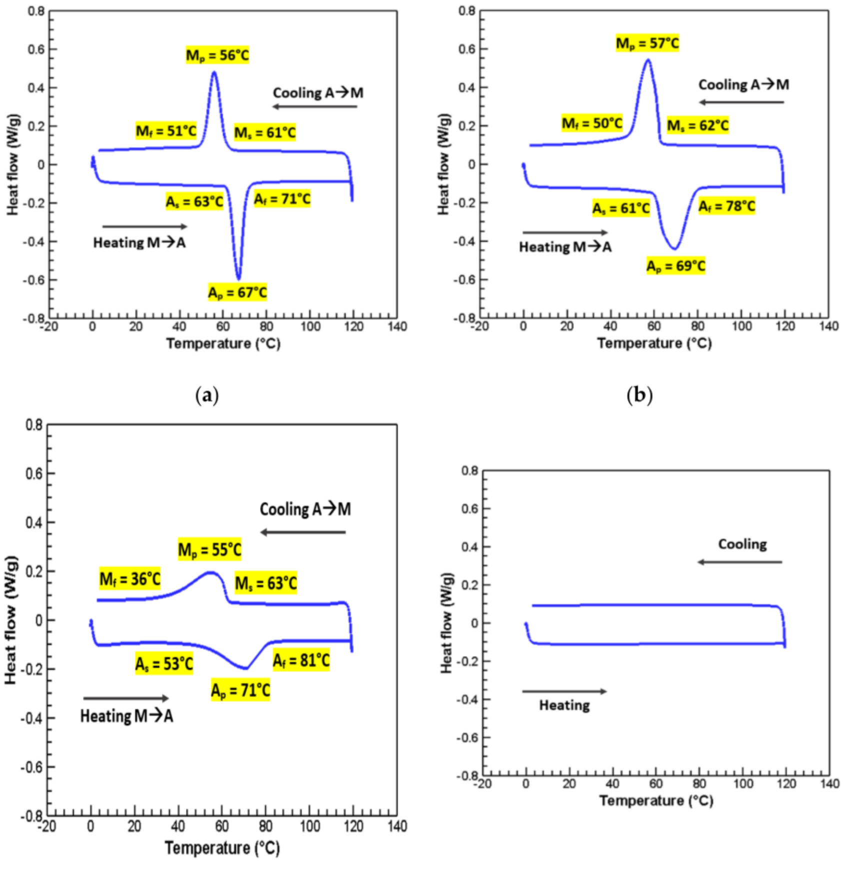

(a) (b)

(c) (d)

Figure 12. DSC heat flow–temperature curves of TiNiCu at four sections: (a) Section S12; (b) Section S23; (c) Section S34; (d) Section S45.

From Figure 12a–c, it can be found that S12, S23, and S34 experience transformation during the heating and cooling temperature. In contrast, no transformation can be found in S45 in the given temperature range. This indicates that S12, S23, and S34 include the martensite TiNi phase before heating, while almost no martensite exists in S45. S12, S23, and S34 exhibit some portion of the martensite phase at room temperature (~25 °C) since their values of M_f and A_s are all higher than room temperature. For S45, it can be inferred that the martensite transformation may occur at a low temperature that is lower than 0 °C. Therefore, at room temperature, S45 consists of almost all austenite. This agrees well with what is found in the aforementioned XRD results. In XRD results, no strong diffraction pattern of the martensite phase can be detected in locations H4 and H5. From Figure 12a–c, peak widths of M→A: $|A_f-A_s|$, and A→M: $|M_s-M_f|$ can also be determined. The relation of peak widths among S12, S23, and S34 is S12 < S23 < S34. The temperature range for the phase transformation becomes longer when the location gets higher, which shows that the homogeneity of martensite is the highest at location H1, and it follows a descending trend when going up along the BD direction [42].

Adding Cu to replace a certain atomic number of Ni was reported to be able to reduce the thermal hysteresis, which is usually defined by the difference between A_p and M_p [46], or the difference between A_f and M_s [47]. In this work, the thermal hysteresis calculated by $|A_p-M_p|$ of these three sections can be found for S12 (11 °C), S23 (12 °C), and S34 (16 °C). Peak widths and hysteresis of S12, S23, and S34 in this work are summarized in Table 3. Several previously reported thermal hysteresis values of TiNiCu alloys and additively manufactured TiNi alloys have been collected and listed together with S12, S23, and S34 in Table 4 for comparison.

Table 3. Peak width and hysteresis of Sections S12, S23, and S34.

Section	$\lvert M_s - M_f \rvert$ (°C)	$\lvert A_f - A_s \rvert$ (°C)	$\lvert A_p - M_p \rvert$ (Hysteresis) (°C)
S12	10	8	11
S23	12	17	12
S34	27	28	16

Table 4. Comparison of thermal hysteresis of TiNiCu and TiNi.

Material Type	Processing	Hysteresis (°C)	Ref.
TiNiCu	DED	11~16	This work
	Plasma skull push–pull	21.1	[30]
	Vacuum arc melting	23.8~30.6	[46]
	Ingot metallurgy	5~19	[47]
	Magnetron sputtering	9	[49]
TiNi	DED	35.3~45.9	[50]
	SLM	30	[51]
	SLM	28	[44]
	Powder metallurgy	30~36	[52]

The thermal hysteresis of TiNi is mostly within the range of 25~40 °C [48], as seen from the TiNi binary alloys listed in Table 4 by both AM and non-AM methods. Table 4 indicates that most reported hysteresis values of TiNiCu ternary shape memory alloys by various non-AM techniques are below 25 °C. There is very little reported hysteresis of TiNiCu by AM so far, and in this work, the TiNiCu fabricated by elemental powder-based DED reaches a much more narrow range of 11~16 °C.

4. CONCLUSIONS

In this work, a TiNiCu ternary shape memory alloy single-wall structure was fabricated by the DED process through an elemental powder mixture. As AM is a layer-based manufacturing technique and the elemental powder mixture is a novel concept in AM, the single-wall structure was equally separated into five location points along the BD to perform comprehensive material characterization on the chemical composition, phase, mechanical properties, and functional properties with regard to various locations of interest. The main conclusions are summarized below:

For the overall element composition along the BD, at the upper locations, the compositions of the three elements are much closer to the as-mixed composition. The small area EDS analysis results show that all matrix phases are TiNi phases, where a small portion of Ni atoms are replaced by Cu. At the lower locations, the main secondary phase is Ti_2Ni. The Ti_2Ni composition decreases when the location goes up due to the decrease in the Ti element composition. At the top of the as-deposited single-wall structure, a small amount of the Ni-rich secondary phase exists where the Ti composition decreases to slightly below 50 at.%.

The XRD patterns indicate the increase in austenite TiNi and the decrease in martensite TiNi from the bottom to the top, which is related to the changing of the compositions of Ti and (Ni + Cu). The variations in the martensitic TiNi and austenitic TiNi compositions agree well with the atomic compositions of Ti and (Ni + Cu). The average Vickers hardness at the martensite-rich area (200~250 HV0.2) is lower than the austenite-rich area (300~450 HV0.2), which also matches the XRD results well.

The UTS of the as-deposited TiNiCu tensile sample reaches 622 MPa along the horizontal direction in the area with less of the martensite phase. The vertical sample that includes martensite-rich areas within the gauge length gets a UTS of 447 MPa, and the strain at the fracture is also lower than the horizontal sample. The UTS values of both are comparable with other AM-based TiNi binary alloys.

Strong martensite–austenite transformation signals are witnessed from the DSC results in sections S12, S23, and S34 within the 0~120 °C temperature range, which reflects a good phase transformation response at room temperature. The three sections' thermal hysteresis values are much smaller than AM-based TiNi binary alloys. These results agree well with reducing thermal hysteresis by adding Cu in the Ti–Ni binary system.

FUNDING

This research was funded by NSF, grant number CMMI 1625736.

ACKNOWLEDGMENTS

The authors greatly acknowledge the research supports from the Intelligent Systems Center (ISC), Material Research Center (MRC), and Department of Chemistry Shared

Instrument Lab at Missouri S&T for the help in sample preparation and material characterization.

REFERENCES

1. Taheri, H.; Koester, L.W.; Bigelow, T.A.; Faierson, E.J.; Bond, L.J. In situ additive manufacturing process monitoring with an acoustic technique: clustering performance evaluation using K-means algorithm. J. Manuf. Sci. Eng. 2019, 141, 041011.

2. F42 Committee. Standard Guide for Directed Energy Deposition of Metals; ASTM International: West Conshohocken, PA, USA, 2016.

3. Wang, Z.; Palmer, T.A.; Beese, A.M. Effect of processing parameters on microstructure and tensile properties of austenitic stainless steel 304L made by directed energy deposition additive manufacturing. Acta Mater. 2016, 110, 226–235.

4. Tan, Z.E.; Pang, J.H.L.; Kaminski, J.; Pepin, H. Characterisation of porosity, density, and microstructure of directed energy deposited stainless steel AISI 316L. Addit. Manuf. 2019, 25, 286–296.

5. Bai, Y.; Chaudhari, A.; Wang, H. Investigation on the microstructure and machinability of ASTM A131 steel manufactured by directed energy deposition. J. Mater. Process. Technol. 2020, 276, 116410.

6. Sui, S.; Chen, J.; Li, Z.; Li, H.; Zhao, X.; Tan, H. Investigation of dissolution behavior of laves phase in inconel 718 fabricated by laser directed energy deposition. Addit. Manuf. 2020, 32, 101055.

7. Hu, Y.; Lin, X.; Li, Y.; Zhang, S.; Gao, X.; Liu, F.; Huang, W. Plastic deformation behavior and dynamic recrystallization of Inconel 625 superalloy fabricated by directed energy deposition. Mater. Des. 2020, 186, 108359.

8. Kistler, N.A.; Nassar, A.R.; Reutzel, E.W.; Corbin, D.J.; Beese, A.M. Effect of directed energy deposition processing parameters on laser deposited Inconel®718: Microstructure, fusion zone morphology, and hardness. J. Laser Appl. 2017, 29, 022005.

9. Wolff, S.; Lee, T.; Faierson, E.; Ehmann, K.; Cao, J. Anisotropic properties of directed energy deposition (DED)-processed Ti–6Al–4V. J. Manuf. Process. 2016, 24, 397–405.

10. Keist, J.S.; Palmer, T.A. Role of geometry on properties of additively manufactured Ti-6Al-4V structures fabricated using laser based directed energy deposition. Mater. Des. 2016, 106, 482–494.

11. Kistler, N.A.; Corbin, D.J.; Nassar, A.R.; Reutzel, E.W.; Beese, A.M. Effect of processing conditions on the microstructure, porosity, and mechanical properties of Ti-6Al-4V repair fabricated by directed energy deposition. J. Mater. Process. Technol. 2019, 264, 172–181.

12. Javidani, M.; Arreguin-Zavala, J.; Danovitch, J.; Tian, Y.; Brochu, M. Additive Manufacturing of AlSi10Mg Alloy Using Direct Energy Deposition: Microstructure and Hardness Characterization. J. Therm. Spray Technol. 2017, 26, 587–597.

13. Svetlizky, D.; Zheng, B.; Buta, T.; Zhou, Y.; Golan, O.; Breiman, U.; Haj-Ali, R.; Schoenung, J.M.; Lavernia, E.J.; Eliaz, N. Directed energy deposition of Al 5xxx alloy using Laser Engineered Net Shaping (LENS®). Mater. Des. 2020, 192, 108763.

14. Clayton, R.M. The Use of Elemental Powder Mixes in Laser-Based Additive Manufacturing. Master’s Thesis, Missouri University of Science and Technology, Missouri, MO, USA, 2013.

15. Mahamood, R.M.; Akinlabi, E.T.; Shukla, M.; Pityana, S.L. Characterization of laser deposited Ti6Al4V/TiC composite powders on a Ti6Al4V substrate. Lasers Eng. 2014, 29, 197–213.

16. Shen, M.-Y.; Tian, X.-J.; Liu, D.; Tang, H.-B.; Cheng, X. Microstructure and fracture behavior of TiC particles reinforced Inconel 625 composites prepared by laser additive manufacturing. J. Alloys Compd. 2018, 734, 188–195.

17. Farayibi, P.K.; Folkes, J.; Clare, A.; Oyelola, O. Cladding of pre-blended Ti–6Al–4V and WC powder for wear resistant applications. Surf. Coat. Technol. 2011, 206, 372–377.

18. Li, N.; Xiong, Y.; Xiong, H.; Shi, G.; Blackburn, J.; Liu, W.; Qin, R. Microstructure, formation mechanism and property characterization of Ti + SiC laser cladded coatings on Ti6Al4V alloy. Mater. Charact. 2019, 148, 43–51.

19. Chaudhary, V.; Yadav, N.M.S.K.K.; Mantri, S.A.; Dasari, S.; Jagetia, A.; Ramanujan, R.V.; Banerjee, R. Additive manufacturing of functionally graded Co–Fe and Ni–Fe magnetic materials. J. Alloys Compd. 2020, 823, 153817.

20. Karnati, S.; Zhang, Y.; Liou, F.F.; Newkirk, J.W. On the Feasibility of Tailoring Copper–Nickel Functionally Graded Materials Fabricated through Laser Metal Deposition. Metals 2019, 9, 287.

21. Collins, P.C.; Banerjee, R.; Banerjee, S.; Fraser, H.L. Laser deposition of compositionally graded titanium–vanadium and titanium–molybdenum alloys. Mater. Sci. Eng. 2003, 352, 118–128.

22. Chao, Q.; Guo, T.; Jarvis, T.; Wu, X.; Hodgson, P.; Fabijanic, D. Direct laser deposition cladding of AlxCoCrFeNi high entropy alloys on a high-temperature stainless steel. Surf. Coat. Technol. 2017, 332, 440–451.

23. Dobbelstein, H.; Gurevich, E.L.; George, E.P.; Ostendorf, A.; Laplanche, G. Laser metal deposition of a refractory TiZrNbHfTa high-entropy alloy. Addit. Manuf. 2018, 24, 386–390.

24. Gwalani, B.; Soni, V.; Waseem, O.A.; Mantri, S.A.; Banerjee, R. Laser additive manufacturing of compositionally graded AlCrFeMoVx (x = 0 to 1) high-entropy alloy system. Opt. Laser Technol. 2019, 113, 330–337.

25. Jani, J.M.; Leary, M.; Subic, A.; Gibson, M.A. A review of shape memory alloy research, applications and opportunities. Mater. Des. 2014, 56, 1078–1113.

26. Wen, C.; Yu, X.; Zeng, W.; Zhao, S.; Wang, L.; Wan, G.; Huang, S.; Grover, H.; Chen, Z. Mechanical behaviors and biomedical applications of shape memory materials: A review. AIMS Mater. Sci. 2018, 5, 559–590.

27. Halani, P.R.; Shin, Y.C. In Situ Synthesis and Characterization of Shape Memory Alloy Nitinol by Laser Direct Deposition. Met. Mater. Trans. A 2012, 43, 650–657.

28. Baran, A.; Polanski, M. Microstructure and properties of LENS (laser engineered net shaping) manufactured Ni-Ti shape memory alloy. J. Alloys Compd. 2018, 750, 863–870.

29. Marattukalam, J.J.; Singh, A.K.; Datta, S.; Das, M.; Balla, V.K.; Bontha, S.; Kalpathy, S.K. Microstructure and corrosion behavior of laser processed NiTi alloy. Mater. Sci. Eng. C 2015, 57, 309–313.

30. De Araújo, C.J.; Da Silva, N.J.; Da Silva, M.M.; Gonzalez, C.H. A comparative study of Ni–Ti and Ni–Ti–Cu shape memory alloy processed by plasma melting and injection molding. Mater. Des. 2011, 32, 4925–4930.

31. Chen, Y.; Zhang, X.; Parvez, M.M.; Liou, F. A Review on Metallic Alloys Fabrication Using Elemental Powder Blends by Laser Powder Directed Energy Deposition Process. Materials 2020, 13, 3562.

32. Shiva, S.; Palani, I.; Paul, C.; Mishra, S.; Singh, B. Investigations on phase transformation and mechanical characteristics of laser additive manufactured TiNiCu shape memory alloy structures. J. Mater. Process. Technol. 2016, 238, 142–151.

33. Carroll, B.E.; Palmer, T.A.; Beese, A.M. Anisotropic tensile behavior of Ti–6Al–4V components fabricated with directed energy deposition additive manufacturing. Acta Mater. 2015, 87, 309–320.

34. Karnati, S.; Hoerchler, J.L.; Liou, F.; Newkirk, J.W. Influence of gage length on miniature tensile characterization of powder bed fabricated 304L stainless steel. In Proceedings of the 28th Solid Freeform Fabrication Symposium, Austin, TX, USA, 7–9 August 2017; pp. 7–9.

35. Chen, X. Fabrication and Characterization of Advanced Materials Using Laser Metal Deposition from Elemental Powder Mixture. Ph.D. Thesis, Missouri University of Science and Technology, Missouri, MO, USA, 2018.

36. Zhu, W.J.; Duarte, L.I.; Leinenbach, C. Experimental study and thermodynamic assessment of the Cu–Ni–Ti system. Calphad 2014, 47, 9–22.

37. Tadayyon, G.; Mazinani, M.; Guo, Y.; Zebarjad, S.M.; Tofail, S.A.; Biggs, M.J. Study of the microstructure evolution of heat treated Ti-rich NiTi shape memory alloy. Mater. Charact. 2016, 112, 11–19.

38. Zhang, X.; Chen, Y.; Liou, F. Fabrication of SS316L-IN625 functionally graded materials by powder-fed directed energy deposition. Sci. Technol. Weld. Join. 2019, 24, 504–516.

39. Zupanc, J.; Vahdat-Pajouh, N.; Schäfer, E. New thermomechanically treated NiTi alloys–a review. Int. Endod. J. 2018, 51, 1088–1103.

40. Wang, C.; Tan, X.; Du, Z.; Chandra, S.; Sun, Z.; Lim, C.; Tor, S.B.; Wong, C. Additive manufacturing of NiTi shape memory alloys using pre-mixed powders. J. Mater. Process. Technol. 2019, 271, 152–161.

41. Shiva, S.; Palani, I.; Mishra, S.; Paul, C.; Kukreja, L. Investigations on the influence of composition in the development of Ni–Ti shape memory alloy using laser based additive manufacturing. Opt. Laser Technol. 2015, 69, 44–51.

42. Kumar, S.; Marandi, L.; Balla, V.K.; Bysakh, S.; Piorunek, D.; Eggeler, G.; Das, M.; Sen, I. Microstructure–Property correlations for additively manufactured NiTi based shape memory alloys. Materialia 2019, 8, 100456.

43. Moghaddam, N.S.; Saghaian, S.E.; Amerinatanzi, A.; Ibrahim, H.; Li, P.; Toker, G.P.; Karaca, H.E.; Elahinia, M. Anisotropic tensile and actuation properties of NiTi fabricated with selective laser melting. Mater. Sci. Eng. A 2018, 724, 220–230.

44. Zhang, Q.; Hao, S.; Liu, Y.; Xiong, Z.; Guo, W.; Yang, Y.; Ren, Y.; Cui, L.; Ren, L.; Zhang, Z. The microstructure of a selective laser melting (SLM)-fabricated NiTi shape memory alloy with superior tensile property and shape memory recoverability. Appl. Mater. Today 2020, 19, 100547.

45. Zeng, Z.; Cong, B.; Oliveira, J.; Ke, W.; Schell, N.; Peng, B.; Qi, Z.; Ge, F.; Zhang, W.; Ao, S. Wire and arc additive manufacturing of a Ni-rich NiTi shape memory alloy: Microstructure and mechanical properties. Addit. Manuf. 2020, 32, 101051.

46. Phukaoluan, A.; Khantachawana, A.; Kaewtathip, P.; Dechkunakorn, S.; Anuwongnukroh, N.; Santiwong, P.; Kajornchaiyakul, J. Property Improvement of TiNi by Cu Addition for Orthodontics Applications. Appl. Mech. Mater. 2011, 87, 95–100.

47. Sampath, V.; Srinithi, R.; Santosh, S.; Sarangi, P.P.; Fathima, J.S. The Effect of Quenching Methods on Transformation Characteristics and Microstructure of an NiTiCu Shape Memory Alloy. Trans. Indian Inst. Met. 2020, 73, 1481–1488.

48. Elahinia, M.H.; Hashemi, M.; Tabesh, M.; Bhaduri, S.B. Manufacturing and processing of NiTi implants: A review. Prog. Mater. Sci. 2012, 57, 911–946.

49. Zhang, H.J.; Qiu, C.J. A TiNiCu Thin Film Micropump Made by Magnetron Co-Sputtered Method. Mater. Trans. 2006, 47, 532–535.

50. Krishna, B.V.; Bose, S.; Bandyopadhyay, A. Laser Processing of Net-Shape NiTi Shape Memory Alloy. Met. Mater. Trans. A 2007, 38, 1096–1103.

51. Zhang, B.; Chen, J.; Coddet, C. Microstructure and Transformation Behavior of in-situ Shape Memory Alloys by Selective Laser Melting Ti–Ni Mixed Powder. J. Mater. Sci. Technol. 2013, 29, 863–867.

52. Elsayed, A.; Umeda, J.; Kondoh, K. Effect of quenching media on the properties of TiNi shape memory alloys fabricated by powder metallurgy. J. Alloys Compd. 2020, 842, 155931.

III. TINI-BASED BI-METALLIC SHAPE-MEMORY ALLOY BY LASER-DIRECTED ENERGY DEPOSITION

ABSTRACT

In this study, laser-directed energy deposition was applied to build a Ti-rich ternary Ti–Ni–Cu shape-memory alloy onto a TiNi shape-memory alloy substrate to realize the joining of the multifunctional bi-metallic shape-memory alloy structure. The cost-effective Ti, Ni, and Cu elemental powder blend was used for raw materials. Various material characterization approaches were applied to reveal different material properties in two sections. The as-fabricated Ti–Ni–Cu alloy microstructure has the TiNi phase as the matrix with Ti_2Ni secondary precipitates. The hardness shows no high values indicating that the major phase is not hard intermetallics. A bonding strength of 569.1 MPa was obtained by tensile testing, and digital image correlation reveals the different tensile responses of the two sections. Differential scanning calorimetry was used to measure the phase-transformation temperatures. The austenite finishing temperature of higher than 80 °C was measured for the Ti–Ni–Cu alloy section. For the TiNi substrate, the austenite finishing temperature was tested to be near 47 °C at the bottom and around 22 °C at the upper substrate region, which is due to the repeated laser scanning that acts as annealing on the substrate. Finally, the multiple shape-memory effect of two shape-memory alloy sides was tested and identified.

1. INTRODUCTION

Joining different metal alloys into a single bi-metallic component can realize a wide variety of combinations with excellent material properties [1,2,3], and the joining of bi-metals is necessary in many industrial environments where different properties are needed at different locations [3]. The directed energy deposition (DED) additive manufacturing (AM) process has become an important approach to realize various types of metal joining and metal repair since strong metallurgical bonding can be achieved [4,5,6]. So far, DED has been used in various applications including metal joining and part repairing [2,6,7,8]. Also, since the AM process has a high degree of freedom for the spatial distribution of both geometry and material compositions, it can be much more flexible in developing more novel alloy structures [9,10]. Typical works using DED to join similar or dissimilar alloys include steels, Ti alloys, Ni-based superalloys, and Cu alloys. Sahasrabudhe et al. [2] joined SS410 with Ti-6Al-4V to obtain a high application temperature at the Ti-alloy end and the economic corrosion-resistive steel end. Jones et al. [11] applied DED for the manufacturing of steel-Inconel bi-metallic structures. Zhang et al. [12] used DED to join steels and Cu in order to obtain both high strengths from steel and high thermal conductivity from Cu. Functionally graded structures and interlayers can also be used for joining two dissimilar alloy parts by DED, which benefits from the flexible nature of the additive process [13,14,15].

Shape-memory alloy (SMA) is a type of smart metallic material that is able to demonstrate different shapes at different temperatures and memorize its original shape through austenite-martensite phase transformation [16,17]. TiNi alloy is a popular metallic material that can demonstrate shape-memory effects [17,18,19]. For TiNi alloys, it has been found that their phase-transformation temperature (TT) can be changed by adjusting the chemical composition and processing methods [17,20]. Therefore, the TTs of TiNi alloy can cover a wide temperature range for multiple functions [20]. Also, if different types of TiNi SMAs can coexist in a single component, it will obtain more unique and attractive multiple shape-memory behaviors. For example, Khan et al. [21] flexibly applied a laser to TiNi alloys to generate a discrepancy between laser-affected areas and created location-dependent TTs within a single part. Nematollahi et al. [22] applied selective laser melting (SLM), a powder-bed-based AM process, to build a graded TiNi SMA by changing the processing parameters at two different sections. For DED, by taking advantage of the flexible capability in similar or dissimilar joining, SMAs with multiple shape-memory behaviors can also be combined using DED to demonstrate more functions. Most of the aforementioned DED processes used for metal joining focused on improving the comprehensive mechanical, structural, and thermal properties. However, the joining effect and shape-memory behavior after joining two different types of TiNi-based SMAs using DED have not been widely reported.

For DED, both the feedstock SMA materials and the substrate SMA materials can have a wide range of selections. In this paper, we applied the DED approach to join two different TiNi-based parts into a bi-metallic SMA in order to exhibit multiple shape-memory behaviors. A Ti-rich ternary Ti–Ni–Cu SMA was deposited on a near equiatomic binary TiNi alloy to realize the bi-metallic SMAs, which were joined by two SMA parts with different element types, element compositions, and processing methods. A small amount of a third element can be applied to create more applications [23], such as by adding

Cu to replace a small portion of Ni, Ti–Ni–Cu SMA can obtain narrower hysteresis and potential applications in the biomedical field [24,25]. The Ti–Ni–Cu ternary SMA was fabricated by the powder mixture of Ti, Ni, and Cu elemental powders. The elemental powder mixture was used as an alternative form of raw materials other than pre-alloyed powders [26,27]. The SMA with an as-mixed atomic composition of Ti–45at.%Ni–5at.%Cu was fabricated by elemental powders in [28,29] with titanium as the substrate material. In this work, more details will be studied on using elemental powder DED to build Ti–Ni–Cu/TiNi bi-metallic alloys. The joining effect at the interface, the bonding strength, and the multiple functional behaviors from different sections of SMA will all be evaluated.

2. MATERIALS AND METHODS

In this work, a Ti-rich Ti–Ni–Cu alloy single-wall structure was deposited on a TiNi substrate by a DED processing system mainly including a laser system, a CNC-controlled moving stage, and a powder feeder. Near spherical Cp-Ti powder (AP&C, particle size 53~150 μm), Ni powder (Atlantic Equipment Engineers Inc., Upper Saddle River, NJ, USA, particle size −100/+325 mesh), and Cu powder (Royal Metal Powders Inc., Maryville, TN, USA, average particle size 110 μm [12]) were mixed with the atomic composition of Ti/Ni/Cu = 53/44/3 to create a Ti-rich composition that is different from the TiNi substrate. We use Ti–Ni–Cu alloy to represent this Ti–44at.%Ni–3at.%Cu ternary SMA that was deposited and studied in this paper. The powder blend was homogenized using a Turbula T2F mixer for 0.5 hr. The substrate material is near-equiatomic TiNi binary

SMA bar material purchased from Kellogg’s Research Labs (New Boston, NH, USA), which was cut to size, 25 mm × 10 mm × 5 mm. The Ti–Ni–Cu alloy single-wall deposition strategy on the TiNi substrate is illustrated in Figure 1a. The substrate was fixed by a vise on the moving stage, and the single wall structure was deposited on the surface of 25 mm × 5 mm of the substrate. An IPG Photonics CW fiber laser with a 1064 nm wavelength was used in this work to create a melt pool on the substrate. The spot size was adjusted and fixed at approximately 2.5 mm. A powder nozzle was used to feed powders into the melt pool and the nozzle was 10 mm above the substrate surface. The moving stage followed a single track and multilayer toolpath. The toolpath consists of uniform +Y direction and −Y direction movements with no dwell time for multiple cycles. Between each change in the Y direction, the stage dropped down vertically by one increment, which represents the layer thickness. The travel speed for the stage in the +Y and −Y directions was 250 mm/min. During the traveling guided by the toolpath, the Ti, Ni, and Cu powder mixture was delivered into the melt pool through the powder nozzle by the powder feeder supplied by Powder Motion Labs. Solid layers build up along the Z direction as seen in Figure 1a,b, which is called the building direction (BD). The laser power was set at 600 W at the first layer and 400 W for all the remaining layers. A total of 60 layers were deposited, and the dimension of the DED Ti–Ni–Cu alloy along the Y direction (long direction) is 25 mm, whereas the total deposition height of the Ti–Ni–Cu alloy is 10 mm. The entire process was carried out within an argon atmosphere to minimize the oxidation effect.

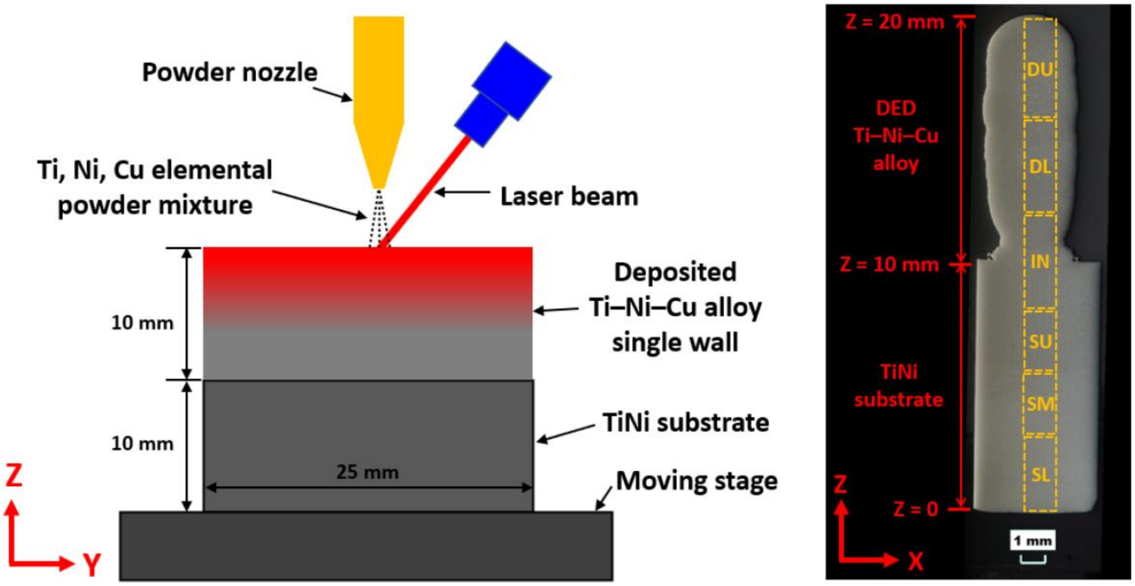

(a) (b)

Figure 1. (a) The schematic of joining bi-metallic SMA using DED in this work. (b) Image of the XZ-plane cross-section of the bi-metallic structure including the TiNi substrate and the DED Ti–Ni–Cu alloy. The bottom line of the substrate has been marked as Z = 0. The Z height of the interface and the top point are 10 mm and 20 mm, respectively.

The cross-section of the 10 mm tall Ti–Ni–Cu alloy single wall joined with the 10 mm tall TiNi substrate was cut off by wire-EDM and was prepared for material characterization, including microstructural, functional, and mechanical testing and joining evaluation. A sample from the cross-section along the XZ-plane of the bi-metallic structure was prepared by following the metallographic specimen preparation steps using a Buehler EcoMet 250 grinder-polisher in order to observe the microstructure through microscopes. The sample was mounted by epoxy and ground using SiC sandpapers from 320 grit to 1200 grit. After grinding, the sample was then polished by 9 µm, 6 µm, 3 µm, 1 µm diamond suspension, and 0.05 µm colloidal alumina. After polishing, the sample was etched using Kroll’s reagent (2 mL HF, 6 mL HNO3, and 92 mL distilled water) by swabbing the surface for 30 s. Optical microscopic imaging was done on the sample by a Hirox KH-8700 optical microscope (OM) (Hirox Co., Ltd., Tokyo, Japan). High-resolution electron microscopic imaging and energy-dispersive spectroscopy (EDS) analysis were performed by a Thermo Fisher Scientific Helios Hydra CX scanning electron microscope (SEM) (Thermo Fisher Scientific, Waltham, MA, USA) and a Helios NanoLab 600 SEM (Thermo Fisher Scientific, Waltham, MA, USA).

Figure 1b is an OM image of the well-polished cross-section of the bi-metallic SMA structure. To determine the locations, the bottom point of the TiNi substrate is marked as Z = 0. Correspondingly, the interfacial line and the top point of the DED Ti–Ni–Cu alloy single wall are marked as Z = 10 mm and Z = 20 mm, respectively. Vickers hardness values of both the DED Ti–Ni–Cu alloy part and the TiNi substrate were measured by a Struers Duramin-5 Vickers hardness tester. According to the Z coordinate shown in Figure 1b, Vickers hardness testing was conducted at a height from Z = 1 mm to Z = 19 mm with a 1 mm interval. For each height, three indentations were taken, and the average hardness of each height was calculated. Each indentation used a load of 1.96 N and a dwell time of 10 s.

The bonding strength between the Ti–Ni–Cu alloy part and the TiNi substrate was measured by uniaxial tensile testing via an Instron 5969 universal testing machine (Instron, Norwood, MA, USA) and analyzed by the digital image correlation (DIC) technique. Figure 2a shows the sketch of the miniature tensile specimen that was developed to study mechanical behaviors of small size materials. The gauge length of the specimen is 3 mm, and the thickness is 1 mm. More information can be found in a previous study [30]. A 10 kN load cell was applied for the testing of the miniature tensile specimen. The crosshead speed was controlled to maintain the strain rate at 0.003 mm/mm/s during the tensile test. Figure 2b displays the camera setup for DIC during the tensile testing. The following fracture surface analysis was also conducted using the Helios Hydra CX SEM.

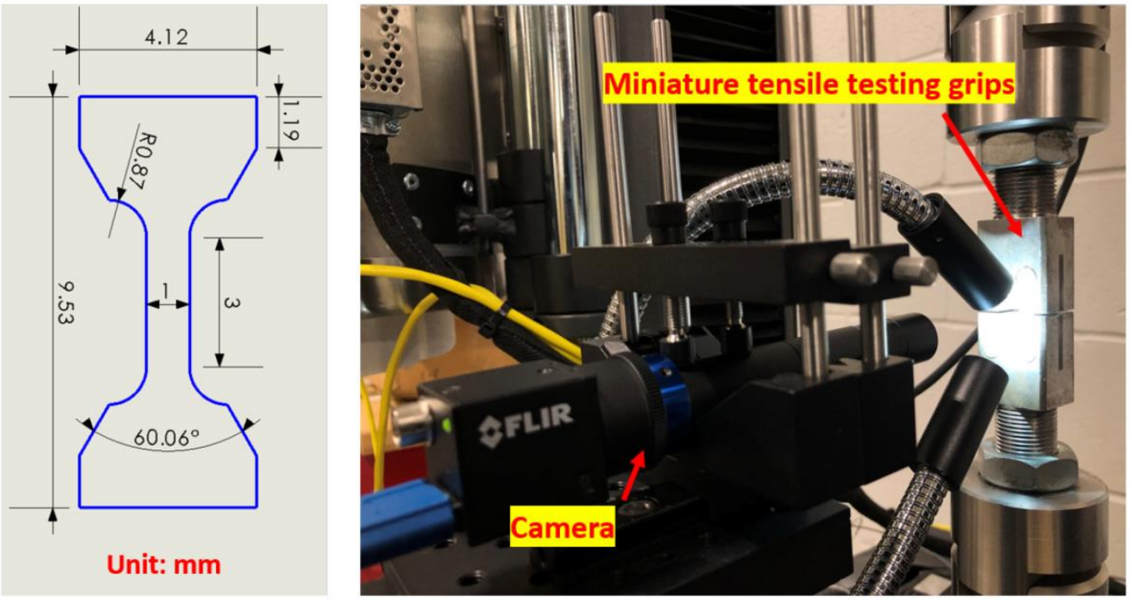

(a) (b)

Figure 2. (a) The sketch of the miniature tensile specimen design. (b) The camera setup for DIC.

Differential scanning calorimetry (DSC) was used for studying the TTs of various sections of the as-deposited Ti–Ni–Cu/TiNi bi-metallic structure using a TA Instruments Q2000 differential scanning calorimeter (New Castle, DE, USA) with a ramping heating/cooling rate of 10 °C/min. Apart from DSC, the shape-memory effect of the as-deposited bi-metallic SMA was tested by recording the shape recovery on a hot plate with changing temperatures.

3. RESULTS AND DISCUSSIONS

3.1. MICROSTRUCTURAL CHARACTERIZATION

Figure 3 shows the micrographs of the as-deposited Ti–Ni–Cu alloy. Figure 3a is an OM image of the interface between the DED Ti–Ni–Cu alloy and the TiNi substrate. A clear interfacial line can be observed and no gas pores and cracks are found near the interfacial line, which indicates a good interaction between the powder flow of the first layer and the substrate materials within the melt pool. Figure 3b is obtained from the Ti–Ni–Cu alloy section, where darker phases distribute within the matrix and form a columnar microstructure. With the assistance of SEM/EDS, higher magnification images are acquired and shown in Figure 3c,d. In Figure 3c, EDS points analysis was performed within both the matrix (Point 1) and the dark minor phase (Point 2). The atomic compositions from the EDS analysis of Point 1 and Point 2 are listed in Figure 3c. It can be seen that in the dark phases, the atomic composition of Ti is twice the atomic composition of (Ni + Cu). Therefore, the dark minor phases are Ti_2Ni intermetallics, which are marked in Figure 3b. The composition of Point 1 indicates that the matrix is Ti-rich TiNi with a Ti atomic composition of about 51.5 at.% and a small number of Cu atoms to replace the Ni atoms. The high magnification image of Figure 3d clearly shows the martensite twinning structure and dark Ti_2Ni particles. Large-area EDS analysis was also performed at heights of Z = 10 mm, 12 mm, 14 mm, 16 mm, and 18 mm of the Ti–Ni–Cu alloy section. The average atomic composition of the five heights measured by EDS is Ti (52.1 ± 0.5) Ni (43.3 ± 0.9) Cu (4.6 ± 0.4). The fluctuation of Ti, Ni, and Cu compositions among the five heights is much lower than the former work that deposited Ti–45at.%Ni–5at.%Cu alloy on the titanium substrates [29]. The dilution from the TiNi substrate in this work has less influence on the as-deposited section. The SEM image of the interfacial region is demonstrated in Figure 4a. Figure 4b–d are the EDS mapping of the Ti, Ni, and Cu elements. It can be seen that the Cu signal is much weaker below the interfacial line; however, there is not a significant change in the signal of Ti and Ni between the area above and below the interface, since the compositions of Ti and Ni within the Ti–Ni–Cu alloy and TiNi substrate are similar. The Ni signal shows a gradual and slight decrease from the TiNi substrate area to the Ti–Ni–Cu alloy area since the atomic composition of Ni in the substrate is a little higher than the Ti–Ni–Cu alloy.

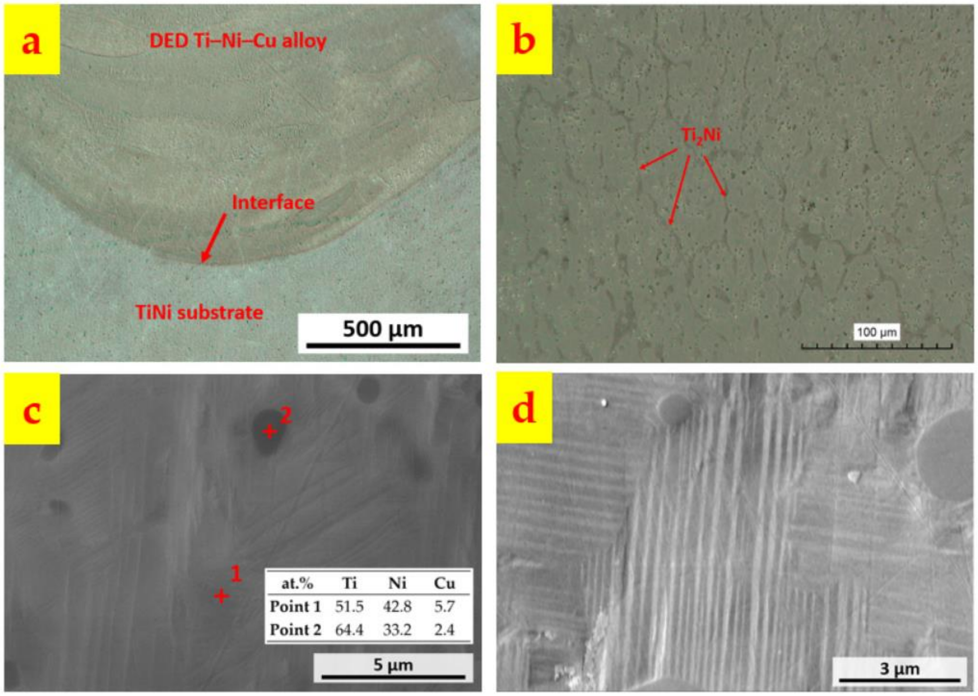

at.%	Ti	Ni	Cu
Point 1	51.5	42.8	5.7
Point 2	64.4	33.2	2.4

Figure 3. Microstructural features of the as-deposited Ti–Ni–Cu SMA. (a) Interfacial region between the DED Ti–Ni–Cu SMA and the TiNi substrate. (b) Microstructure of TiNi matrix and Ti_2Ni. (c) EDS point analysis of TiNi matrix and Ti_2Ni. (d) Twinning structure of martensitic TiNi phase.

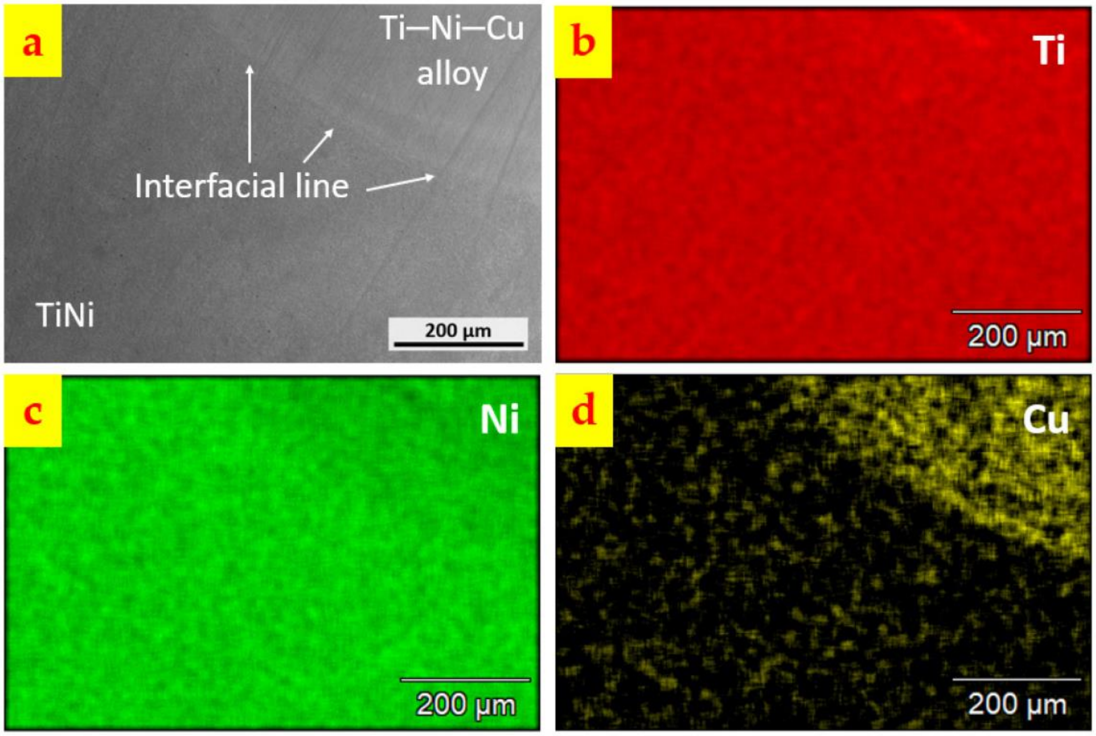

Figure 4. (a) Interface between the DED Ti–Ni–Cu alloy and the TiNi substrate. (b) Element mapping of Ti. (c) Element mapping of Ni. (d) Element mapping of Cu. Notice that the intensity of the Cu signal from the Ti–Ni–Cu alloy above the interfacial line is much stronger than the area within the TiNi substrate below the interfacial line.

3.2. HARDNESS DISTRIBUTION

Vickers hardness distribution from Z = 1 mm to Z = 19 mm with a 1 mm interval is plotted in Figure 5. Figure 5 shows the average hardness of the three indentations at each Z height. It can be seen that the Vickers hardness distribution from bottom to top shows typical low hardness (200~300 HV0.2) of the entire cross-sectional area along the Z direction of the bi-metallic structure. It was reported in [31] that the hardness of the intermetallic Ti_2Ni phase could be as high as 700 HV. Thus, the low hardness reflects that the major phase of this bi-metallic structure is the TiNi phase, and the Ti_2Ni intermetallic phase is the dispersive secondary phase in the as-deposited Ti–Ni–Cu alloy section due to the rich atomic composition of the Ti element. Almost all of the average hardness values of the DED Ti–Ni–Cu alloy (above Z = 10 mm) are within the range of 200~250 HV0.2. Within the substrate, from Z = 1 mm to Z = 9 mm, an obvious difference in the average hardness value can be observed between the lower half of the substrate and the upper half of the substrate. The average hardness values of the lower half of the substrate (Z < 6 mm) are closer to 300 HV0.2. The hardness also obtains a higher value at the location of Z = 10 mm, which could be due to the local mixing of the Ti, Ni, and Cu elements between the TiNi substrate and the first layer of DED Ti–Ni–Cu alloy that might result in a local small composition deviation in the TiNi matrix compared to the original TiNi substrate.

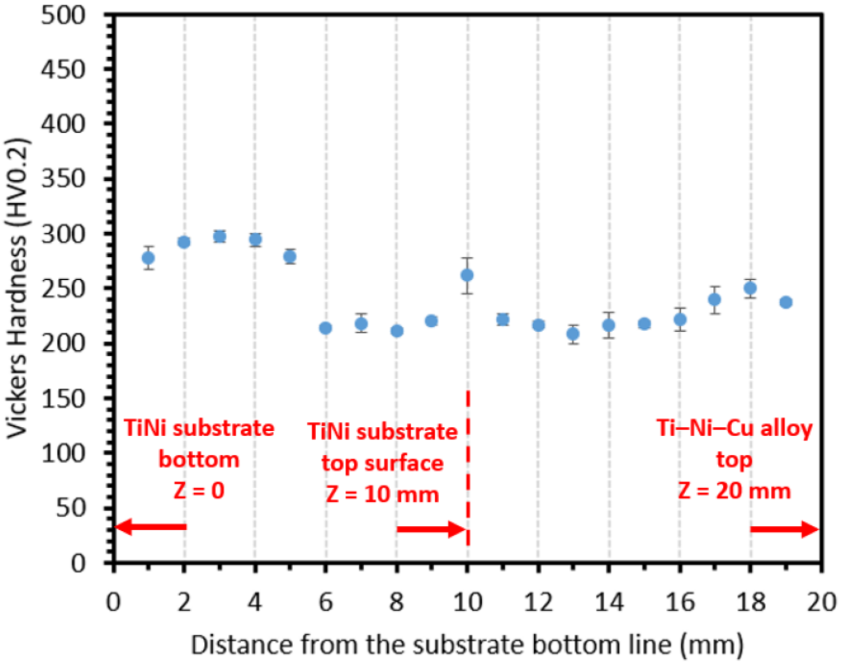

Figure 5. Vickers hardness distribution from the bottom of the TiNi substrate to the top of the DED Ti–Ni–Cu alloy. Notice that the lack of high hardness value from the hard intermetallics indicates that the major phase is the TiNi phase. Relatively higher hardness values can be observed at the lower section of the substrate from Z = 1 mm to Z = 5 mm and at the point of Z = 10 mm near the interface.

To obtain more information related to the Z-height-dependent hardness value, the sample sectioning plan for the following DSC analysis is designed according to the dashed boxes in Figure 1b. From bottom to top, they are the lower part of the substrate (SL, Z height: 0~3 mm), the middle part of the substrate (SM, Z height: 3~5.5 mm), the upper part of the substrate (SU, Z height: 5.5~8 mm), the interface including both the substrate and the bottom region of the DED Ti–Ni–Cu alloy (IN, Z height: 8~12 mm), the lower part of the DED Ti–Ni–Cu alloy (DL, Z height: 12~16 mm), and the upper part of the DED Ti–Ni–Cu alloy (DU, Z height: 16~20 mm). In this way, the phase-transition behaviors of samples SL and SM represent the lower half region of the substrate with higher average hardness, and sample SU reflects the upper half region of the substrate with lower average hardness.

3.3. PHASE TRANSFORMATION

DSC results in all six different sections: DU, DL, IN, SU, SM, and SL, according to Figure 1b, are demonstrated in Figure 6 from Figure 6a–f, respectively. Each DSC curve consists of a heating and cooling cycle with peaks that indicate the austenite formation during heating and the martensite formation during cooling. Typical characterization temperatures, including martensite starting temperature (M_s), martensite finishing temperature (M_f), austenite starting temperature (A_s), and austenite finishing temperature (A_f), are determined by the tangent method [32] as shown in the DSC curve of sample DU in Figure 6a. Austenite peak temperature (A_p) and martensite peak temperature (M_p) are also included.

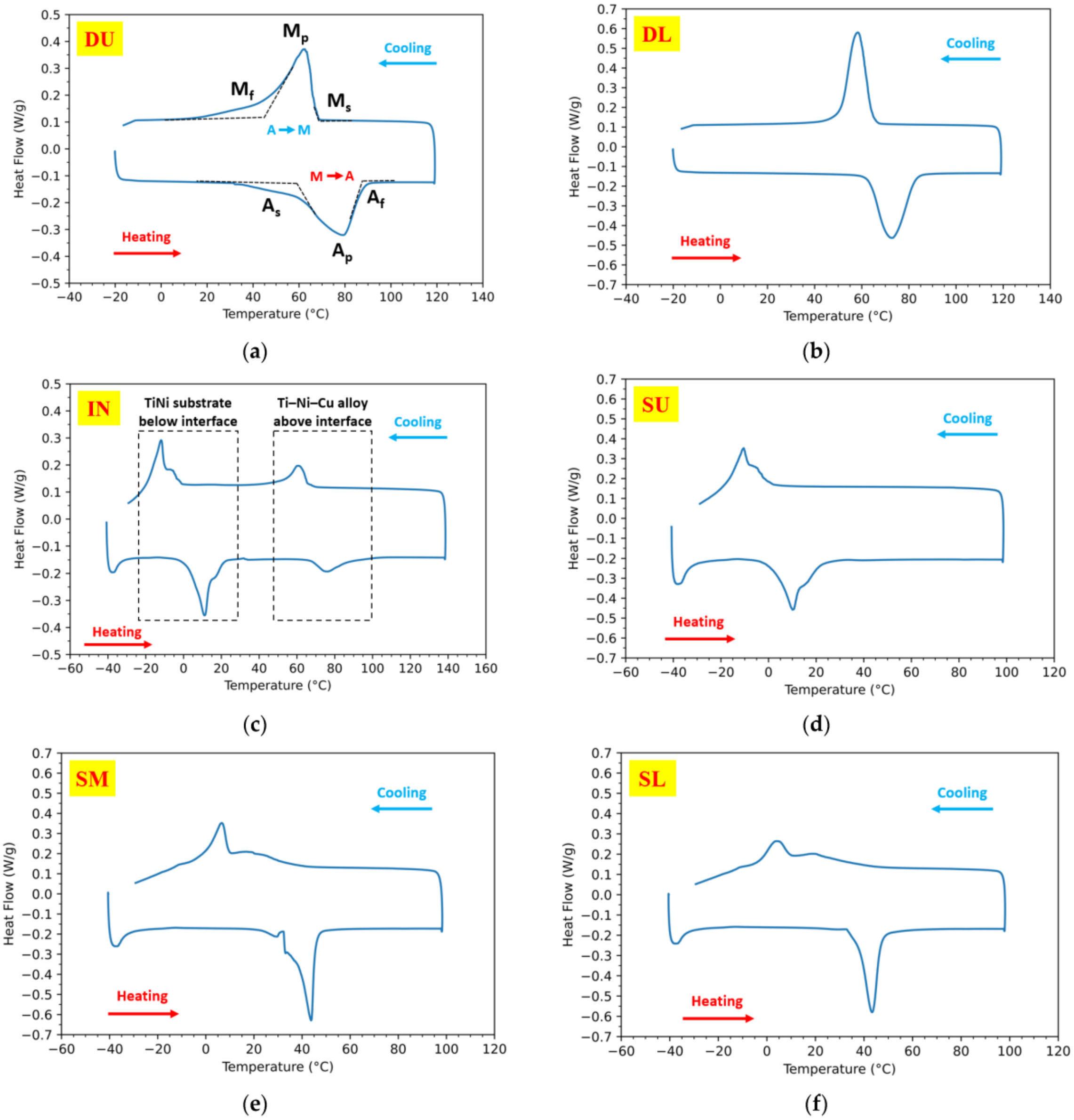

(a) (b)

(c) (d)

(e) (f)

Figure 6. DSC heating–cooling curves of the six regions (marked in Figure 1b) of the as-deposited bi-metallic SMA. (a) The upper part of the DED Ti–Ni–Cu alloy (DU). The characterization temperatures: austenite starting temperature (A_s), austenite peak temperature (A_p), austenite finishing temperature (A_f), martensite starting temperature (M_s), martensite peak temperature (M_p), and martensite finishing temperature (M_f) are labeled. (b) The lower part of the DED Ti–Ni–Cu alloy (DL). (c) The interfacial region (IN). Notice that there are two distinctive phase-transformation peaks during heating and cooling from Ti–Ni–Cu alloy and TiNi substrate, which are marked by dashed boxes. (d) The upper part of the substrate (SU). (e) The middle part of the substrate (SM). (f) The lower part of the substrate (SL).

Table 1 summarizes the A_f of all sections. Figure 6 shows that the Ti-rich upper Ti–Ni–Cu alloy shows a higher austenite finishing temperature A_f. As for the sections DU and DL, the TiNi matrix is highly Ti-rich and the A_f reaches higher than 80 °C. The DSC curve of the IN sample with the interface has two distinctive peaks both during heating and during cooling in Figure 6c, which are marked by dashed boxes. The high-temperature peaks come from the Ti-rich Ti–Ni–Cu alloy portion above the interface, whereas the low-temperature peaks are due to the equiatomic TiNi substrate below the interface. So, after the joining by DED, both phase-transformation behaviors of the two sections near the interface can still be clearly illustrated in DSC. For the substrate, at the upper part of the substrate, which includes the lower half of IN and the section of SU, the values of A_f are as low as 21.2 °C and 22.8 °C, whereas the A_f values of the SM and SL are 46.5 °C and 47.7 °C.

Table 1. Summary of the A_f value of all sections within the bi-metallic SMA structure and the corresponding Z heights.

Sample Section	**A_f (°C)**
DU	88.3
DL	82.9
IN (above interface)	90.9
IN (below interface)	21.2
SU	22.8
SM	46.5
SL	47.7

It can also be seen that all of the samples from the Ti–Ni–Cu alloy section exhibit one-step phase transformation in both the heating and cooling processes. For the substrate, during cooling the upper half of the substrate, IN and SU, exhibit features close to one-step martensite transformation, whereas the cooling curves of the lower part including SM and SL are closer to double overlapped peaks during cooling, which could be related to the intermediate R-phase [33,34] that initially exists in the substrate. For the near-equiatomic TiNi substrate used in this work, the upper part went through repeated high-temperature annealing from the laser, which tends to exhibit lower TTs and one-step austenite-martensite transition after annealing [33,35]. The lower part of the substrate, SM and SL, which are far from the deposited part, underwent a relatively lower heating temperature; the TTs are not highly affected by the laser-annealing processes. It was also reported that the formation of the R-phase can be favored by secondary precipitates such as Ni_4Ti_3 and dislocation substructures [36]. Therefore, the higher hardness values of the lower substrate from Z = 1 mm to Z = 5 mm are likely from the existence of precipitates and dislocation substructures. In contrast, the high-temperature annealing effect at the upper substrate reduces the hardness due to the reduction in those factors.

The thermal hysteresis ΔT is defined by the temperature difference between A_p and M_p [37]. The ΔT value of the DED Ti–Ni–Cu alloy section was calculated for the whole Ti–Ni–Cu alloy section. The ΔT values of DU, DL, and the upper part of IN ranges from 14.4 °C to 17.2 °C, which is narrower than reported additively manufactured Ti-rich TiNi binary SMAs such as in [38]. This then shows the effects of the addition of the Cu element in using the AM process to fabricate TiNi-based SMAs.

3.4. TENSILE BEHAVIOR

The DIC technique was applied using GOM Correlate software to plot the stress–strain curve of the bi-metal under a uniaxial load using the function of the virtual extensometer. A testing sample was extracted vertically across the interface with the half-gauge section belonging to the DED Ti–Ni–Cu alloy single wall and the other half gauge located within the TiNi substrate according to the design in Figure 2a, as seen in the dashed rectangular box in the lower right corner of Figure 7. Thus, the axial direction of the sample and the tensile loading direction are parallel to the Z axis shown in Figure 1. The tensile stress–strain curve is shown in Figure 7, which demonstrates the typical stages of SMA. In order to obtain a good alignment on the miniature tensile specimen, a preload was applied at the beginning of the uniaxial tensile testing. The first near-linear section mainly corresponds to the initial elastic response. After the initial elastic stage, the curve starts a near-horizontal stress plateau, which mainly comes from the stress-induced martensite formation of the austenite-dominated top part of the TiNi substrate (the lower half of the IN section) [39]. After the plateau, the curve goes into the elastic stage of the detwinned martensitic structure, followed by plastic deformation after the elastic region [39]. It can be seen from the stress–strain curve of the sample in Figure 7 that the sample obtains an ultimate tensile strength σUTS of 569.1 MPa. The total tensile strain at the fracture is about 8.2%. The local axial strain (ε) within the gauge section when the total tensile strain reaches 0, 1%, 2%, 3%, 4%, 5%, 6%, 7%, and 8% are mapped and shown in Figure 8. From the entire evolution of the strain map, it can be observed that as the tensile load increases, the gauge shows two distinctive sections with higher local axial strain in the TiNi substrate (approximately 10%) and lower local axial strain in the DED Ti–Ni–Cu alloy (approximately 4~5%). Anomalous points start to appear in the strain map near the interface when the total tensile strain reaches 8% due to crack formation. Therefore, the mechanical behavior at different sections of the bi-metallic SMA can be clearly tracked using the DIC technique.

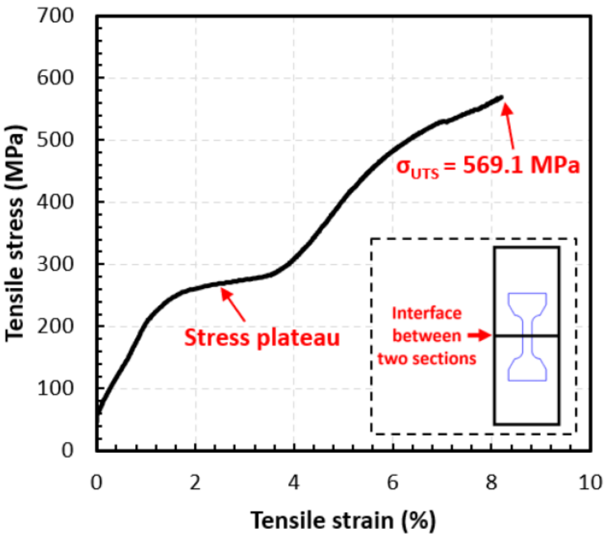

Figure 7. The stress–strain curve of the DED as-deposited bi-metallic structure. The miniature tensile sample was extracted with the interfacial line located at the center of the gauge section.

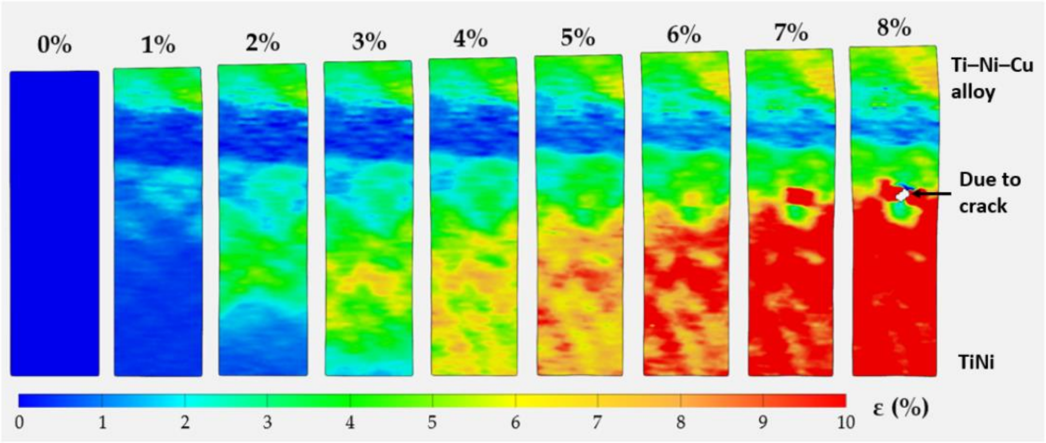

Figure 8. The strain map of the local axial strain within the gauge section at the moments when the total tensile strain equals 0, 1%, 2%, 3%, 4%, 5%, 6%, 7%, and 8%.

The SEM images of the details on the fracture surface of the sample are shown in Figure 9. Figure 9a,b shows the ductile regions where the dimple-like structure dominates, whereas the feature in Figure 9c,d shows low ductility. Figure 9c includes both local dimples and cleavage regions, and in the higher magnification image of Figure 9d, it also has perpendicular patterns marked by perpendicular short, dashed lines, which may correspond to the martensite twinning structure within the Ti–Ni–Cu alloy single-wall section shown in Figure 3d. Also, the dark particles can be found in Figure 9d. Figure 9e–h represent the SEM/EDS mapping of the long, dashed rectangular area in Figure 9d. The Ti, Ni, Cu element mapping of Figure 9e indicates that the dark particle could be Ti_2Ni, which may act as a stress concentrator near the interface that initiates the cracking under the tensile loading.

3.5. DEMONSTRATION OF MULTIPLE SHAPE-MEMORY EFFECT

The multiple shape-memory behavior is demonstrated by a cross-section slice from the as-deposited bi-metallic SMA. Both the DED Ti–Ni–Cu alloy side and the TiNi substrate side are bent compared to the original straight shape. After bending, the bi-metallic SMA piece was then placed on a hot plate at 70 °C, which is higher than (A_f + 20 °C) of the TiNi substrate, as seen in Figure 10a. Figure 10b–d capture the shape change of the bi-metallic SMA on the hot plate at 70 °C after 10 s, 15 s, and 30 s, respectively. It can be noticed that at 70 °C, the curved TiNi substrate side gradually changes back to the straight status. In comparison, the Ti–Ni–Cu alloy side keeps the curved shape since the temperature of 70 °C is not able to complete the martensite-austenite transition of the Ti–Ni–Cu alloy section. As the time reaches 60 s, the hot plate temperature starts to rise and finally reaches 120 °C. Figure 10e shows that at 120 °C, which is higher than the (A_f + 20 °C) of the DED Ti–Ni–Cu alloy part, the Ti–Ni–Cu alloy side also recovers to the original straight state. Therefore, the multiple shape-memory behaviors at two sides of the bi-metallic structure are identified.

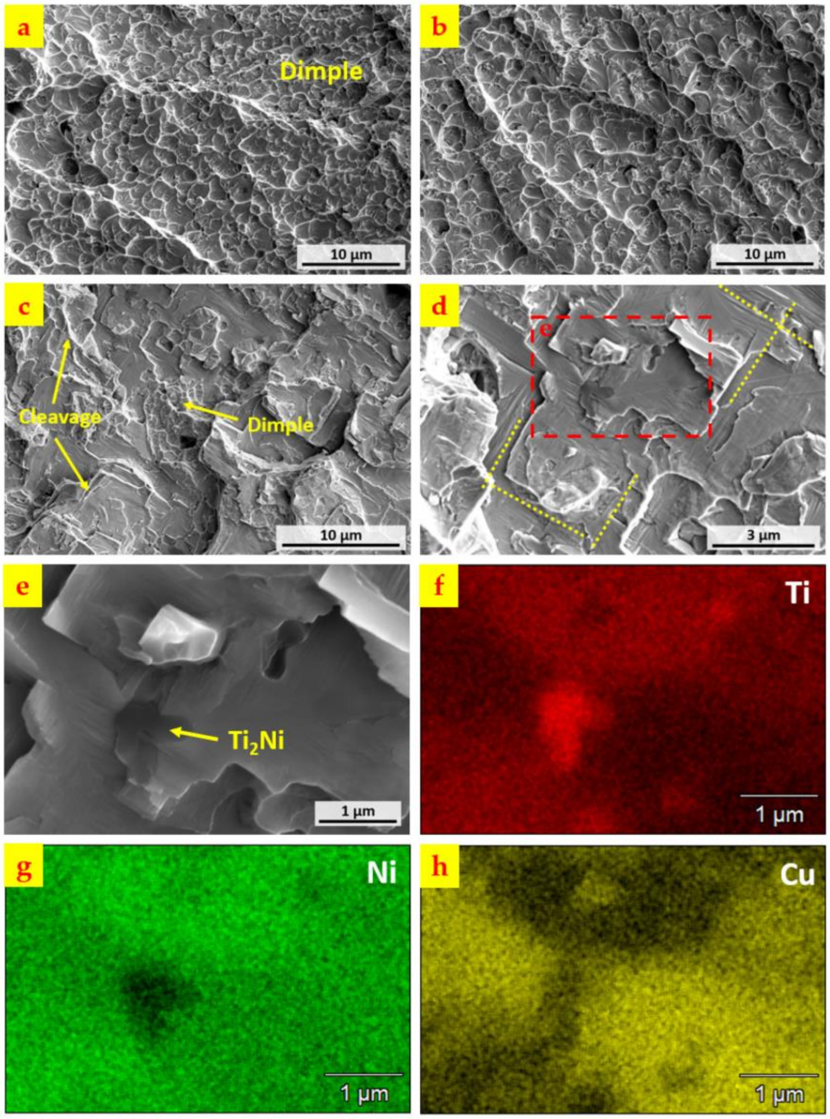

Figure 9. (a,b) Dimple-like ductile area of the fracture surface. (c,d) Brittle area of the fracture surface. (e) High magnification image of (d) in long, dashed rectangular box. (f) Element mapping of Ti in (e). (g) Element mapping of Ni in (e). (h) Element mapping of Cu in (e).

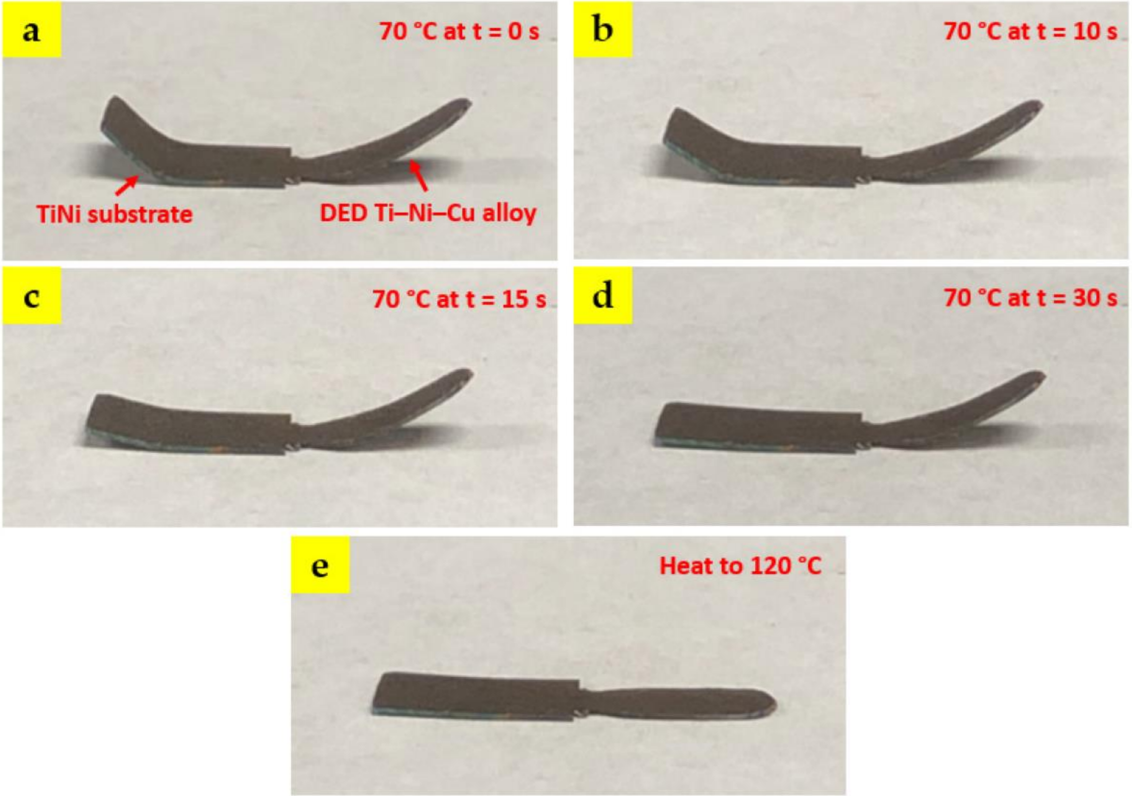

Figure 10. Demonstration of the SMA using a hot plate at 70 °C and 120 °C: (a) The bi-metallic SMA sample was bent at both the TiNi substrate side and the DED Ti–Ni–Cu alloy side and placed at 70 °C at t = 0 s. (b) t = 10 s. (c) t = 15 s. (d) t = 30 s. Notice that the TiNi substrate has almost recovered to the original status, whereas the Ti–Ni–Cu alloy side keeps the curved shape. (e) The hot plate was then heated from 70 °C to 120 °C. Finally, the Ti–Ni–Cu alloy side recovers.

4. CONCLUSIONS

In this work, a Ti-rich Ti–Ni–Cu ternary SMA with an as-mixed atomic composition of Ti–44at.%Ni–3at.%Cu was fabricated on a near-equiatomic commercial TiNi binary SMA substrate, which shows the capability of the elemental powder DED process to join two different types of SMA sections and build SMAs with multiple shape-memory behaviors. The findings from studying the microstructural, mechanical, and functional behaviors of the as-fabricated bi-metallic SMA are summarized below.

Microscopic imaging revealed the dense metallurgical bonding between the as-deposited Ti–Ni–Cu alloy part and the TiNi substrate with no gas pores or cracks being seen at the interface. The TiNi matrix phase and Ti_2Ni minor phase are identified by EDS, and the martensite twinning structure is observed within the TiNi matrix phase of the as-deposited Ti–Ni–Cu alloy section.

Vickers hardness distribution from bottom to top shows the typical low hardness (200~300 HV 0.2) of SMAs across the entire cross-section. All major phases are TiNi phases rather than Ti_2Ni hard intermetallic phases, and Ti_2Ni is the main secondary phase in the Ti–Ni–Cu alloy section.

Tensile testing combined with the DIC technique on a miniature tensile sample shows a bonding strength of 569.1 MPa and the fracture occurs at 8.2% total tensile strain. DIC strain mapping indicates the difference in local axial strain distribution between two sections of different SMA types, which are approximately 4~5% in the Ti–Ni–Cu alloy side and approximately 10% in the TiNi substrate.

DSC analysis at different sections shows that the Ti-rich DED Ti–Ni–Cu alloy shows higher A_f. For the near-equiatomic TiNi substrate, the lower half of the substrate maintains a higher A_f and more obvious R-phase features than the upper half of the substrate since the upper part went through higher temperature annealing from laser power, which tends to exhibit lower TTs and a single austenite-martensite transition without an R-phase.

The shape-memory behavior is tested by an as-deposited bi-metallic slice at 70 °C and 120 °C. At 70 °C, shape recovery occurs only at the TiNi substrate side, whereas when the temperature reaches 120 °C, both sides perform the shape recovery. Future studies will include the heat treatment effect on the microstructure and functional properties of DED bi-metallic SMAs.

FUNDING

This research was partially funded by the U.S. Department of Energy STTR Contract DE-SC0018879, the National Science Foundation Grants CMMI 1625736, and the Material Research Center at Missouri S&T. Their financial support is greatly appreciated.

ACKNOWLEDGMENTS

The authors would like to thank the Intelligent Systems Center, Material Research Center, and Department of Chemistry Shared Instruments Lab at Missouri S&T for all the research support.

REFERENCES

1. Cai, W.; Daehn, G.; Vivek, A.; Li, J.; Khan, H.; Mishra, R.S.; Komarasamy, M. A state-of-the-art review on solid-state metal joining. J. Manuf. Sci. Eng. 2019, 141, 031012.

2. Sahasrabudhe, H.; Harrison, R.; Carpenter, C.; Bandyopadhyay, A. Stainless steel to titanium bimetallic structure using LENS™. Addit. Manuf. 2015, 5, 1–8.

3. Rajesh Kannan, A.; Mohan Kumar, S.; Pramod, R.; Pravin Kumar, N.; Siva Shanmugam, N.; Palguna, Y. Microstructure and mechanical properties of wire arc additive manufactured bi-metallic structure. Sci. Technol. Weld. Join. 2020, 26, 47–57.

4. Feenstra, D.R.; Molotnikov, A.; Birbilis, N. Effect of energy density on the interface evolution of stainless steel 316L deposited upon INC 625 via directed energy deposition. J. Mater. Sci. 2020, 55, 13314–13328.

5. Piscopo, G.; Iuliano, L. Current research and industrial application of laser powder directed energy deposition. Int. J. Adv. Manuf. Technol. 2022, 119, 6893–6917.

6. Ahn, D.G. Directed energy deposition (DED) process: State of the art. Int. J. Precis. Eng. Manuf.-Green Technol. 2021, 8, 703–742.

7. Saboori, A.; Aversa, A.; Marchese, G.; Biamino, S.; Lombardi, M.; Fino, P. Application of directed energy deposition-based additive manufacturing in repair. Appl. Sci. 2019, 9, 3316.

8. Carroll, B.E.; Otis, R.A.; Borgonia, J.P.; Suh, J.O.; Dillon, R.P.; Shapiro, A.A.; Hofmann, D.C.; Liu, Z.K.; Beese, A.M. Functionally graded material of 304L stainless steel and inconel 625 fabricated by directed energy deposition: Characterization and thermodynamic modeling. Acta Materialia 2016, 108, 46–54.

9. Feenstra, D.R.; Banerjee, R.; Fraser, H.L.; Huang, A.; Molotnikov, A.; Birbilis, N. Critical review of the state of the art in multi-material fabrication via directed energy deposition. Curr. Opin. Solid State Mater. Sci. 2021, 25, 100924.

10. Mosallanejad, M.H.; Niroumand, B.; Aversa, A.; Saboori, A. In-situ alloying in laser-based additive manufacturing processes: A critical review. J. Alloy. Compd. 2021, 872, 159567.

11. Jones, N.F.; Beuth, J.L.; de Boer, M.P. Directed energy deposition joining of Inconel 625 to 304 stainless steel with direct bonding. J. Mater. Res. 2021, 36, 3701–3712.

12. Zhang, X.; Li, L.; Pan, T.; Chen, Y.; Zhang, Y.; Li, W.; Liou, F. Additive manufacturing of copper-tool steel dissimilar joining: Experimental characterization and thermal modeling. Mater. Charact. 2020, 170, 110692.

13. Khodabakhshi, F.; Farshidianfar, M.H.; Bakhshivash, S.; Gerlich, A.P.; Khajepour, A. Dissimilar metals deposition by directed energy based on powder-fed laser additive manufacturing. J. Manuf. Processes 2019, 43, 83–97.

14. Reichardt, A.; Dillon, R.P.; Borgonia, J.P.; Shapiro, A.A.; McEnerney, B.W.; Momose, T.; Hosemann, P. Development and characterization of Ti-6Al-4V to 304L stainless steel gradient components fabricated with laser deposition additive manufacturing. Materials Design 2016, 104, 404–413.

15. Banait, S.M.; Paul, C.P.; Jinoop, A.N.; Kumar, H.; Pawade, R.S.; Bindra, K.S. Experimental investigation on laser directed energy deposition of functionally graded layers of Ni-Cr-B-Si and SS316L. Opt. Laser Technol. 2020, 121, 105787.

16. Jani, J.M.; Leary, M.; Subic, A.; Gibson, M.A. A review of shape memory alloy research, applications and opportunities. Mater. Des. 2014, 56, 1078–1113.

17. Otsuka, K.; Ren, X. Physical metallurgy of Ti–Ni-based shape memory alloys. Prog. Mater. Sci. 2005, 50, 511–678.

18. Gloanec, A.L.; Bilotta, G.; Gerland, M. Deformation mechanisms in a TiNi shape memory alloy during cyclic loading. Mater. Sci. Eng. A 2013, 564, 351–358.

19. Liu, Y.; Shan, L.; Shan, J.; Hui, M. Experimental study on temperature evolution and strain rate effect on phase transformation of TiNi shape memory alloy under shock loading. Int. J. Mech. Sci. 2019, 156, 342–354.

20. Lah, A.Š.; Fajfar, P.; Lavrič, Z.; Bukošek, V.; Rijavec, T. Preparation of Shape Memory NiTiNOL Filaments for Smart Textiles. Tekstilec 2016, 59, 168–174.

21. Khan, M.I.; Pequegnat, A.; Zhou, Y.N. Multiple memory shape memory alloys. Adv. Eng. Mater. 2013, 15, 386–393.

22. Nematollahi, M.; Safaei, K.; Bayati, P.; Elahinia, M. Functionally graded NiTi shape memory alloy: Selective laser melting fabrication and multi-scale characterization. Mater. Lett. 2021, 292, 129648.

23. Liang, Y.; Jiang, S.; Zhang, Y.; Hu, L.; Zhao, C. Microstructure evolution and deformation mechanism of NiTiFe shape memory alloy based on plane strain compression and subsequent annealing. Mater. Chem. Phys. 2018, 215, 112–120.

24. Chang, S.H.; Chiu, W.C. Selective leaching and surface properties of Ti50Ni50−xCux (x = 0–20 at.%) shape memory alloys for biomedical applications. Appl. Surf. Sci. 2015, 324, 106–113.

25. Jhou, W.-T.; Wang, C.; Ii, S.; Chiang, H.-S.; Hsueh, C.-H. TiNiCuAg shape memory alloy films for biomedical applications. J. Alloy. Compd. 2018, 738, 336–344.

26. Chen, Y.; Zhang, X.; Parvez, M.M.; Liou, F. A review on metallic alloys fabrication using elemental powder blends by laser powder directed energy deposition process. Materials 2020, 13, 3562.

27. Schwendner, K.I.; Banerjee, R.; Collins, P.C.; Brice, C.A.; Fraser, H.L. Direct laser deposition of alloys from elemental powder blends. Scr. Mater. 2001, 45, 1123–1129.

28. Shiva, S.; Palani, I.A.; Paul, C.P.; Mishra, S.K.; Singh, B. Investigations on phase transformation and mechanical characteristics of laser additive manufactured TiNiCu shape memory alloy structures. J. Mater. Process. Technol. 2016, 238, 142–151.

29. Chen, Y.; Zhang, X.; Parvez, M.M.; Newkirk, J.W.; Liou, F. Fabricating TiNiCu Ternary Shape Memory Alloy by Directed Energy Deposition via Elemental Metal Powders. Appl. Sci. 2021, 11, 4863.

30. Karnati, S.; Axelsen, I.; Liou, F.F.; Newkirk, J.W. Investigation of tensile properties of bulk and SLM fabricated 304L stainless steel using various gage length specimens. In Proceedings of the 2016 International Solid Freeform Fabrication Symposium. University of Texas at Austin, Austin, TX, USA, 8–10 August 2016.

31. Ren, H.S.; Xiong, H.P.; Pang, S.J.; Chen, B.; Wu, X.; Cheng, Y.Y.; Chen, B.Q. Microstructures and mechanical properties of transient liquid-phase diffusion-bonded Ti3Al/TiAl joints with TiZrCuNi interlayer. Metall. Mater. Trans. A 2016, 47, 1668–1676.

32. De Araújo, C.J.; Da Silva, N.J.; Da Silva, M.M.; Gonzalez, C.H. A comparative study of Ni–Ti and Ni–Ti–Cu shape memory alloy processed by plasma melting and injection molding. Mater. Des. 2011, 32, 4925–4930.

33. Xu, L.; Wang, R. The effect of annealing and cold-drawing on the super-elasticity of the Ni-Ti shape memory alloy wire. Mod. Appl. Sci. 2010, 4, 109.

34. Zhao, C.; Liang, H.; Luo, S.; Yang, J.; Wang, Z. The effect of energy input on reaction, phase transition and shape memory effect of NiTi alloy by selective laser melting. J. Alloy. Compd. 2020, 817, 153288.

35. López-Medina, M.; Hernández-Navarro, F.; Flores-Zúñiga, H.; Soto-Parra, D.E. Reversible elastocaloric effect related to B2–R transformation in Ni50. 5Ti49. 5 alloy. J. Appl. Phys. 2021, 129, 115104.

36. Carroll, M.C.; Somsen, C.; Eggeler, G. Multiple-step martensitic transformations in Ni-rich NiTi shape memory alloys. Scr. Mater. 2004, 50, 187–192.

37. Shahmir, H.; Nili-Ahmadabadi, M.; Huang, Y.; Langdon, T.G. Evolution of microstructure and hardness in NiTi shape memory alloys processed by high-pressure torsion. J. Mater. Sci. 2014, 49, 2998–3009.

38. Li, S.; Hassanin, H.; Attallah, M.M.; Adkins, N.J.; Essa, K. The development of TiNi-based negative Poisson's ratio structure using selective laser melting. Acta Mater. 2016, 105, 75–83.

39. Gall, K.; Tyber, J.; Brice, V.; Frick, C.P.; Maier, H.J.; Morgan, N. Tensile deformation of NiTi wires. J. Biomed. Mater. Res. Part A Off. J. Soc. Biomater. Jpn. Soc. Biomater. Aust. Soc. Biomater. Korean Soc. Biomater. 2005, 75, 810–823.

IV. HEAT TREATMENT EFFECTS ON TI–NI–CU/TINI BI-METALLIC SHAPE MEMORY ALLOY BY ADDITIVE MANUFACTURING WITH ELEMENTAL POWDER MIXTURE

ABSTRACT

In this work, a bi-metallic Ti–Ni–Cu/TiNi shape memory alloy was fabricated using laser powder-based directed energy deposition with Ti/Ni/Cu elemental powder mixture as feedstock. Part of the as-deposited bi-metallic shape memory alloy was then heat treated at the temperature of 400 °C and 600 °C. The bi-metallic alloy parts in the as-deposited condition, 400 °C heat treatment condition, and 600 °C heat treatment condition were all characterized in microstructural, mechanical, and functional properties at multiple locations to explore the variation of the multifunctional features and shape memory properties. Microstructure analysis shows no obvious change in the Ti-rich Ti–Ni–Cu alloy section among different heat treatment effects. In contrast, within the TiNi substrate, the laser heating effect during the directed energy deposition process created a location-dependent microstructure and property distribution, and more combinations in mechanical and thermal behaviors were generated after the following post heat treatment. The work presents a good use of the directed energy deposition technique and the subsequent heat treatment to develop bi-metallic shape memory alloys with higher flexibility, lower cost, and a wider range of memory effect combinations.

1. INTRODUCTION

Additive manufacturing (AM) is becoming increasingly popular in metal parts manufacturing in all kinds of industrial environments [1–3]. Due to its high composition and geometry flexibility, metal AM can create more complicated part design and manufacturing in customizable compositions and shapes that are difficult to be realized by conventional manufacturing [4–6]. Among all metal AM processes, directed energy deposition (DED) is a major category that applies energy sources to deposit metal feedstocks layer by layer to form a 3D object [7,8]. Laser is a kind of widely used energy source, while the metal feedstocks are usually in the powder state or wire state [7,9,10].

Various metal alloys have been fabricated by DED from powders such as stainless steels, Al alloys, Ni alloys, Ti alloys, etc. [11–14]. Apart from using a single type of powder to fabricate parts with uniform chemical compositions, due to the easy-to-blend nature of powders, people have made attempts to develop composite materials using powder mixture as the raw material, such as Ti/TiC metal matrix composite [15]. Also, Since DED has the advantage of local composition selection and high flexibility in metal powder mixture choices, nowadays, researchers are also studying the capability of DED to develop novel alloy structures with more combinations of compositions and functions, such as bi-metallic structures and functionally graded metallic materials [16,17]. With the assistance of the DED process, multiple types of metals can be combined layer by layer, and functionally graded layers and interlayers can also be inserted to ensure a better joining effect [18].

TiNi-based alloy is a type of shape memory alloy (SMA), which has been widely used so far [19,20]. Traditional processing using materials subtracting methods such as conventional machining is difficult to process TiNi-based SMA, while AM process shows a great advantage in fabricating TiNi to overcome the poor machinability [21]. It was reported that TiNi SMA is possible to be synthesized by elemental powder mixture in the AM process including DED, where the mixture of Ti and Ni elemental powder has a lower material cost [22,23]. In addition, a third element can be added to the Ti–Ni alloy system to study ternary SMAs, such as adding Cu can be used to narrow down the thermal hysteresis [24]. Apart from single SMAs with only one type of functional property, for the DED AM technique, depositing one type of TiNi-based SMA on another different TiNi-based SMA substrate is also possible to realize a wide range of bi-metallic SMAs that can possibly possess multiple shape memory effects from both the substrate and the DED portion. In our previous work, a Ti-rich Ti–Ni–Cu ternary SMA bulk part was built on a near equiatomic TiNi substrate by elemental powder DED, and thus, Ti–Ni–Cu/TiNi bi-metallic structure was successfully realized, which demonstrated obvious multiple shape memory temperatures and high-quality metallurgical bonding at the interfacial zone [25].

Furthermore, both the laser heat and post heat treatment can cause changes in the microstructure and material behaviors of TiNi alloys [26–28]. While bi-metallic TiNi-based SMA structures consist of more than one type of TiNi structure, it will attract more interest in studying the heat treatment effect on the bi-metallic TiNi-based SMA fabricated by DED with respect to different locations and various heat treatment conditions. Heat treatment can be an important way to further tailor the multiple shape memory effects of bi-metallic SMAs. So far, there is very limited study on bi-metallic TiNi-based SMAs fabricated by the DED AM process using the cost-effective elemental powder feedstock and how different heat treatment conditions affect their properties at multiple different

SMA sections. In this work, studies on the effect of post heat treatment will be included to find more details on the location-dependent microstructural features, mechanical properties, and shape memory behaviors of the TiNi-based bi-metallic SMA fabricated by DED.

2. MATERIALS AND METHOD

2.1. MATERIALS AND PROCESSING

In this experiment, elemental Ti, Ni, and Cu powders were used as raw materials for the DED processing to synthesize Ti–Ni–Cu ternary SMA on the TiNi binary SMA. The details of the powders were provided in the former work [25]. The Ti, Ni, and Cu powders were weighed and mixed in an atomic composition of 53 at.% for Ti, 44 at.% for Ni, and 3 at.% for Cu. The powder mixture was then homogenized by a Turbula T2F powder mixer for 30 min before the AM process. A commercial near equiatomic TiNi binary alloy bar was used as the substrate. The substrate was in a cuboid shape with an approximate dimension of 25 mm long, 5 mm wide, and 10 mm tall. The surface of 25 mm × 5 mm was used as the top surface for the DED processing.

The DED processing system consists of an IPG Photonics YLR CW laser system, an electrostatic powder feeder supplied by Powder Motion Labs, and a CNC-controlled moving stage that can travel linearly in x-, y-, and z-direction. Figure 1a shows the schematic of the deposition process. The TiNi substrate was clamped on the moving stage by a vice. The 25 mm × 5 mm top surface was placed horizontally for the DED processing [25]. The powder mixture was delivered by the powder feeder and fed to the melt pool. A single track, multi-layer deposition toolpath was used to build a Ti–Ni–Cu ternary SMA single wall structure on the TiNi binary SMA. The Ti–Ni–Cu single wall is approximately 11 mm in height, and the length is close to 25 mm, as shown in Figure 1b. The +Y direction and –Y direction are the travel direction of the substrate, which is parallel to the long side of the single wall, while the +Z direction is the build direction. The laser power and the substrate travel speed were 600 W and 200 mm/min, respectively, for the first five layers to create a higher energy density to achieve complete mixing of the powder stream and the melt pool on the substrate. For all the remaining layers, the power switched to 400 W, and the travel speed was increased to 250 mm/min to reduce the energy density due to the heat accumulation at higher layers.

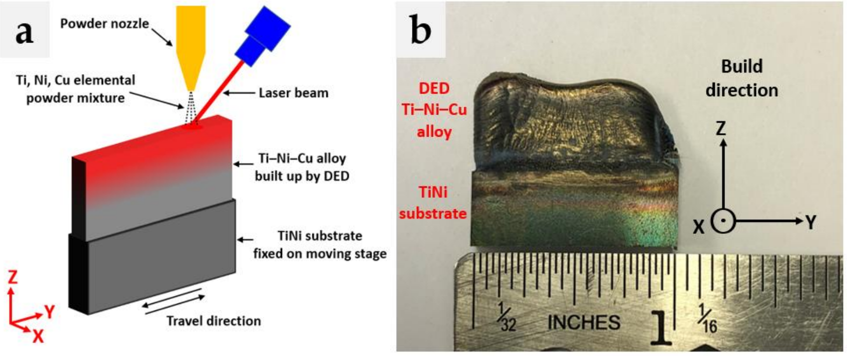

Figure 1. (a) The schematic of the DED processing in this work. (b) The picture of the as-deposited Ti–Ni–Cu/TiNi bimetallic SMA part with the defined xyz coordinate system.

2.2. CHARACTERIZATION

Cross-sectional pieces for sample preparation were cut off from the as-deposited (AD) bi-metallic SMA single wall demonstrated in Figure 1b by wire electrical discharged machining (EDM). Those pieces were divided into three groups. One group of pieces remained in the AD status. While for the other two groups, one group went through heat treatment at 400 °C for 3 hours, and the other group went through 600 °C heat treatment also for 3 hours. For both heat treatment conditions, furnace heating was conducted in a Marshall tubular furnace with an argon atmosphere. After furnace heating, pieces were taken out from the furnace and air-cooled. In this work, heat treatment conditions at 400 °C and 600 °C are also denoted as HT400 and HT600, respectively. After the heat treatment steps, all three groups of pieces in AD, HT400, and HT600 conditions were then prepared into samples to be ready for materials characterization.

Studies on microstructure features, mechanical properties, and functional properties of the bi-metallic SMA were conducted at three different height locations. One of them was in the DED Ti–Ni–Cu SMA region, while the other two locations were in the substrate section. In our previous work [25], it was also found that different height locations within the substrate section of the bi-metallic SMA demonstrated different material behaviors, which was due to the laser heating effect causing a non-constant temperature distribution along the Z direction within the substrate. Therefore, within the substrate, both an upper part location and a lower part location were selected to reveal the correlation among structures and properties at two different height locations of the substrate.

The microstructural information at three locations from the bi-metallic structure, which include the DED Ti–Ni–Cu alloy region located near the middle height of the Ti–Ni–Cu section (Z ~ 15.5 mm), the TiNi substrate upper region which is at a substrate near-top location approximately 9 mm above the bottom line of the substrate (Z ~ 9 mm) and also below the interfacial line, and the TiNi substrate lower region which is a near-bottom location approximately 1 mm above the bottom line of the substrate (Z ~ 1 mm), were selected for microscopic imaging using a Hirox KH-8700 optical microscope (OM) and a TFS Helios Hydra CX scanning electron microscope (SEM). During the SEM observation, the energy dispersive spectroscopy (EDS) analysis was also conducted. Samples for microscopic observation were mounted by epoxy, polished, and etched by Kroll's reagent. Samples made from all three heat treatment conditions (AD, HT400, and HT600) were included in the microscopic observation.

Tensile tests were conducted using an Instron 5969 universal testing machine for evaluating the mechanical response. The miniature tensile specimen was designed for small volume tensile testing, and the detail in dimension can be found in the literature [29]. Miniature tensile samples were extracted horizontally from three locations: the TiNi substrate lower region, the TiNi substrate upper region, and the DED Ti–Ni–Cu alloy region. The location information for sample extraction can be found in Figure 2. For all tests, a loading-unloading test was performed. During the loading step, a strain rate of 0.003 mm/mm/s was maintained by controlling a constant crosshead speed. When the tensile stress reached 300 MPa, unloading started with a constant unloading rate of –10 N/s. All tests used a 10 kN load cell. Before loading started, a preload was added to ensure a good alignment of the miniature tensile sample. Digital image correlation (DIC) was applied to acquire the stress-strain curve of each tensile test to capture the actual mechanical responses and compare the mechanical behaviors at various locations under different heat treatment conditions. For functional properties, differential scanning calorimetry (DSC) analysis was performed to identify the transformation temperatures. The DSC tests were carried out by a TA Instruments Q2000 DSC calorimeter. Similar to the tensile sample locations, samples from three locations of TiNi substrate lower region, TiNi substrate upper region, and the DED Ti–Ni–Cu alloy region in the AD state and the heat treatment states were also evaluated by DSC. The heating and cooling rate for DSC was set at 10 °C/min in the nitrogen atmosphere.

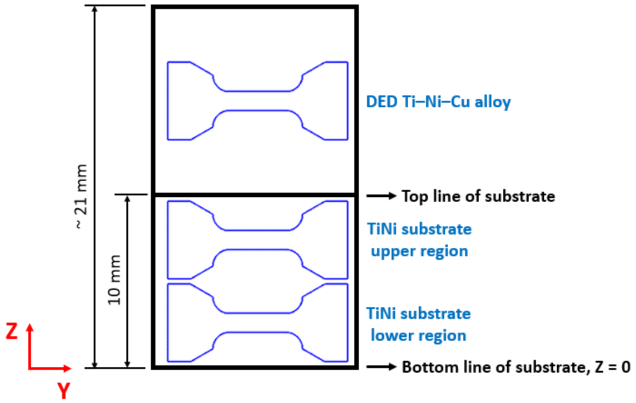

Figure 2. The Z height and coordinate information of the YZ-plane cross-section of the bi-metallic SMA and the location of the extraction of miniature tensile samples.

3. RESULT AND DISCUSSION

3.1. MICROSTRUCTURE AND PHASE

The appearance of the bi-metallic SMA cross-section at the interfacial region is shown in Figures 3a–b. It can be found that there are no defects near the interface. A clear interfacial line between the DED section and the substrate section can be seen in Figure 3b, which shows a good interface interaction between the first few layers of the Ti–Ni–Cu and the upper surface of the TiNi substrate. The first five layers with higher energy density resulted in a larger single wall width. Higher magnification SEM micrographs from the DED Ti–Ni–Cu alloy region are demonstrated in Figures 3c–d. The Ti-rich Ti–Ni–Cu alloy region mainly consists of the matrix and the secondary phase, which form in a columnar structure. The EDS point analysis was performed at Point 1 (matrix) and Point 2 (secondary phase), which gives the results of 51.2 at.% Ti, 46.1 at.% Ni, 2.7 at.% Cu for Point 1 and 66.8 at.% Ti, 32 at.% Ni, 1.2 at.% Cu for Point 2. Therefore, in the DED Ti-rich Ti–Ni–Cu alloy region, the matrix indicates the Ti-rich TiNi phase, while the secondary phase represents Ti_2Ni intermetallic.

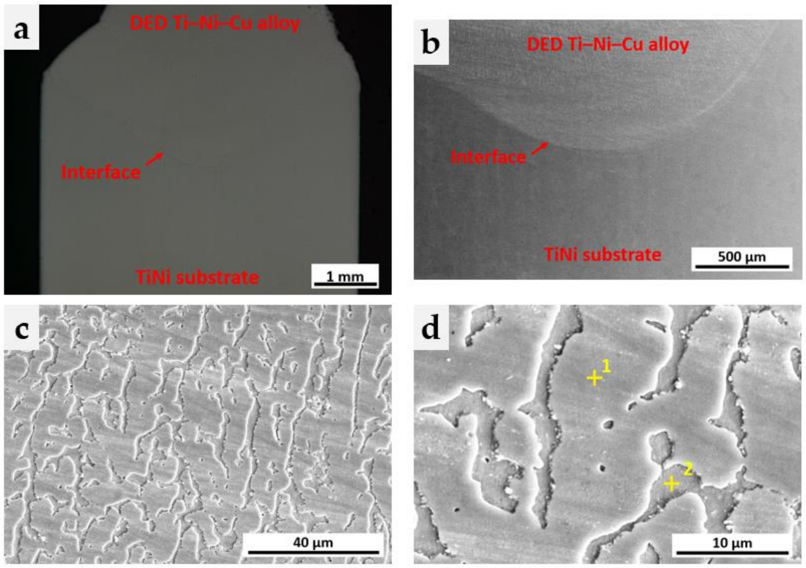

Figure 3. (a) The low magnification OM image of the AD state interfacial area. (b) The SEM image of the AD interfacial area. (c) The columnar structure of the AD Ti–Ni–Cu alloy region. (d) Higher magnification image of the Ti–Ni–Cu alloy region with Point 1 and Point 2, which are two points from different phases for EDS analysis.

The OM micrographs of three states: AD, HT400, and HT600 at three locations are listed in Figures 4a–i. Figures 4a–c are the AD, HT400, and HT600 states at the DED Ti–Ni–Cu alloy region, respectively. Similarly, Figures 4d–f show the three states at the substrate near-top region, and Figures 4g–i represent the three states at the substrate near-bottom region. Figures 4a–c show that at all three heat treatment states, the DED Ti–Ni–

Cu alloy region has same features of the Ti-rich TiNi matrix and Ti_2Ni secondary phase with columnar structures. As the DED Ti–Ni–Cu alloy consists of highly Ti-rich TiNi matrix (around 51 at.% in Ti composition) and Ti_2Ni, there are no obvious changes in phase constituent at various heat treatment conditions. On the other hand, equiaxed grain structures can be clearly seen in Figures 4d–i from the substrate region. The grain structure of the near equiatomic TiNi alloy is similar to the microstructure found in the literature [30]. Differences in minor phase features within grains can be clearly seen within the substrate region, especially in the status of AD and HT400 shown in Figures 4d,e,g,h.

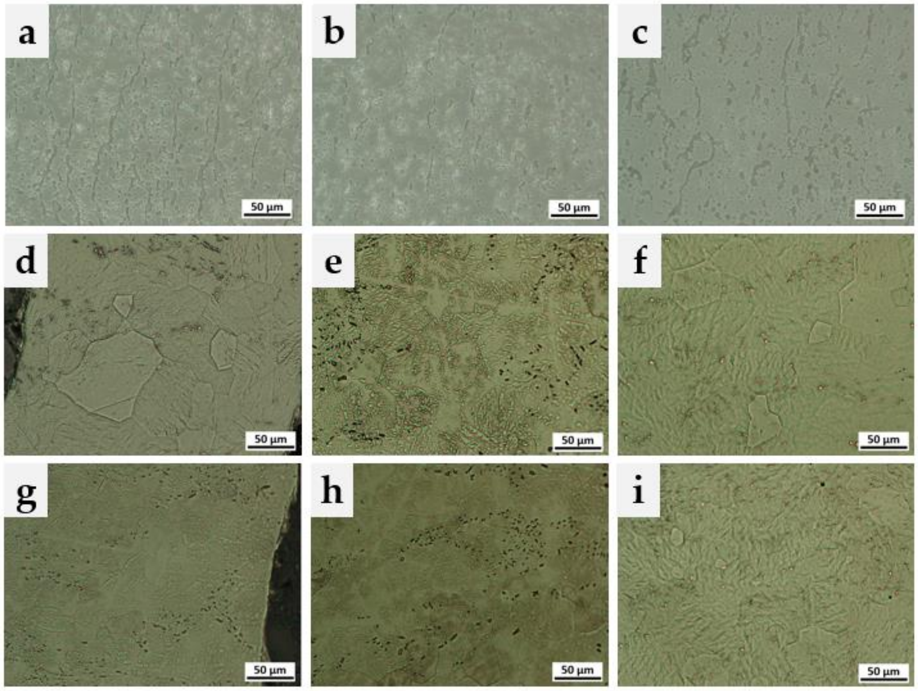

Figure 4. The OM micrographs of the Ti–Ni–Cu/TiNi bi-metallic structure at three locations under three heat treatment conditions. (a) AD Ti–Ni–Cu alloy. (b) HT400 Ti–Ni–Cu alloy. (c) HT600 Ti–Ni–Cu alloy. (d) AD TiNi substrate near-top region. (e) HT400 TiNi substrate near-top region. (f) HT600 TiNi substrate near-top region. (g) AD TiNi substrate near-bottom region. (h) HT400 TiNi substrate near-bottom region. (i) HT600 TiNi substrate near-bottom region. Notice that in images from (d) to (i), minor phase structures within grains are different based on two substrate locations and three heat treatment conditions.

Figure 5 includes SEM images obtained from the TiNi substrate near-top region and the near-bottom region under the AD and HT400 conditions. Figure 5a and Figure 5b were taken from the near-top region in the AD state and the HT400 state, while Figure 5c and Figure 5d were acquired from the near-bottom region in the AD state and the HT400 state, respectively. Grains and grain boundaries are included in all four images in Figure 5. Whereas within grains, minor phase structures can be found to differ from each other. Minor microstructural features with dashed circles in Figure 5 show that Figure 5a has a homogeneous appearance within the grains, while in Figure 5b, there are long martensite-like structures, which did not show up in the AD state of the substrate at the near-top region. Figure 5c and Figure 5d show nanoscale features that might be precipitate-related structures within grains [31]. It was reported in near equiatomic TiNi alloys with a slightly Ni-rich composition, precipitates such as Ni_4Ti_3 can form under low-temperature aging treatment [31–33].

Notice that during the DED process, the laser power not only assisted in building up the DED Ti–Ni–Cu alloy section layer by layer but also resulted in the heating of the TiNi substrate. The substrate near-top region received more heating effects and got a higher temperature from the laser than the near-bottom region. For the AD state, the substrate near-bottom region (Figure 5c) includes a certain amount of precipitate-related structures, which is not found in Figure 5a from the near-top region. It was stated that high-temperature heat treatment might result in the dissolution of precipitates [32,34]. Compared with the AD state near-bottom region, the homogenous structure at the AD state substrate near-top region is likely due to the higher temperature induced by the laser.

Figure 5b and Figure 5d demonstrate HT400 state images after the AD states in Figure 5a and Figure 5c, respectively. After 400 °C heat treatment of a laser-heated area, the substrate near-top region formed larger martensite-like structures, as seen in Figure 5b. While there was not an obvious difference in the microstructural feature at the substrate near-bottom region after the 400 °C heat treatment. In contrast, after 600 °C heat treatment, both the HT600 substrate near-top and near-bottom regions show very similar microstructure seen in Figure 4f and Figure 4i without nanoscale features in HT400 substrate samples. The high-temperature heat treatment at 600 °C resulted a more homogeneous TiNi matrix with a much weaker location-dependency within the substrate.

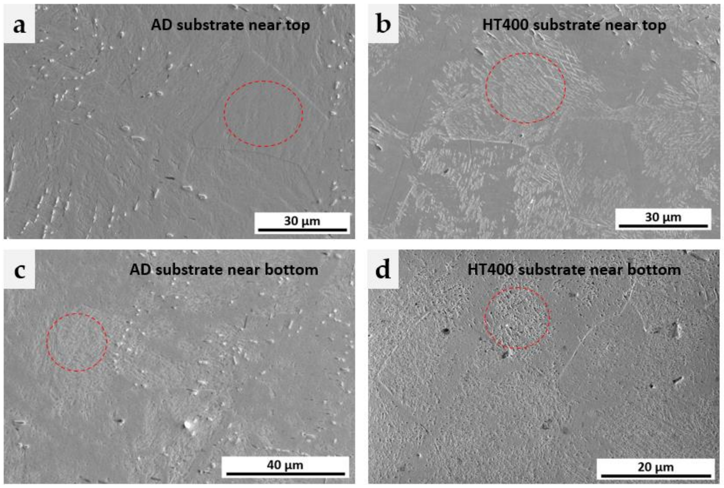

Figure 5. SEM images of (a) AD TiNi substrate near-top region. (b) HT400 TiNi substrate near-top region. (c) AD TiNi substrate near-bottom region. (d) HT400 TiNi substrate near-bottom region. Notice the microstructure features in dashed circles show differences among four images.

3.2. PHASE TRANSFORMATION

Figure 6 is the DSC curve of the as-received TiNi substrate material. It can be observed that the peak related to the intermediate R–phase before the occurrence of martensite formation peak exists during cooling [35]. Transformation temperatures can be measured from the DSC curve, and particularly, the austenite finishing temperature (A_f) of this as-received near equiatomic TiNi substrate material is 41.3 °C.

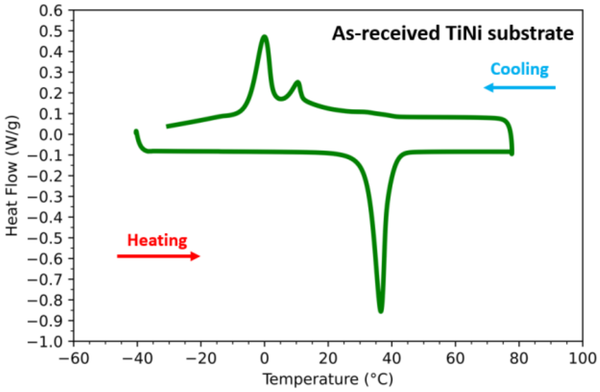

Figure 6. DSC curve of the as-received TiNi substrate.

The DSC curves of the additively manufactured bi-metallic structure under the AD, HT400, and HT600 status are demonstrated in Figure 7, Figure 8, and Figure 9, respectively, and all three locations are included.

For the phase transformation temperatures of the AD state in Figure 7, the DED Ti–Ni–Cu region with the highly Ti-rich matrix has the highest characteristic temperatures where the A_f is measured as 92.8 °C, as seen in Figure 7a. The TiNi substrate upper region (Figure 7b) shows a single martensite transformation during cooling and low transformation temperatures. The A_f of the substrate upper region is 20.4 °C, which indicates that at room temperature, the TiNi phase is mostly in an austenite state. In contrast, the DSC curve of the substrate lower region shown in Figure 7c includes the R phase peak that has some overlap with the martensite peak. Also, the A_f value of the AD substrate lower region is 42.6 °C, which is very close to the as-received substrate in Figure 6. It was reported that the R phase could nucleate around precipitate sites [36]. The AD state substrate upper region experienced high temperature from laser heating during the DED process, which resulted in the absence of the R phase and a one-step martensite transformation. In comparison, the AD state substrate lower region after the DED process did not received obvious laser heating effect, which resulted in similar phase transformation temperatures as the as-received state.

Figure 8 exhibits the DSC curves of the bi-metallic structure of HT400 status. Figure 8a has no obvious changes in transformation features compared with the corresponding AD sample in Figure 7a. In contrast, both the locations within the substrate received higher A_f in the heating step that the martensite-to-austenite peaks shifted to the high-temperature direction. The A_f values of the substrate increased to around 57 °C. While in the cooling step, the temperatures corresponding to the R phase transformation and the martensite phase transformation from the TiNi substrate upper region and the TiNi substrate lower region show differences. The differences in transformation temperatures of the R phase and the martensite phase might be a result of the difference in the matrix of AD state between the substrate upper region and lower region that led to different precipitate features [31] after the 400 °C heat treatment.

Figure 9 summarizes the bi-metallic structure sample under HT600 for the same three locations. After the heat treatment at 600 °C, both the TiNi substrate upper region and lower region exhibit a one-step austenite-to-martensite phase transformation in the cooling step and a low A_f of about 24 °C. The DSC curves of the HT600 substrate are completely different from that in HT400 (Figures 8b–c), while they show similarity with the AD substrate upper region. The laser heating and 600 °C heat treatment similarly affected the phase transformation of the TiNi substrate. The absence of the R phase after 600 °C heat treatment has also been reported in the literature [30,34]. The martensite transformation temperatures are also similar in both substrate upper and lower regions, which are not obviously affected by precipitates. The type of the DSC curve of the section from the DED Ti–Ni–Cu alloy is still similar to the AD and HT400 cases with high transformation temperatures. This indicates that the Ti-rich Ti–Ni–Cu SMA fabricated by the elemental powder DED process can possess a stable shape memory effect after 600 °C heat treatment.

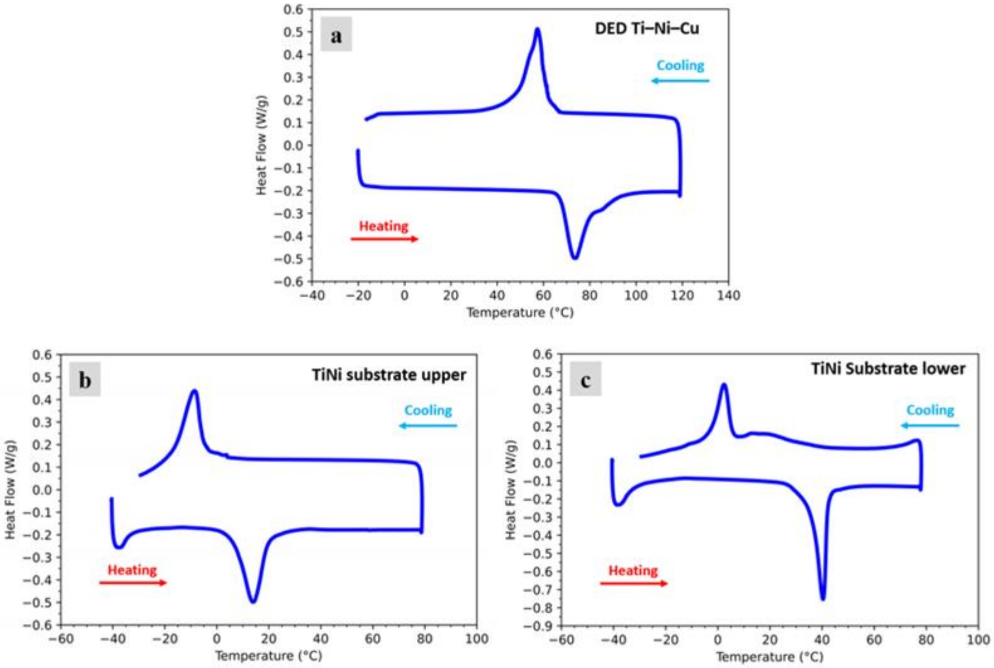

Figure 7. DSC curves at three locations under the AD state. (a) DED Ti–Ni–Cu alloy region. (b) TiNi substrate upper region. (c) TiNi substrate lower region.

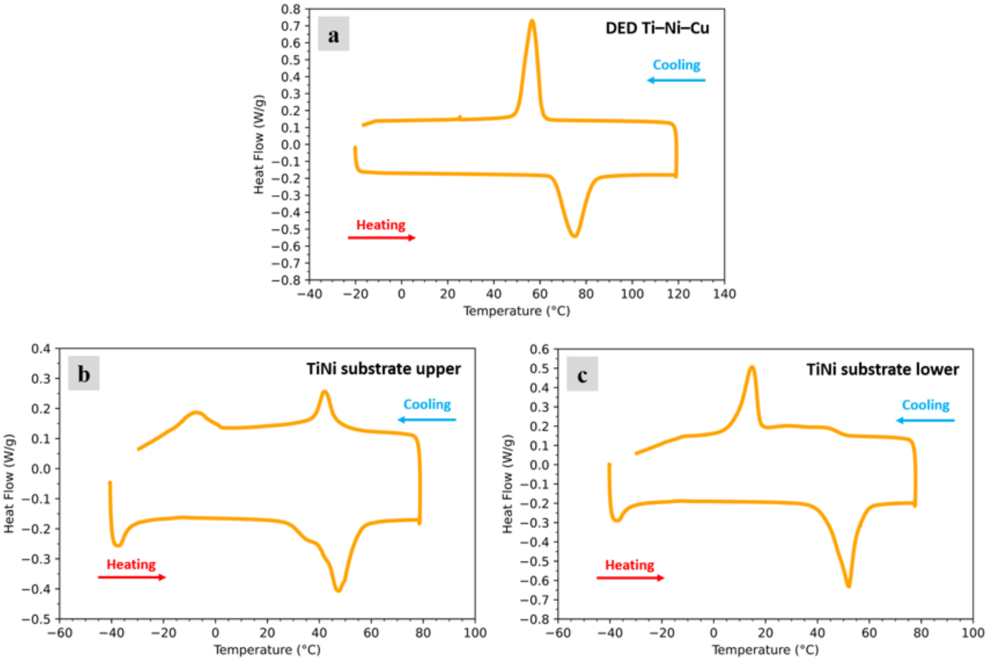

Figure 8. DSC curves at three locations under the HT400 state. (a) DED Ti–Ni–Cu alloy region. (b) TiNi substrate upper region. (c) TiNi substrate lower region.

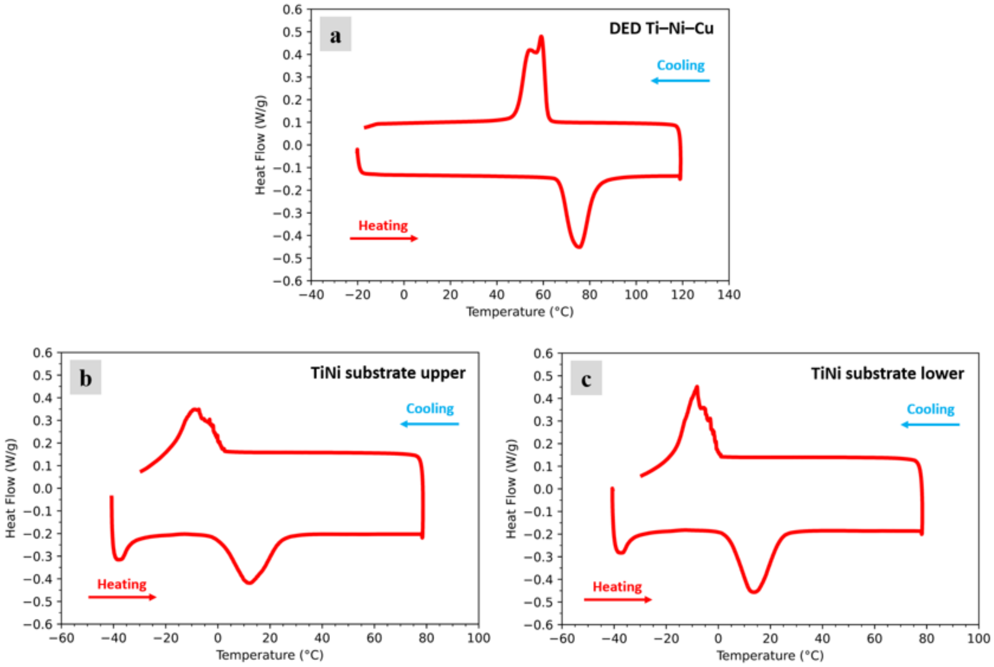

Figure 9. DSC curves at three locations under the HT600 state. (a) DED Ti–Ni–Cu alloy region. (b) TiNi substrate upper region. (c) TiNi substrate lower region.

All the A_f values from the three sections under three heat treatment states, together with the as-received TiNi substrate, are listed in Figure 10. By using the high material and spatial flexibility in the DED process to combine different SMAs together to form bi-metallic structures with different responses to heat treatment, various transformation temperature combinations can be realized in a cost-effective approach.

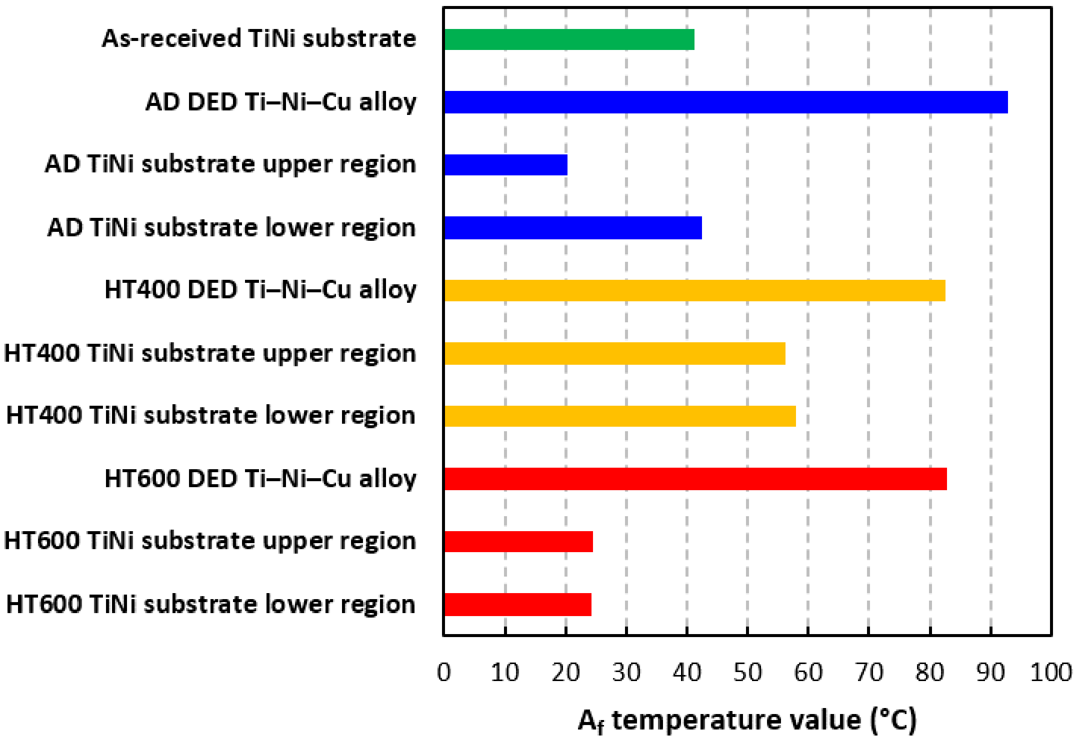

Figure 10. Summary of A_f values in various locations at three heat treatment conditions.

3.3. MECHANICAL PROPERTIES

Stress-strain curves of miniature tensile samples at three locations are listed in Figures 11a–f. The curve of the as-received substrate in Figure 11a indicates a martensite feature with a low-stress plateau caused by martensite reorientation, as mentioned in [37]. As the A_f of the as-received substrate is 41.3 °C, martensite-type behavior is expected at room temperature. Figure 11b demonstrates the stress-strain curve of the AD Ti–Ni–Cu alloy. The Ti–Ni–Cu alloy shows behavior more like martensite TiNi with a lower tensile strain when the tensile stress reaches 300 MPa. This could be due to the existence of the Ti_2Ni intermetallic phases that limited its tensile elongation.

The substrate lower region in the AD status has a stress-strain curve (Figure 11e) very close to the as-received TiNi (Figure 11a), which agrees well with the high similarity in phase transformation information between the AD substrate lower region and the as-received substrate. On the other hand, the AD substrate upper region underwent high-temperature heat treatment and exhibited more austenite phase at room temperature according to the DSC curve. The stress-strain curve of the AD substrate upper region in Figure 11c has a higher stress plateau occurring between 200 MPa and 250 MPa, which is more likely due to the stress-induced martensite formation [38].

When the austenite-dominated AD substrate upper region went through heat treatment at 400 °C, the mechanical response became martensite type again in Figure 11d as the microstructure shows more martensite features. On the other hand, after the heat treatment at 600 °C, the TiNi of the AD substrate lower region turned into austenite behavior with a higher stress plateau that represents the stress-induced martensite formation shown in Figure 11f, which matches the low A_f close to the room temperature shown in Figure 9c.

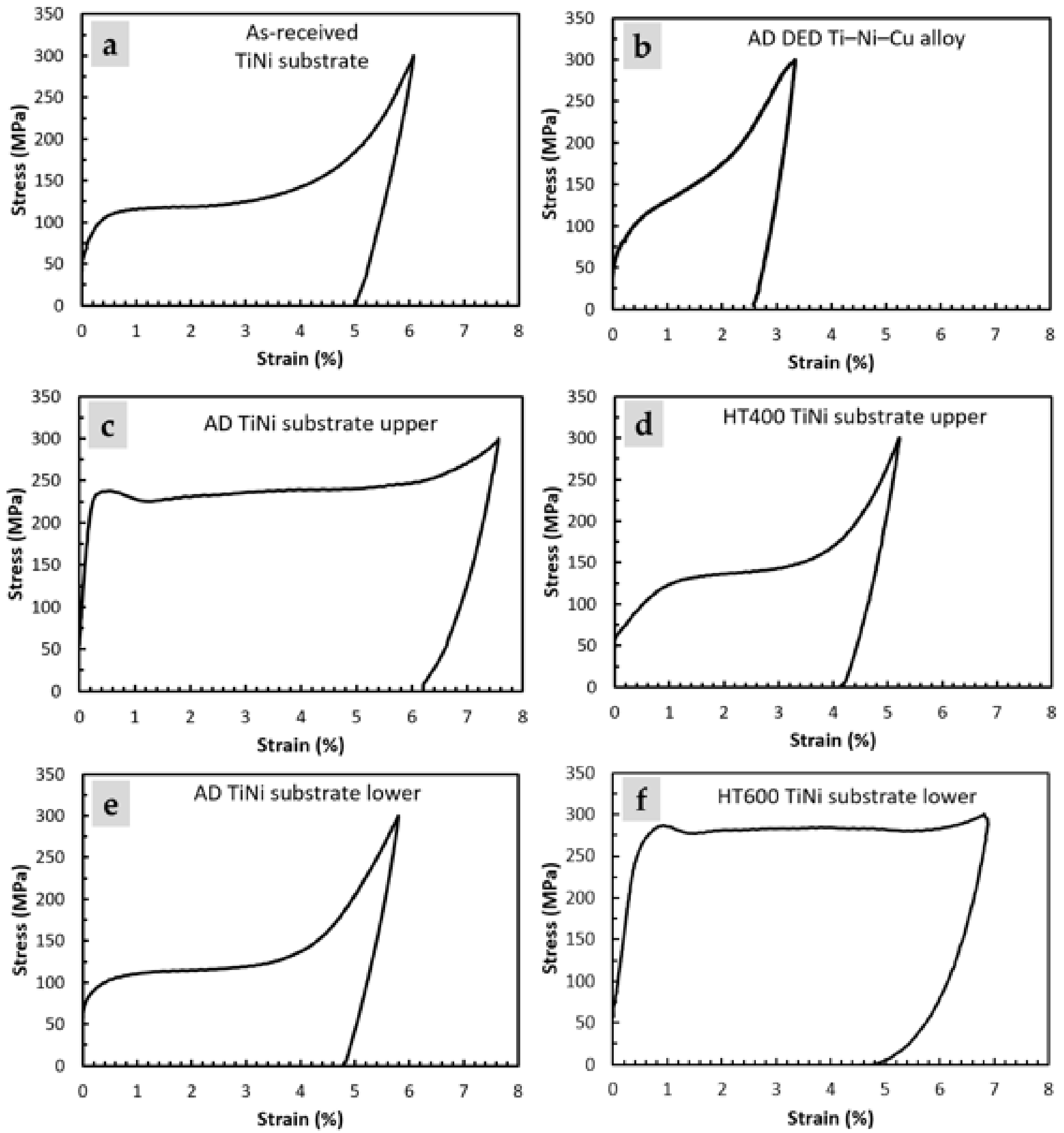

Figure 11. Tensile stress-strain curves from various locations under various post treatments. (a) As-received TiNi alloy substrate. (b) The AD DED Ti–Ni–Cu alloy. (c) The AD TiNi substrate upper region. (d) The HT400 TiNi substrate upper region. (e) The AD TiNi substrate lower region. (f) The HT600 TiNi substrate lower region.

4. CONCLUSIONS

This work studied the post heat treatment effect on the additively manufactured bi-metallic Ti–Ni–Cu/TiNi SMA fabricated by elemental powder DED process in different locations. Particularly, three locations at the DED Ti–Ni–Cu region, the TiNi substrate upper region, and the TiNi substrate lower region under three heat treatment conditions: AD, HT400, and HT600 states were evaluated in terms of microstructure, mechanical, and functional properties.

The DED Ti-rich Ti–Ni–Cu region consists of the Ti-rich TiNi matrix and Ti_2Ni secondary phases. The microstructure and phase transformation did not have obvious changes under heat treatments. Under all heat treatment conditions, the Ti-rich Ti–Ni–Cu region has austenite finishing temperatures higher than 80 °C.

For the near equiatomic substrate, the laser heating resulted in a temperature gradient that created the difference in microstructure and material behaviors between the substrate upper region and the substrate lower region. At the AD state, the substrate upper region received more laser heating effect and exhibited homogeneous austenite-dominated grains and a low A_f value of 20.4 °C. On the other side, the substrate lower region exhibits precipitate-like minor structures and maintained an A_f of about 42.6 °C with some martensite behavior at room temperature.

HT400 condition increased the A_f values of both two substrate locations to approximately 57 °C with martensite behaviors. Differences in cooling of DSC curves at the two locations were observed that might be due to the different precipitate features. HT600 condition resulted in the substrate A_f at about 24 °C with austenite-dominate behaviors. All three locations show a good correlation among microstructure, phase, and tensile properties. More heat treatment conditions can be further explored to create a wider range of combinations of transformation temperatures for multifunctional applications of novel SMAs after the DED AM process.

ACKNOWLEDGMENTS

This research was partially funded by the U.S. Department of Energy STTR Contract DE-SC0018879, the National Science Foundation Grants CMMI 1625736, and the Material Research Center at Missouri S&T. Their financial support is greatly appreciated. The authors thank the Intelligent Systems Center, the Material Research Center, and the Department of Chemistry Shared Instruments Lab at Missouri S&T for all the support in research.

REFERENCES

1. Chen, Lian, Yong He, Yingxin Yang, Shiwei Niu, and Haitao Ren. "The research status and development trend of additive manufacturing technology." The International Journal of Advanced Manufacturing Technology 89, no. 9 (2017): 3651-3660.
2. Du Plessis, Anton, Ina Yadroitsava, and Igor Yadroitsev. "Effects of defects on mechanical properties in metal additive manufacturing: A review focusing on X-ray tomography insights." Materials & Design 187 (2020): 108385.
3. Dilberoglu, Ugur M., Bahar Gharehpapagh, Ulas Yaman, and Melik Dolen. "The role of additive manufacturing in the era of industry 4.0." Procedia Manufacturing 11 (2017): 545-554.
4. Bandyopadhyay, Amit, Yanning Zhang, and Susmita Bose. "Recent developments in metal additive manufacturing." Current opinion in chemical engineering 28 (2020): 96-104.
5. Slotwinski, John A., and Edward J. Garboczi. "Metrology needs for metal additive manufacturing powders." Jom 67, no. 3 (2015): 538-543.

6. Kang, Nan, Mohamed El Mansori, X. Lin, Fabrice Guittonneau, H. L. Liao, W. D. Huang, and C. Coddet. "In-situ synthesis of aluminum/nano-quasicrystalline Al-Fe-Cr composite by using selective laser melting." Composites Part B: Engineering 155 (2018): 382-390.

7. Svetlizky, David, Baolong Zheng, Alexandra Vyatskikh, Mitun Das, Susmita Bose, Amit Bandyopadhyay, Julie M. Schoenung, Enrique J. Lavernia, and Noam Eliaz. "Laser-based directed energy deposition (DED-LB) of advanced materials." Materials Science and Engineering: A (2022): 142967.

8. Saboori, Abdollah, Donato Gallo, Sara Biamino, Paolo Fino, and Mariangela Lombardi. "An overview of additive manufacturing of titanium components by directed energy deposition: microstructure and mechanical properties." Applied Sciences 7, no. 9 (2017): 883.

9. Caiazzo, Fabrizia, and Vittorio Alfieri. "Directed Energy Deposition of stainless steel wire with laser beam: evaluation of geometry and affection depth." Procedia CIRP 99 (2021): 348-351.

10. Gibson, Brian T., Yashwanth Kumar Bandari, Bradley S. Richardson, William C. Henry, Emma J. Vetland, Tayler W. Sundermann, and Lonnie J. Love. "Melt pool size control through multiple closed-loop modalities in laser-wire directed energy deposition of Ti-6Al-4V." Additive Manufacturing 32 (2020): 100993.

11. Feenstra, D. R., V. Cruz, X. Gao, A. Molotnikov, and N. Birbilis. "Effect of build height on the properties of large format stainless steel 316L fabricated via directed energy deposition." Additive Manufacturing 34 (2020): 101205.

12. Caiazzo, Fabrizia, Vittorio Alfieri, and Giovanni Bolelli. "Residual stress in laser-based directed energy deposition of aluminum alloy 2024: Simulation and validation." The International Journal of Advanced Manufacturing Technology 118, no. 3 (2022): 1197-1211.

13. Jinoop, A. N., C. P. Paul, and K. S. Bindra. "Laser-assisted directed energy deposition of nickel super alloys: a review." Proceedings of the Institution of Mechanical Engineers, Part L: Journal of Materials: Design and Applications 233, no. 11 (2019): 2376-2400.

14. Liu, Zhiying, Bei He, Tianyi Lyu, and Yu Zou. "A Review on Additive manufacturing of titanium alloys for aerospace applications: directed energy deposition and beyond Ti-6Al-4V." Jom 73, no. 6 (2021): 1804-1818.

15. Radhakrishnan, M., M. M. Hassan, B. E. Long, D. Otazu, T. J. Lienert, and O. Anderoglu. "Microstructures and properties of Ti/TiC composites fabricated by laser-directed energy deposition." Additive Manufacturing 46 (2021): 102198.

16. Zhang, Xinchang, Lan Li, Tan Pan, Yitao Chen, Yunlu Zhang, Wei Li, and Frank Liou. "Additive manufacturing of copper-tool steel dissimilar joining: Experimental characterization and thermal modeling." Materials Characterization 170 (2020): 110692.

17. Bobbio, Lourdes D., Richard A. Otis, John Paul Borgonia, R. Peter Dillon, Andrew A. Shapiro, Zi-Kui Liu, and Allison M. Beese. "Additive manufacturing of a functionally graded material from Ti-6Al-4V to Invar: Experimental characterization and thermodynamic calculations." Acta Materialia 127 (2017): 133-142.

18. Khodabakhshi, F., M. H. Farshidianfar, S. Bakhshivash, A. P. Gerlich, and A. Khajepour. "Dissimilar metals deposition by directed energy based on powder-fed laser additive manufacturing." Journal of Manufacturing Processes 43 (2019): 83-97.

19. Bae, Joohyeon, Hyunsuk Lee, Duckhyeon Seo, Sangdu Yun, Jeonghyeon Yang, Sunchul Huh, Hyomin Jeong, and Jungpil Noh. "Grain Size and Phase Transformation Behavior of TiNi Shape-Memory-Alloy Thin Film under Different Deposition Conditions." Materials 13, no. 14 (2020): 3229.

20. Yang, Chi, Sylvester Abanteriba, and Andrew Becker. "A review of shape memory alloy based filtration devices." AIP Advances 10, no. 6 (2020): 060701.

21. Walker, Jason, Mohsen Taheri Andani, Christoph Haberland, and Mohammad Elahinia. "Additive manufacturing of Nitinol shape memory alloys to overcome challenges in conventional Nitinol fabrication." In ASME International Mechanical Engineering Congress and Exposition, vol. 46438, p. V02AT02A037. American Society of Mechanical Engineers, 2014.

22. Hamilton, Reginald F., Todd A. Palmer, and Beth A. Bimber. "Spatial characterization of the thermal-induced phase transformation throughout as-deposited additive manufactured NiTi bulk builds." Scripta Materialia 101 (2015): 56-59.

23. Halani, Pratik R., and Yung C. Shin. "In situ synthesis and characterization of shape memory alloy nitinol by laser direct deposition." Metallurgical and Materials Transactions A 43, no. 2 (2012): 650-657.

24. De Araújo, C. J., N. J. Da Silva, M. M. Da Silva, and C. H. Gonzalez. "A comparative study of Ni–Ti and Ni–Ti–Cu shape memory alloy processed by plasma melting and injection molding." Materials & Design 32, no. 10 (2011): 4925-4930.

25. Chen, Yitao, Cesar Ortiz Rios, Braden McLain, Joseph W. Newkirk, and Frank Liou. "TiNi-Based Bi-Metallic Shape-Memory Alloy by Laser-Directed Energy Deposition." Materials 15, no. 11 (2022): 3945.

26. Deepan Bharathi Kannan, T., Raju Pegada, P. Sathiya, and T. Ramesh. "A comparison of the effect of different heat treatment processes on laser-welded NiTinol sheets." Journal of the Brazilian Society of Mechanical Sciences and Engineering 40, no. 12 (2018): 1-11.

27. Oliveira, Joao Pedro, FM Braz Fernandes, R. M. Miranda, N. Schell, and J. L. Ocaña. "Effect of laser welding parameters on the austenite and martensite phase fractions of NiTi." Materials Characterization 119 (2016): 148-151.

28. Marattukalam, Jithin J., Vamsi K. Balla, Mitun Das, Srikanth Bontha, and Sreeram K. Kalpathy. "Effect of heat treatment on microstructure, corrosion, and shape memory characteristics of laser deposited NiTi alloy." Journal of Alloys and Compounds 744 (2018): 337-346.

29. Karnati, Sreekar, I. Axelsen, F. F. Liou, and Joseph William Newkirk. "Investigation of tensile properties of bulk and SLM fabricated 304L stainless steel using various gage length specimens." In 2016 International Solid Freeform Fabrication Symposium. University of Texas at Austin, 2016.

30. Saedi, Soheil, Ali Sadi Turabi, Mohsen Taheri Andani, Narges Shayesteh Moghaddam, Mohammad Elahinia, and Haluk Ersin Karaca. "Texture, aging, and superelasticity of selective laser melting fabricated Ni-rich NiTi alloys." Materials Science and Engineering: A 686 (2017): 1-10.

31. Yu, Hao, Ying Qiu, and Marcus L. Young. "Influence of Ni4Ti3 precipitate on pseudoelasticity of austenitic NiTi shape memory alloys deformed at high strain rate." Materials Science and Engineering: A 804 (2021): 140753.

32. Ben Fraj, B., A. Gahbiche, S. Zghal, and Z. Tourki. "On the influence of the heat treatment temperature on the superelastic compressive behavior of the Ni-Rich NiTi shape memory alloy." Journal of Materials Engineering and Performance 26, no. 11 (2017): 5660-5668.

33. Otsuka, Kazuhiro, and Xiabing Ren. "Physical metallurgy of Ti–Ni-based shape memory alloys." Progress in materials science 50, no. 5 (2005): 511-678.

34. Zheng, Yufeng, Fei Jiang, Li Li, Hong Yang, and Yinong Liu. "Effect of ageing treatment on the transformation behaviour of Ti–50.9 at.% Ni alloy." Acta Materialia 56, no. 4 (2008): 736-745.

35. Tan, L., and W. C. Crone. "In situ TEM observation of two-step martensitic transformation in aged NiTi shape memory alloy." Scripta materialia 50, no. 6 (2004): 819-823.

36. Huo, Xinyu, Peng Chen, Simanta Lahkar, Mingjiang Jin, Xiaocang Han, Yuanwei Song, and Xiaodong Wang. "Occurrence of the R-phase with increased stability induced by low temperature precipitate-free aging in a Ni50. 9Ti49. 1 alloy." Acta Materialia 227 (2022): 117688.

37. Lu, H. Z., C. Yang, X. Luo, H. W. Ma, B. Song, Y. Y. Li, and L. C. Zhang. "Ultrahigh-performance TiNi shape memory alloy by 4D printing." Materials Science and Engineering: A 763 (2019): 138166.

38. Xue, L., K. C. Atli, S. Picak, C. Zhang, B. Zhang, A. Elwany, R. Arroyave, and I. Karaman. "Controlling martensitic transformation characteristics in defect-free NiTi shape memory alloys fabricated using laser powder bed fusion and a process optimization framework." Acta Materialia 215 (2021): 117017.

SECTION

2. CONCLUSIONS

In this dissertation, the fabrication and development of various types of metal alloys using the directed energy deposition (DED) processing technique with elemental powder mixture as the novel type of feedstock was reviewed, which comprehensively summarized the current status, scientific guidelines, and outlook to the future development of the advanced alloys by the DED additive manufacturing (AM) process with a wide range of material flexibility from elemental powder mixture.

The novel elemental powder method in the DED process was proven to be effective in synthesizing Ti–Ni–Cu ternary shape memory alloy (SMA) using Ti, Ni, and Cu elemental powders as feedstock. By using the idea of the elemental powder mixture, a third metal element can be flexibly selected and added to the TiNi-based system to create more types of TiNi-based alloys and novel material properties in the SMA field. The as-fabricated Ti–Ni–Cu alloy demonstrated the desired TiNi major phase. Phase transformation temperatures were detected, and a narrower thermal hysteresis range of 11~16 °C was obtained, which indicated the effective addition of Cu in Ti–Ni–Cu alloys fabricated by the AM process. The results and findings provided important and useful data points for the area of 4D printing of smart metallic materials.

Next, a Ti–Ni–Cu ternary SMA with a Ti-rich composition was deposited on a TiNi binary SMA substrate with a near equiatomic composition using the elemental powder DED process. The advantage of DED in selecting a wider range of substrate material and feedstock materials was fully utilized to realize Ti–Ni–Cu/TiNi bi-metallic SMA structures by combining multiple types of TiNi-based SMAs in a single part to show multifunctional shape memory behavior. Bi-metallic SMA structures with multiple element types, compositions, and processing methods were built by DED with a high joining quality at the interface where no pore or crack was detected, which indicated the good interaction between the substrate and the first few layers of the DED section. The major phase from all the height locations was identified as the TiNi phase without very high hardness values. The tensile test with digital image correlation (DIC) showed a bonding strength of 569.1 MPa. An obvious difference in mechanical responses of two SMA sections on two sides of the interface was also observed from DIC. The multiple shape memory effects from the TiNi substrate side (A_f < 50 °C) and the DED Ti–Ni–Cu alloy side (A_f > 80 °C) were successfully demonstrated, which shows the potential in manufacturing new smart materials, such as structures with multiple shape memory effects that can work differently in multiple temperature environments.

Also, follow-up studies were performed on heat treatment effects on the structure and properties of additively manufactured bi-metallic SMA structures with respect to various locations under different thermal histories from laser processing and multiple levels of post heat treatment temperatures at 400 °C and 600 °C. It was found that more combinations of transformation temperatures within a single bi-metallic SMA were achieved as the result of different locations that experienced various microstructural feature changes after heat treatment.

This work provides a systematic review of using elemental powder mixture as an alternative way to design and manufacture advanced alloys using the DED process for various industrial environments. The results and findings in the AM of TiNi-based ternary SMA and bi-metallic SMA structures with tailorable multi-sectional shape memory effects from elemental powder mixture not only improve the understanding and broaden the applications of the laser metal AM process and 4D printing but also offer new ideas to the development of innovative smart materials for multifunctionality.

BIBLIOGRAPHY

1. Mwangi, James Wamai, Linh T. Nguyen, Viet D. Bui, Thomas Berger, Henning Zeidler, and Andreas Schubert. "Nitinol manufacturing and micromachining: A review of processes and their suitability in processing medical-grade nitinol." Journal of manufacturing processes 38 (2019): 355-369.

2. Wen, Chunsheng, Xiaojiao Yu, Wei Zeng, Shan Zhao, Lin Wang, Guangchao Wan, Shicheng Huang, Hannah Grover, and Zi Chen. "Mechanical behaviors and biomedical applications of shape memory materials: A review." AIMS Materials Science 5, no. 4 (2018): 559-590.

3. Jani, Jaronie Mohd, Martin Leary, Aleksandar Subic, and Mark A. Gibson. "A review of shape memory alloy research, applications and opportunities." Materials & Design (1980-2015) 56 (2014): 1078-1113.

4. Lee, Eun Sang, and Tae Hee Shin. "An evaluation of the machinability of nitinol shape memory alloy by electrochemical polishing." Journal of mechanical science and technology 25, no. 4 (2011): 963-969.

5. Liu, J. F., L. Li, and Y. B. Guo. "Surface integrity evolution from main cut to finish trim cut in W-EDM of shape memory alloy." Procedia CIRP 13 (2014): 137-142.

6. Lee, Hyub, Chin Huat Joel Lim, Mun Ji Low, Nicholas Tham, Vadakke Matham Murukeshan, and Young-Jin Kim. "Lasers in additive manufacturing: A review." International Journal of Precision Engineering and Manufacturing-Green Technology 4, no. 3 (2017): 307-322.

7. Chew, Y., G. J. Bi, Z. G. Zhu, F. L. Ng, F. Weng, S. B. Liu, S. M. L. Nai, and B. Y. Lee. "Microstructure and enhanced strength of laser aided additive manufactured CoCrFeNiMn high entropy alloy." Materials Science and Engineering: A 744 (2019): 137-144.

8. Hwang, Taewoo, Young Yun Woo, Sang Wook Han, and Young Hoon Moon. "Functionally graded properties in directed-energy-deposition titanium parts." Optics & Laser Technology 105 (2018): 80-88.

9. Saboori, Abdollah, Alberta Aversa, Giulio Marchese, Sara Biamino, Mariangela Lombardi, and Paolo Fino. "Microstructure and mechanical properties of AISI 316L produced by directed energy deposition-based additive manufacturing: A review." Applied Sciences 10, no. 9 (2020): 3310.

10. Despeisse, Mélanie, and Simon Ford. "The role of additive manufacturing in improving resource efficiency and sustainability." In IFIP International Conference on Advances in Production Management Systems, pp. 129-136. Springer, Cham, 2015.

11. Svetlizky, David, Baolong Zheng, Tali Buta, Yizhang Zhou, Oz Golan, Uri Breiman, Rami Haj-Ali, Julie M. Schoenung, Enrique J. Lavernia, and Noam Eliaz. "Directed energy deposition of Al 5xxx alloy using Laser Engineered Net Shaping (LENS®)." Materials & Design 192 (2020): 108763.

12. Kistler, Nathan A., David J. Corbin, Abdalla R. Nassar, Edward W. Reutzel, and Allison M. Beese. "Effect of processing conditions on the microstructure, porosity, and mechanical properties of Ti-6Al-4V repair fabricated by directed energy deposition." Journal of Materials Processing Technology 264 (2019): 172-181.

13. Hu, Y. L., Y. L. Li, S. Y. Zhang, X. Lin, Z. H. Wang, and W. D. Huang. "Effect of solution temperature on static recrystallization and ductility of Inconel 625 superalloy fabricated by directed energy deposition." Materials Science and Engineering: A 772 (2020): 138711.

14. Yu, Lin, Keyu Chen, Yuanling Zhang, Jie Liu, Lei Yang, and Yusheng Shi. "Microstructures and mechanical properties of NiTi shape memory alloys fabricated by wire arc additive manufacturing." Journal of Alloys and Compounds 892 (2022): 162193.

15. Aydogan, Beytullah, Aaron O'Neil, and Himanshu Sahasrabudhe. "Microstructural and mechanical characterization of stainless steel 420 and Inconel 718 multi-material structures fabricated using laser directed energy deposition." Journal of Manufacturing Processes 68 (2021): 1224-1235.

16. Gibson, Ian, David Rosen, and Brent Stucker. "Directed energy deposition processes." In Additive manufacturing technologies, pp. 245-268. Springer, New York, NY, 2015.

17. Schwendner, Katrin I., Rajarshi Banerjee, Peter C. Collins, Craig A. Brice, and Hamish L. Fraser. "Direct laser deposition of alloys from elemental powder blends." Scripta Materialia 45, no. 10 (2001): 1123-1129.

18. Liu, Yong, L. F. Chen, H. P. Tang, Chain T. Liu, Bin Liu, and B. Y. Huang. "Design of powder metallurgy titanium alloys and composites." Materials Science and Engineering: A 418, no. 1-2 (2006): 25-35.

19. Karnati, Sreekar, Yunlu Zhang, Frank F. Liou, and Joseph W. Newkirk. "On the feasibility of tailoring copper–nickel functionally graded materials fabricated through laser metal deposition." Metals 9, no. 3 (2019): 287.

20. Halani, Pratik R., and Yung C. Shin. "In situ synthesis and characterization of shape memory alloy nitinol by laser direct deposition." Metallurgical and Materials Transactions A 43, no. 2 (2012): 650-657.

21. De Araújo, C. J., N. J. Da Silva, M. M. Da Silva, and C. H. Gonzalez. "A comparative study of Ni–Ti and Ni–Ti–Cu shape memory alloy processed by plasma melting and injection molding." Materials & Design 32, no. 10 (2011): 4925-4930.

22. Medeiros, Melânea Almeida Ramalho, and Carlos José de Araújo. "Thermal, microstructural and elastic modulus behavior of Ti50Ni50− xNbx (x= 0–25% at) shape memory alloys obtained by plasma arc melting." Journal of Alloys and Compounds 866 (2021): 158970.

23. Zhang, Xinchang, Cheng Sun, Tan Pan, Aaron Flood, Yunlu Zhang, Lan Li, and Frank Liou. "Additive manufacturing of copper–H13 tool steel bi-metallic structures via Ni-based multi-interlayer." Additive Manufacturing 36 (2020): 101474.

24. Zhang, Wenqi, Baopeng Zhang, Haifeng Xiao, Huanqing Yang, Yun Wang, and Haihong Zhu. "A Layer-Dependent Analytical Model for Printability Assessment of Additive Manufacturing Copper/Steel Multi-Material Components by Directed Energy Deposition." Micromachines 12, no. 11 (2021): 1394.

25. Onuike, Bonny, Bryan Heer, and Amit Bandyopadhyay. "Additive manufacturing of Inconel 718—Copper alloy bimetallic structure using laser engineered net shaping (LENS™)." Additive Manufacturing 21 (2018): 133-140.

26. Zhang, Yanning, and Amit Bandyopadhyay. "Direct fabrication of bimetallic Ti6Al4V+ Al12Si structures via additive manufacturing." Additive manufacturing 29 (2019): 100783.

27. Groden, C., Kellen D. Traxel, Ali Afrouzian, E. Nyberg, and A. Bandyopadhyay. "Inconel 718-W7Ni3Fe bimetallic structures using directed energy deposition-based additive manufacturing." Virtual and Physical Prototyping (2022): 1-11.

28. Khodabakhshi, F., M. H. Farshidianfar, S. Bakhshivash, A. P. Gerlich, and A. Khajepour. "Dissimilar metals deposition by directed energy based on powder-fed laser additive manufacturing." Journal of Manufacturing Processes 43 (2019): 83-97.

29. Nematollahi, Mohammadreza, Keyvan Safaei, Parisa Bayati, and Mohammad Elahinia. "Functionally graded NiTi shape memory alloy: Selective laser melting fabrication and multi-scale characterization." Materials Letters 292 (2021): 129648.

30. Collins, P. C., R. Banerjee, S. Banerjee, and H. L. Fraser. "Laser deposition of compositionally graded titanium–vanadium and titanium–molybdenum alloys." Materials Science and Engineering: A 352, no. 1-2 (2003): 118-128.

31. Borkar, Tushar, Bharat Gwalani, Deep Choudhuri, C. V. Mikler, C. J. Yannetta, Xiaodong Chen, Raju Vijayaraghavan Ramanujan, M. J. Styles, M. A. Gibson, and Rajarshi Banerjee. "A combinatorial assessment of AlxCrCuFeNi2 (0< x< 1.5) complex concentrated alloys: Microstructure, microhardness, and magnetic properties." Acta Materialia 116 (2016): 63-76.

32. Alijani, Fatemeh, Rasool Amini, Mohammad Ghaffari, Morteza Alizadeh, and Ali Kemal Okyay. "Effect of milling time on the structure, micro-hardness, and thermal behavior of amorphous/nanocrystalline TiNiCu shape memory alloys developed by mechanical alloying." Materials & Design 55 (2014): 373-380.

33. Marattukalam, Jithin J., Vamsi K. Balla, Mitun Das, Srikanth Bontha, and Sreeram K. Kalpathy. "Effect of heat treatment on microstructure, corrosion, and shape memory characteristics of laser deposited NiTi alloy." Journal of Alloys and Compounds 744 (2018): 337-346.

34. Mehrpouya, Mehrshad, Annamaria Gisario, and Mohammad Elahinia. "Laser welding of NiTi shape memory alloy: A review." Journal of Manufacturing Processes 31 (2018): 162-186.

VITA

Yitao Chen was born in China. He received a B.E. degree in Materials Science and Engineering at Chongqing University (Chongqing, China) in 2013. He then received an M.S. degree in Materials Science and Engineering at Columbia University in 2015 and an M.S.E. degree in Mechanical Engineering at Johns Hopkins University in 2017. With a strong interest in additive manufacturing, he started his Ph.D. study in Mechanical Engineering at Missouri University of Science and Technology in August 2017 and worked in Dr. Frank Liou's lab on the study of additive manufacturing of shape memory alloys. During his Ph.D. study, he authored and co-authored eleven journal papers and seven conference papers, and was awarded the Department of Mechanical and Aerospace Engineering Mathews Fellowship. He received his Ph.D. degree in Mechanical Engineering in July 2022.